
Impact of Epitaxial Strain on Antiferroelectricity in NaNbO_3 and AgNbO_3 Thin Films

Zur Erlangung des Grades eines Doktors der Naturwissenschaften (Dr. rer. nat.)
Genehmigte Dissertation von Thorsten Schneider
Tag der Einreichung: 23. Januar 2024, Tag der Prüfung: 17. April 2024

1. Gutachten: Prof. Lambert Alff
2. Gutachten: Prof. Leopoldo Molina-Luna
Darmstadt, Technische Universität Darmstadt



TECHNISCHE
UNIVERSITÄT
DARMSTADT

Materials and Earth
Sciences Department
Materials Science
Advanced Thin Film
Technology



Impact of Epitaxial Strain on Antiferroelectricity in NaNbO_3 and AgNbO_3 Thin Films

Accepted doctoral thesis by Thorsten Schneider

Date of submission: 23. Januar 2024

Date of thesis defense: 17. April 2024

Darmstadt, Technische Universität Darmstadt

Bitte zitieren Sie dieses Dokument als:

URL: <http://tuprints.ulb.tu-darmstadt.de/27667>

Jahr der Veröffentlichung auf TUprints: 2024

Dieses Dokument wird bereitgestellt von tuprints,

E-Publishing-Service der TU Darmstadt

<http://tuprints.ulb.tu-darmstadt.de>

tuprints@ulb.tu-darmstadt.de

Die Veröffentlichung steht unter folgender Creative Commons Lizenz:

Namensnennung 4.0 International

<https://creativecommons.org/licenses/by/4.0/>

This work is licensed under a Creative Commons License:

Attribution 4.0 International

<https://creativecommons.org/licenses/by/4.0/>

Erklärungen laut Promotionsordnung

§ 8 Abs. 1 lit. c PromO

Ich versichere hiermit, dass die elektronische Version meiner Dissertation mit der schriftlichen Version übereinstimmt.

§ 8 Abs. 1 lit. d PromO

Ich versichere hiermit, dass zu einem vorherigen Zeitpunkt noch keine Promotion versucht wurde. In diesem Fall sind nähere Angaben über Zeitpunkt, Hochschule, Dissertationsthema und Ergebnis dieses Versuchs mitzuteilen.

§ 9 Abs. 1 PromO

Ich versichere hiermit, dass die vorliegende Dissertation selbstständig und nur unter Verwendung der angegebenen Quellen verfasst wurde.

§ 9 Abs. 2 PromO

Die Arbeit hat bisher noch nicht zu Prüfungszwecken gedient.

Darmstadt, 23. Januar 2024

T. Schneider

Zusammenfassung

Antiferroelektrische Materialien bieten eine verlockende Aussicht auf die Verbesserung moderner Kondensatoren durch die Einführung neuer Funktionalitäten und Erhöhung der Energiedichte. Obwohl bereits erste Schritte in Richtung Kommerzialisierung unternommen wurden, wird der Fortschritt durch ein begrenztes Verständnis des antiferroelektrischen Effekts und einen Mangel an Materialien, die diese einzigartige Eigenschaft aufweisen, behindert. In dieser Studie werden antiferroelektrische Perowskite als epitaktische Dünnschichten synthetisiert, um den Einfluss von Verspannungen auf das Gleichgewicht der antiferroelektrischen und ferroelektrischen Phasen zu untersuchen.

Dünne Schichten aus zwei antiferroelektrischen Materialien, NaNbO_3 und AgNbO_3 , werden durch gepulste Laserabscheidung hergestellt. Ähnlich zur Festkörpersynthese treten Probleme bei der Stöchiometrie des Kationenverhältnisses während des Wachstums der Dünnschicht auf. Diese Herausforderung kann überwunden werden, indem die Wachstumsparameter für NaNbO_3 angepasst werden, während Silbermangel in AgNbO_3 Schichten durch die Bereitstellung einer Silberreserve ausgeglichen wird. Diese liefert Silberionen um den nicht stöchiometrischen Transfer während des gepulsten Laserablationsprozesses zu korrigieren.

Das erfolgreiche Wachstum hochwertiger dünner Schichten wird anschließend auf verschiedene Substrate ausgedehnt, wobei sowohl Druck- als auch Zugspannungen in die dünnen Schichten eingebracht werden. So kann die Ausbildung des Grundzustands für beide Materialien untersucht werden und der Stabilitätsbereich der antiferroelektrischen Phase in Abhängigkeit der eingebrachten Verspannung bestimmt werden. Für beide Materialien wird das Vorhandensein eines antipolaren Grundzustands, der der antiferroelektrischen Struktur der Materialien als Keramik ähnelt, in Schichten beobachtet, die unter Druckbelastung gewachsen werden. Schichten unter Zugbelastung weisen im Gegensatz dazu nicht die erwartete strukturelle Symmetrie auf, die für antiferroelektrische Materialien charakteristisch ist.

Um die Stabilität dieser antiferroelektrischen Phase zu bewerten wird eine elektrische Charakterisierung in einer Kondensatorstruktur durchgeführt. Interessanterweise ähnelt das dielektrische Verhalten der NaNbO_3 Dünnschichten jedoch eher einem ferroelektrischen als einem antiferroelektrischen Material, obwohl der antipolare Grundzustand in

den unter Druckbelastung gewachsenen Dünnschichten beibehalten wird. Dies zeigt, dass keine zusätzliche Stabilisierung des antiferroelektrischen Zustands aufgrund der induzierten Verspannung zu beobachten ist. Nichtsdestotrotz steigt die Sättigungspolarisation der dünnen Schichten durch die Druckbelastung auf mehr als 200 %, was eine erhebliche Steigerung der Energiedichte für antiferroelektrische Kondensatoren verspricht. Zusammenfassend lässt sich sagen, dass diese Forschungsarbeit das Potenzial von Verspannung zur Verbesserung antiferroelektrischer Kondensatoren aufzeigt. Dünnschichten, die unter Druckbelastung gewachsen werden, behalten den antipolaren Grundzustand des Materials bei, wobei die Sättigungspolarisation der ferroelektrischen Phase erheblich verbessert wird. Durch die Kombination dieser Forschung mit dem eingehend untersuchten Dotierungsansatz zur weiteren Stabilisierung der antiferroelektrischen Phase wird eine wesentliche Verbesserung der Energiedichte antiferroelektrischer Kondensatoren erwartet.

Abstract

Antiferroelectric materials offer a tantalising prospect for enhancing modern capacitors by introducing novel functionalities and significantly increasing the energy density. Although initial steps have been taken towards commercialisation, progress is impeded by a limited understanding of the antiferroelectric effect and a scarcity of materials that exhibit this unique property. In this study, antiferroelectric perovskites are synthesised as epitaxial thin films to explore the nature of the antiferroelectric effect when impacted by strain, as well as the influence of epitaxy on the balance of the antiferroelectric and ferroelectric phases.

Thin films of antiferroelectric materials, specifically NaNbO_3 and AgNbO_3 , are fabricated through pulsed laser deposition. Challenges similar to those encountered in bulk synthesis are identified, concerning the preservation of stoichiometric cation ratios during thin film growth. These are overcome by adaptation of growth parameters for NaNbO_3 , while silver deficiency in AgNbO_3 films is addressed by provision of a silver reservoir. This reservoir supplies silver ions to rectify the off-stoichiometric transfer during the pulsed laser deposition process.

The successful growth of high-quality thin films is subsequently extended to various substrates, introducing a range of strains, from compressive to tensile, into the films. This allows to explore the formation of the ground state for both materials, and to determine the stability region of the antiferroelectric phase as a function of the induced strain. For both materials, the presence of a bulk-like antiferroelectric ground state is observed in films grown under compressive strain, whereas films under tensile strain do not exhibit the expected structural symmetry characteristic of antiferroelectric materials.

To evaluate the stability of this phase, electrical characterisation in a capacitor structure is performed. Interestingly, while an antipolar ground state is maintained in thin films grown under compressive strain, the dielectric behaviour of these NaNbO_3 thin films resembles that of a ferroelectric material rather than an antiferroelectric one. This shows that no additional stabilisation of the antiferroelectric phase is observed due to the induced strain. Nonetheless, the saturation polarisation of thin films grown under compressive strain increases to over 200 %, offering the promise of a significant boost in energy density for antiferroelectric capacitors.

In summary, this research demonstrates the potential of strain to enhance antiferroelectric capacitors. Thin films grown under compressive strain maintain the antiferroelectric characteristics of the bulk material, with a substantial enhancement in saturation polarisation of the ferroelectric phase. By combining this research with the thoroughly investigated doping approach to further stabilise the antiferroelectric phase, a substantial improvement in the energy density of antiferroelectric capacitors is anticipated.

Contents

List of Tables	xiii
List of Figures	xv
Acronyms	xix
1 Introduction and Motivation	1
1.1 Purpose and Structure of this Thesis	3
2 Physical Background	5
2.1 Dielectric Materials	5
2.1.1 Properties of Dielectrics	7
2.1.2 Ferroelectricity	8
2.1.3 Antiferroelectricity	10
2.2 The Perovskite Structure	12
2.2.1 Antiferroelectric Materials	13
2.2.2 The Antiferroelectric Perovskite NaNbO_3	14
2.2.3 The Antiferroelectric Perovskite AgNbO_3	16
2.2.4 Electrode Material LaNiO_3	19
2.3 Thin Films	19
2.3.1 Thin Film Growth	21
2.3.2 Strain	22
2.3.3 Literature Review on NaNbO_3 Thin Films	26
2.3.4 Literature Review on AgNbO_3 Thin Films	27
3 Experimental Methods	31
3.1 Sample Preparation	31
3.1.1 Pulsed Laser Deposition	31
3.1.2 Photolithography	34
3.2 Analysis Methods	35
3.2.1 X-Ray Diffraction	35

3.2.2	X-Ray Photoelectron Spectroscopy	38
3.2.3	Leakage Current Characterisation	40
3.2.4	Measurement of the Polarisation	43
4	Experimental Procedures	47
4.1	Synthesis of Thin Films	47
4.1.1	PLD	47
4.1.2	Process	48
4.1.3	Photolithography Process	50
4.2	Sample Analysis	52
4.2.1	XRD	52
4.2.2	XPS	54
4.2.3	Leakage Current Measurement	55
4.2.4	Polarisation Measurement	55
5	Towards High Quality Thin Films	57
5.1	Motivation	57
5.2	NaNbO ₃	57
5.2.1	Achieving Phase Pure Films via Growth Parameter Optimisation . .	57
5.2.2	Heterostructures	59
5.2.3	Translation of the Growth to other Substrates	61
5.3	AgNbO ₃	62
5.3.1	Achieving Phase Pure Films via Growth Parameter Optimisation . .	62
5.3.2	Ag Compensation Method	67
5.3.3	Versatility of the Ag Compensation Method	72
5.4	Conclusion	75
6	Strain Impact on the Crystallographic Structure	77
6.1	Motivation	77
6.2	NaNbO ₃ Heterostructures	78
6.2.1	Strain State	78
6.2.2	AFE versus FE Structure	83
6.3	AgNbO ₃	88
6.3.1	Strain State	88
6.3.2	AFE versus FE Structure	89
6.4	Conclusion	91

7	Electrical Characterisation	95
7.1	Motivation	95
7.2	Leakage Current Reduction	96
7.3	Polarisation versus Electric Field Behaviour	98
7.4	Conclusion	101
8	Final Conclusion & Outlook	105
	Bibliography	I
	Acknowledgements	XVII
	Appendix	XIX
	List of Publications and Conference Contributions	XXVII
	Curriculum Vitae	XXIX

List of Tables

4.1.1 PLD parameters for the growth of LaNiO_3 thin films.	50
5.2.1 PLD parameters for the growth of NaNbO_3 thin films from literature.	58
5.2.2 Optimised PLD parameters for the growth of NaNbO_3 thin films.	60
5.2.3 Lattice parameters of NaNbO_3 and the substrates utilised for NaNbO_3 growth.	62
5.3.1 PLD parameters for the growth of AgNbO_3 thin films from literature.	64
5.3.2 Cation stoichiometries of thin films grown from an AgNbO_3 target with an Ag compensation layer.	70
5.3.3 Lattice parameters of AgNbO_3 and the substrates utilised to grow AgNbO_3	72

List of Figures

2.1.1 Classification of the 32 point groups.	6
2.1.2 Characteristic properties of an FE material.	9
2.1.3 Characteristic properties of an AFE crystal.	11
2.2.1 The cubic perovskite structure ABO_3	12
2.2.2 Unit cell of the antiferroelectric P- and ferroelectric Q-Phase of $NaNbO_3$	14
2.2.3 P-E behaviour of $NaNbO_3$ as single crystal and as a polycrystalline ceramic.	16
2.2.4 Crystal structure of $AgNbO_3$ refined from neutron diffraction data.	17
2.2.5 Displacement current versus electric field behaviour for $AgNbO_3$ ceramics.	18
2.3.1 Dielectric breakdown strength of various dielectrics depending on their respective thickness.	20
2.3.2 Schematic illustration of various particle-substrate interactions during thin film growth.	22
2.3.3 Schematic illustration of Young's equation.	22
2.3.4 Schematic illustration of the three growth modes for different monolayer coverage Θ	23
2.3.5 Schematic of epitaxial growth of a film with a larger lattice parameter than the substrate.	24
2.3.6 Comparison of characteristic properties of a $BaTiO_3$ single crystal with $BaTiO_3$ thin films under compressive strain.	25
2.3.7 $\theta - 2\theta$ scans of $NaNbO_3$ thin films on different substrates.	27
2.3.8 Calculation of phase stability for $NaNbO_3$ thin films under epitaxial strain.	27
3.1.1 Schematic of the photolithography process.	35
3.2.1 Schematic of X-ray diffraction at lattice planes for the derivation of the Bragg equation.	36
3.2.2 Schematic band diagram of a capacitor structure under an applied electric field.	40
3.2.3 Equivalent circuits for the different polarisation measurement techniques.	44

3.2.4 Polarisation versus electric field curves for different scenarios encountered in dielectrics.	45
4.1.1 Illustration of the PLD device utilised in this thesis.	48
4.1.2 Layout of the photolithography mask utilised in this thesis.	51
4.2.1 Simplified sketch of a four circle diffractometer.	53
5.2.1 Impact of pressure variation on the film growth of NaNbO_3 thin films. . . .	59
5.2.2 XRD analysis of a NaNbO_3 thin film grown on the stack structure of $\text{LaNiO}_3/\text{SrTiO}_3(100)$	61
5.2.3 $\theta - 2\theta$ scans of NaNbO_3 thin films grown on different substrates.	63
5.3.1 Cation stoichiometry of AgNbO_3 thin films grown via PLD with variation of process parameters.	65
5.3.2 Cation stoichiometry of thin films grown from a stoichiometric AgNbO_3 target in dependence on various PLD parameters.	66
5.3.3 Schematic illustration of the method applied to compensate for the Ag deficiency in thin films grown from a AgNbO_3 target in PLD.	68
5.3.4 Evaluation of the impact of the Ag compensation layer on the film growth and phase formation of AgNbO_3	69
5.3.5 Dependence of the cation ratio on the Ag compensation layer thickness for different film thicknesses for growth of AgNbO_3 thin films on $\text{LaNiO}_3/\text{SrTiO}_3$	73
5.3.6 $\theta - 2\theta$ -scans of AgNbO_3 grown on different substrates, utilising the developed Ag compensation method.	73
5.3.7 RSM of 150 nm thick AgNbO_3 on $\text{LaNiO}_3/\text{SrTiO}_3(100)$, grown with a Ag compensation layer thickness of 60 nm.	75
6.2.1 $\theta - 2\theta$ scans of NaNbO_3 thin films grown on different substrates.	80
6.2.2 RSMs of NaNbO_3 grown on $\text{LaNiO}_3/\text{LSAT}$ around the 103 substrate reflection with a NaNbO_3 thicknesses of 91 nm and 105 nm.	81
6.2.3 RSMs of NaNbO_3 thin films grown on different substrates around the 103 substrate reflection as well as at the regions for the $\frac{3}{4}03$ and $103\frac{1}{4}$ superlattice reflections.	85
6.2.4 HRTEM micrographs of NaNbO_3 grown on SrTiO_3 with a thickness of 310 nm.	87
6.3.1 RSMs of AgNbO_3 thin films around the 103 substrate reflection on different substrates.	90
7.2.1 Leakage current depending on the applied field for an as-grown as well as heat treated NaNbO_3 thin films.	97

7.2.2 Fitting of the leakage current from the as grown sample as well as the annealed samples.	99
7.3.1 Polarisation and current density versus electric field curves for NaNbO ₃ thin films on different substrates.	102
8.0.1 Simplified model of the results from the structural and electrical results of the NaNbO ₃ thin films.	109
S1 θ - 2θ scans of thin films grown from a stoichiometric AgNbO ₃ target with variation of the Ag compensation layer thickness for a fixed film thickness.	XIX
S2 All RSMs around the 103 substrate reflection for NaNbO ₃ grown on LaNiO ₃ /LSAT with varying thickness.	XX
S3 All RSMs around the 103 substrate reflection for NaNbO ₃ grown on LaNiO ₃ /SrTiO ₃ with varying thickness.	XXI
S4 All RSMs around the 103 substrate reflection for NaNbO ₃ grown on LaNiO ₃ /DyScO ₃ with varying thickness.	XXII
S5 All RSMs around the 103 substrate reflection for NaNbO ₃ grown on LaNiO ₃ /GdScO ₃ with varying thickness. Reprinted with permission.	XXIII
S6 Comparison between the $\theta - 2\theta$ scans of NaNbO ₃ grown on LaNiO ₃ /SrTiO ₃ before and after the heat treatment.	XXIV
S7 Comparison between the RSMs of the 310 nm thick NaNbO ₃ film on LaNiO ₃ /SrTiO ₃ before and after the heat treatment.	XXIV
S8 RSM of NaNbO ₃ grown on LaNiO ₃ /LSAT around the 103 substrate reflection. Additionally, the areas for the expected superlattice reflection are shown.	XXV

Acronyms

AC Alternating current.

AFE Antiferroelectric(ity).

CVD Chemical vapour deposition.

DC Direct current.

FE Ferroelectric(ity).

FFT Fast Fourier transform.

HRTEM High resolution transmission electron microscopy.

HT Heat treated.

P-E loop Polarisation versus applied electric field curve.

PC Pseudo-cubic.

PFM Piezoresponse force microscopy.

PLD Pulsed laser deposition.

PVD Physical vapour deposition.

RSM Reciprocal space map.

SCLC Space charge limited current.

XPS X-ray photoelectron spectroscopy.

XRD X-ray diffraction.

1 Introduction and Motivation

Antiferroelectric (AFE) materials have recently garnered extensive attention due to their remarkable capacity to alternate between AFE and ferroelectric (FE) phases.[1, 2] This unique functionality has spurred interest in their applications, particularly in pulse power capacitors, DC-link capacitors for power electronics, high-energy density capacitors, and solid-state electrocaloric cooling.[2, 3, 4, 5, 6] The concept of AFE was introduced by Kittel's theory in 1951,[7] with lead zirconate (PbZrO_3) emerging as an early example of an AFE oxide.[8]

Despite the initial breakthrough, the exact definition of AFE remains a challenge, as the phenomenon is approached from various angles:[9] Phenomenologically, an AFE crystal exhibits a double hysteresis loop in the polarisation as a function of an electric field due to field-induced phase transitions. Energetically, the free energy of an AFE state closely resembles that of the FE state, allowing the latter to be induced in a non-polar crystal through the application of an electric field. From a structural standpoint, both AFE and FE materials emerge from the distortion of a non-polar high-symmetry reference phase. Non-polar phases become AFE if a low-energy FE phase arises from a polar distortion of the same reference structure, facilitating an easy transformation between the two phases.[1] Despite these insights, the comprehensive understanding of AFE materials lags behind their FE counterparts. While more than a thousand FE materials are known, only a few AFE systems have been deeply investigated.[10] Among these, PbZrO_3 -based AFE have reached the commercial market as a candidate for short-term energy storage.[11] Environmental concerns related to lead containing components, however, have sparked a search for lead-free alternatives.[5, 12]

One such alternative is NaNbO_3 , which presents a complex structural landscape and multiple phases with temperature variation.[13] At room temperature, it undergoes competition between AFE and FE phases, rendering it sensitive to factors like composition, starting chemicals, and external stresses.[14, 15] Achieving stable AFE states in NaNbO_3 is a fundamental step in exploring its properties. A key question revolves around how the structure, microstructure, and macroscopic functional properties evolve during phase transitions. This puzzle can be pieced together through a combination of structural characterisations and electrical analyses. Ultimately, the goal is to achieve reversibility

in phase transitions, akin to the behaviour seen in PbZrO_3 -based AFE. This endeavour involves stabilising AFE states, often achieved through compositional modifications. In this regard, computational approaches offer avenues for designing new AFE materials.[2] AgNbO_3 represents another known AFE material, which features a similar perovskite structure to NaNbO_3 as well as its complex structural landscape.[16] In contrast to NaNbO_3 , the AFE phase of AgNbO_3 is sufficiently stable to achieve the characteristic double-hysteresis loop of AFE materials.[15] In comparison to lead containing compounds, however, the performance of the energy storage density as well as its efficiency remain inferior.[2] Beyond the compositional optimisation, which has been conducted in-depth for the lead-free compounds,[15, 17, 18, 19] the manipulation of material properties through strain engineering has emerged as a versatile and promising approach across various scientific disciplines.[20] By exerting controlled mechanical stress on materials, various properties can be tailored and optimised, opening up avenues for the creation of novel functionalities in various devices. This strategy has witnessed notable success in enhancing FE properties, where even modest levels of strain can induce significant increases in key parameters like saturation and remanent polarisation.[21] However, the exploration into the influence of strain on AFE materials is relatively limited compared to its application in FE materials.[22] Despite the inherent connection between AFE and FE, only a few studies have directly investigated the impact of strain on AFE properties.[23] This gap in understanding presents a compelling opportunity to delve into the effects of strain on AFE materials. Such investigations hold the promise of not only improving the performance of AFE materials but also providing deeper insights into the mechanisms of the AFE effect itself. Strain engineering, as a means of affecting the AFE-FE phase balance, could offer new avenues for tailoring material properties. Combining strain engineering with other approaches, such as doping, may further amplify its potential for enhancing energy storage density and other desirable characteristics. In practice, introducing strain into bulk ceramic materials, particularly tensile strain, can be challenging.[24] This has led to the exploration of thin film approaches, which offer more controlled means of applying both compressive and tensile strain.[20] The choice of substrate in thin film deposition allows for the promotion of epitaxial strain, from compressive to tensile with varying magnitude. Additionally, thin films exhibit higher electric breakdown strengths, facilitating the investigation of electrical properties.[25] Meanwhile, the epitaxial growth of materials leads to a change in the unit cell by forcing the in-plane lattice parameters to coincide with those of the substrate. This leads to the question whether an epitaxial thin film can even exhibit AFE, as the in-plane lattice constants are restrained during the phase transition. If this relation is removed, the film would delaminate from the substrate. For bulk AFE, however, the phase transition is accompanied by a substantial change in the different lattice parameters and strain in

the material.[26] Thus, the transition from the AFE phase to the FE phase might be inhibited due to the epitaxial strain, and the material ceases its AFE properties in thin films. Coinciding with this assumption, so far, neither epitaxial thin films of NaNbO_3 nor AgNbO_3 have been found to exhibit the AFE state. While a scarcity of reports can be linked to the difficult fabrication of these materials as thin films,[27, 28] the few existing publications report the presence of a FE phase.[23, 29, 30] However, the origin of the shift to the FE phase remains unclear, with arguments for strain impact, size effects as well as epitaxy.[31, 32]

1.1 Purpose and Structure of this Thesis

This thesis is concerned with the thin film growth of high-quality, epitaxial thin films of the AFE perovskites NaNbO_3 and AgNbO_3 . Optimised films are subsequently utilised to investigate the impact of strain and epitaxy on the AFE properties.

Chapter 5 - *Towards High Quality Thin Films* is dedicated to the optimisation of thin film growth for both NaNbO_3 and AgNbO_3 . Challenges faced during this process are analysed and methods to overcome them are proposed. Finally, parameters and conditions for growth of high quality, epitaxial thin films are concluded.

In chapter 6 - *Strain Impact on the Structure*, optimised films with different strain states are investigated via structural means. The objective is to analyse the ground structure of the films and identify symmetries differentiating the AFE and FE structures, to visualise the feasibility of AFE epitaxial thin films. By performing this analysis for two different AFE materials, a trend for the formation of the ground structure in dependence on the induced strain is extracted.

In chapter 7 - *Electrical Characterisation*, the dielectric behaviour of NaNbO_3 in a capacitor structure is investigated to gain information about the phase stability and further knowledge about the strain impact. Meaningful results can only be obtained once the leakage current of these capacitor structures, which can overshadow the influence of polarisation, is minimised. The results of the electrical investigation can be utilised to formulate a combined hypothesis about strain and epitaxy impact on AFE properties with the results from the structural part.

The results of this thesis are preceded by a brief summary of the physical background in chapter 2, facilitating comprehension of the analysis conducted within this thesis. The characteristics of FE and AFE materials, the current comprehension of the AFE effect as well as the theory of thin film growth is covered. In chapter 3, the physics of the experimental methods, utilised in this thesis, are examined. Chapter 4 presents the experimental procedures, describing in detail, how the experiments are conducted.

Finally, Chapter 8 gives a short summary of this thesis and presents an outlook of its impact along with open questions that need to be addressed in the future.

2 Physical Background

This chapter recaptures literature which is fundamental to the understanding of the thesis. Section 2.1 introduces the general characteristics of dielectrics along with the concept of ferroelectricity (FE) and antiferroelectricity (AFE). Section 2.2 discusses the performance of various AFE materials in correlation with their crystal structure and gives an overview of the state of literature concerning the investigated AFE materials NaNbO_3 and AgNbO_3 as well as the utilised electrode material LaNiO_3 . Finally, section 2.3 describes the theory of thin film growth with focus on the epitaxial strain, concluding with a review of the current literature available for thin films of NaNbO_3 and AgNbO_3 .

The fundamentals described in the following are a specialised description with regards to the scope of this thesis. For a more in-depth description, the reader is referred to sources [33, 10, 1, 34, 35] upon which these fundamentals are based on.

2.1 Dielectric Materials

A dielectric is a non-conductive material that can be polarised by application of an external electric field. In contrast to metals, dielectrics feature ideally no mobile charge carriers which leads to the high electrical resistivity of this material class. Application of an electric field affects bound charges and shifts them out of their equilibrium positions, generating a polarisation response. There are four main mechanisms responsible for the polarisation:

- Electronic polarisation: Deformation of the electron cloud surrounding the atoms
- Ionic polarisation: Shifts of ions from their equilibrium positions
- Orientation polarisation: Re-orientation of existing dipoles within the material
- Space charge polarisation: Accumulation of mobile charges at interfaces

Depending on the crystal symmetry, additional effects like piezo- and pyroelectricity can occur in dielectrics. These can be considered in regard to the point groups and their respective symmetry, see Figure 2.1.1. Piezoelectricity describes the coupling of the me-

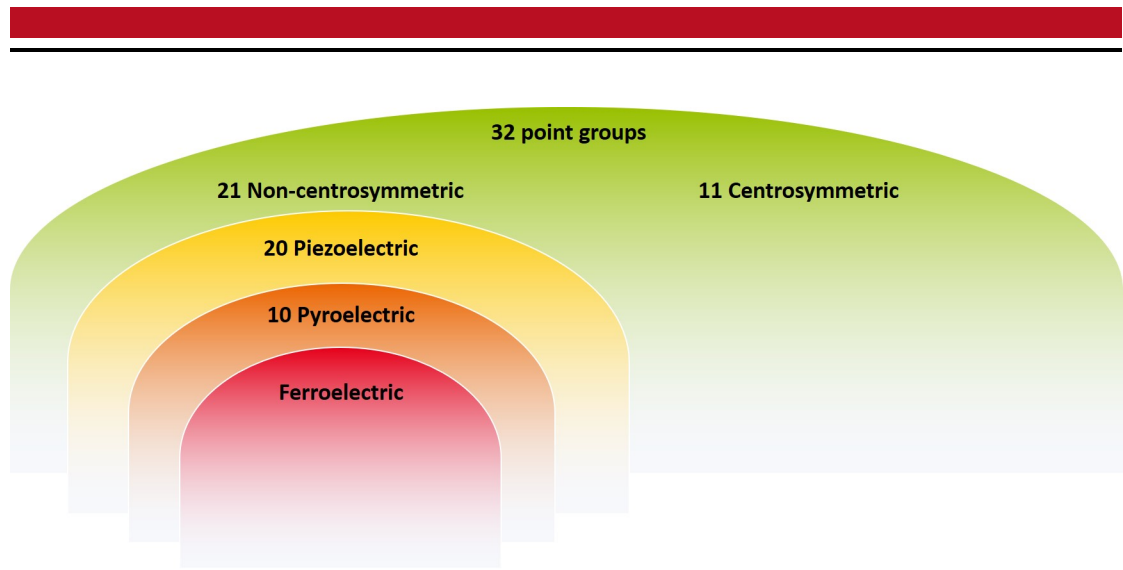


Figure 2.1.1: Classification of the 32 point groups into piezoelectric, pyroelectric and ferroelectric groups depending on the centrosymmetry.

chanical deformation to the electrical polarisation, i.e. by a mechanical deformation the polarisation of the material changes. This effect is reversible, meaning that the application of an electric field leads to a mechanical deformation of the material, termed the inverse piezoelectric effect. A necessary requirement for this effect is the presence of a polar axis, which results in an asymmetric charge distribution upon deformation of the unit cell. Thus, this effect only occurs in crystals without inversion symmetry, i.e. a non-centrosymmetric unit cell, which is true for 21 out of the 32 point groups. Out of these, 20 point groups show a polar axis and, hence, are piezoelectric.

On top of the requirements for piezoelectric materials, pyroelectric materials also show a nonzero polarisation along a polar axis without application of an electric field, so-called spontaneous polarisation. This polarisation is temperature dependent and, similar to the piezoelectric effect, a converse effect called the electrocaloric effect, i.e. the material changes temperature upon an external mediated change of polarisation, is also present. This occurs exclusively in polar crystal classes which applies to 10 out of the 20 piezoelectric point groups.

Materials which allow this polarisation to be reversed along the polar axis by application of an electric field are then called ferroelectrics (FE). This group is a subgroup to the pyroelectrics, as no additional symmetry breaking is required. Thus, all FE are necessarily pyroelectric, while pyroelectric materials are only considered to be FE if the reversal of the polarisation is associated with small lattice distortions. This is essential as the material tends to have an electrical breakdown if the barrier between the different states

is too large. Therefore, the classification of whether a pyroelectric is a FE is a matter of experimental limitations rather than crystallographic arguments, contrary to the previous classification of piezoelectrics and pyroelectrics. As a result, all FE are pyroelectric and all pyroelectrics are piezoelectrics while the converse is not always true. FE will be discussed in more detail in the following chapters.

2.1.1 Properties of Dielectrics

The polarisation \vec{P} of a dielectric is the response to an applied external electric field \vec{E} . The magnitude of this polarisation is dependent on the material and linked to the applied electric field via its electric susceptibility χ_e and the electric permittivity of free space $\epsilon_0 = 8.854 \cdot 10^{-12} \text{ F} \cdot \text{m}^{-1}$:

$$\vec{P} = \epsilon_0 \cdot \chi_e \cdot \vec{E} \quad (2.1)$$

The susceptibility is related to a material's electric permittivity ϵ_r via:

$$\epsilon_r = \chi_e + 1 \quad (2.2)$$

Both the electric permittivity and the electric susceptibility are second rank tensors, accounting for anisotropic effects. The permittivity of a material can be understood as a measure of its ability to store electrical energy in an electric field while the susceptibility describes the degree to which it can generate a polarisation in response to an applied electric field.

The electric displacement \vec{D} describes the displacements of bound charges in a material by an electric field \vec{E} :

$$\vec{D} = \epsilon_0 \cdot \vec{E} + \vec{P} = \epsilon_0 \cdot \epsilon_r \cdot \vec{E} \quad (2.3)$$

When alternating fields are applied to a dielectric, the movement of its electrical charges leads to the dissipation of energy in form of heat. This is termed dielectric loss and quantified by the loss tangent $\tan(\delta)$ of the complex permittivity:

$$\tan(\delta) = \frac{\epsilon''}{\epsilon'} \quad (2.4)$$

with ϵ' and ϵ'' as the real and imaginary parts of the permittivity, respectively. In an ideal case without any losses, $\tan(\delta)$ would be zero.

When a dielectric is placed between two metal electrodes, a parallel plate capacitor in a metal/insulator/metal (MIM) stacking is created which can store charges q under an

applied voltage U . The amount of charges it can store is referred to as its capacitance C and can be expressed with regards to the electric permittivity of the dielectric:

$$C = \frac{q}{U} = \epsilon_0 \cdot \epsilon_r \cdot \frac{A}{t} \quad (2.5)$$

where A corresponds to the area of the electrodes and t to the thickness of the dielectric, i.e. the electrode separation. The energy E which can be stored in a MIM capacitor is then given by:

$$E = \int_{Q_0}^{Q_{Max}} U(q) dq = \int_{Q_0}^{Q_{Max}} \frac{q}{C} dq \quad (2.6)$$

For the case of linear dielectrics, i.e. materials whose permittivity is independent of the electric field, this can be further simplified to Equation 2.7, while for non-linear dielectrics, the capacitance is also a function of the applied voltage and, hence, this simplification is not applicable.

$$E = \frac{1}{2} \cdot C \cdot U^2 \quad (2.7)$$

2.1.2 Ferroelectricity

Ferroelectricity (FE) was discovered in Rochelle salt in 1920 by J. Valasek.[36] Depending on the origin of the polarisation, FE material can be sorted into two different categories: oxygen-octahedral type or order-disorder type FE. For the former, the polarisation arises from the displacement of a cation within the surrounding oxygen octahedra, see Figure 2.1.2a. This is most commonly found in perovskite type compounds, which will be described in Section 2.2. For the latter, the polarisation originates from the ordering of structural elements, e.g. hydrogen bonds in Rochelle salt. For this thesis, the focus and all following fundamentals will be in regards to oxygen octahedral type FE.

FE describes dielectrics with two or more stable states of nonzero polarisation, which can be accessed by application of an electric field. In the absence of an electric field, a FE tends to form multiple domains of uniform polarisation to minimise the energy loss in form of depolarising fields. Thus, the resulting material has no overall polarisation as the contributions from the different domains cancel each other out. Once a unipolar electric field is applied, the polarisation aligns along the direction of this field and a hysteresis characteristic for FE materials forms in the polarisation versus electric field (P-E) graph, see Figure 2.1.2b: from the unpolarised state, the material follows the black dashed line, which results from the switching of the domains which were oriented in the opposite direction of the applied field and subsequent rotation of the domains towards the direction of the external electric field. Once all domains are aligned parallel to this direction, the

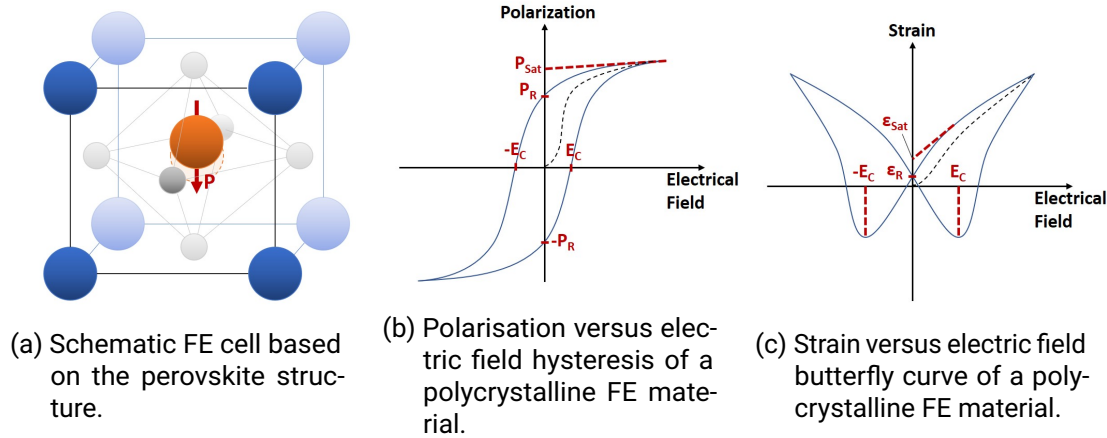


Figure 2.1.2: Characteristic properties of an FE material.

material exhibits the maximal polarisation, termed saturation polarisation P_{Sat} . Removal of the outer field leads to a small decrease in polarisation, as some domains reverse their polarisation due to elastic interactions. This so-called back-switching reduces the saturation polarisation to the remanent polarisation P_R , which is left when the external field is removed. Application of a field in the opposite direction leads to further decrease of the polarisation. Due to the long-range stabilisation of the polarisation in the material, however, the coercive field $-E_C$ has to be applied to return to a state with no overall polarisation. Further increase of the field in this direction leads again to a saturation, which possesses the same magnitude as before, only the direction of the polarisation vector is reversed.

As all FE materials are also piezoelectric, the polarisation is always coupled to a mechanical deformation of the material. Thus, along the change of the polarisation upon application of an electric field, also the strain inside the material varies, see Figure 2.1.2c. In the beginning, the strain increases until a saturation ε_{Sat} , is reached, as more and more domains switch in the same direction. Removal of the field leads to a remaining strain ε_R , similar to the polarisation behaviour. Reversal of the applied field further decreases the strain until it reaches a maximal negative value at the remanent field $-E_C$, after which it increases up to the saturation again. Due to its shape, the strain versus electric field behaviour of FE materials is termed the butterfly curve.

2.1.3 Antiferroelectricity

Antiferroelectricity (AFE) was first discovered in 1950 by Shirane and Sawaguchi,[37, 38, 39] and in the subsequent year, Kittel formulated the first theoretical work considering the existence of AFE materials.[7] In his work, he defined an AFE as two FE sublattices with antipolar order. While no material conforming to this definition has been found up to date, one fundamental property remains: the presence of no spontaneous polarisation in the unit cell, separating the class of AFE materials from FE. At this point, however, it should be noted, that the precise definition of an AFE remains nontrivial and a matter of discussion.[8]

A material which exhibits the above described characteristic antiparallel orientation of dipoles within a unit cell, exemplary shown in Figure 2.1.3a, is commonly referred to as an antipolar material rather than an AFE. In order to qualify as a true AFE, the material additionally needs to feature a FE phase with similar crystal structure. Upon application of an electric field, this FE phase is reduced in energy until the material transitions to the latter phase, see Figure 2.1.3b. This results in the characteristic double-hysteresis loop, which is commonly used as the identification of an AFE, see Figure 2.1.3c. As the application of the field makes the FE phase energetically favourable, the material transforms from the antipolar ground state to the FE phase when a critical field E_{FE} , is reached. After this transition, all dipoles are aligned parallel and the material reaches a polarisation saturation. If the field is removed, the antipolar phase becomes stable again and the material transforms back at a second critical field E_{AFE} . Thus for an ideal AFE, no remanent polarisation remains. It should be noted that, while the hysteresis reminds of the hysteresis in the FE polarisation versus electric field behaviour, compare Figure 2.1.2b, the origin is different: For a FE material, the material retains the polarisation due to the long-range order of the dipoles. On the other hand, the hysteresis for an AFE results from the phase transition between the antipolar and FE phase.

The difficulty of a precise definition for AFE materials originates in the connection between the macroscopic behaviour and its microscopic sources in form of crystal structure, and energetics. While initial theories were based on rigid sublattices with defined dipole moments,[7] real systems of oxide AFE are often not describable as a lattice of differentiable dipoles.[9] A more successful approach is the description via the soft mode theory established for FE, arriving at the lengthy definition by Rabe:[9] "...an antiferroelectric is analogous to a ferroelectric in that their structures are obtained through distortion of a non-polar high-symmetry reference phase. The distortion is nonpolar for antiferroelectrics, while polar for ferroelectrics. However, not all non-polar phases obtained are antiferroelectric unless there is an alternative low-energy ferroelectric phase obtained by a polar distortion of the same high-symmetry reference structure, which allows a small energy

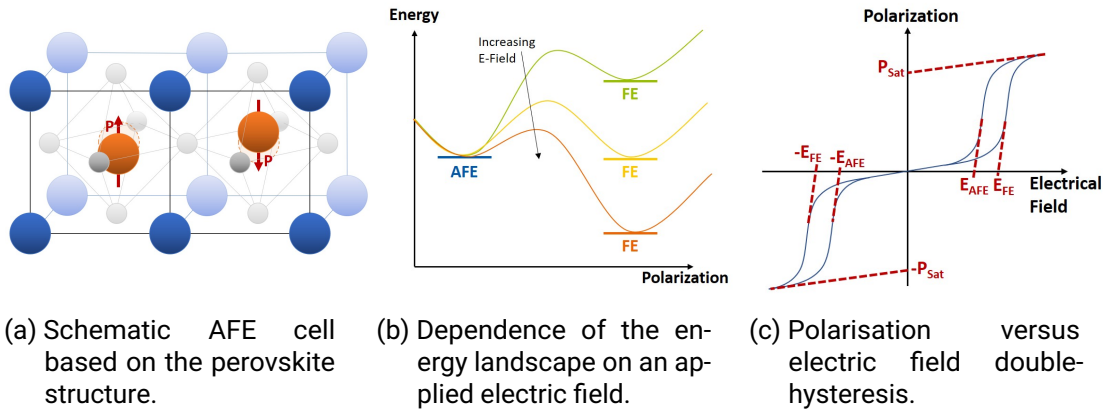


Figure 2.1.3: Characteristic properties of an AFE crystal.

difference and ease of transition between the two states.”.

For application as a dielectric in a capacitor structure, AFE benefit from the combination of a high saturation polarisation due to the switching to the FE phase and zero remanent polarisation. This results in a high recoverable energy storage density W_{rec} , which can be approximated by integration of the hysteresis loop: [40]

$$W_{rec} = - \int_{D_{Max}}^{D_0} EdD = - \int_{P_{Max}}^{P_0} EdP \quad (2.8)$$

The expression in terms of the polarisation P instead of the electric displacement D is an approximation valid for materials with large permittivity, meaning $D \approx P$. P_{Max} then corresponds to the polarisation at the maximum applied field E_{Max} .

This equation is only valid for the discharge, from P_{Max} down to P_0 , where the latter is zero for a true AFE. Due to the hysteresis, the total energy for charging W_{tot} is always larger than the energy returned during discharge, which results in an efficiency η of AFE smaller than one:

$$\eta = \frac{W_{rec}}{W_{tot}} = \frac{- \int_{P_{Max}}^{P_0} EdP}{\int_{P_0}^{P_{Max}} EdP} \quad (2.9)$$

From these equations it is obvious, that for a high W_{rec} large P_{Sat} with low P_0 (ideally 0), large breakdown strength E_b and small hysteresis, i.e. small difference between E_{FE} and E_{AFE} is desired.

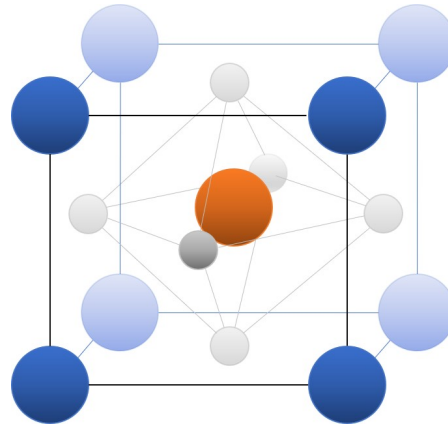


Figure 2.2.1: The cubic perovskite structure ABO_3 . The spheres at the corners, shown in blue, represent the **A cations**, the orange sphere in the centre the **B cation** and the oxygen anions are shown as grey spheres.

2.2 The Perovskite Structure

Along with the controversial nature of the AFE state, which materials are true AFE is similarly debated. Among the few materials which are classified as AFE materials, three classes are usually differentiated: oxide AFE, hydrogen bonded AFE and AFE liquid crystals. This work will be focused solely on oxide AFE, which commonly crystallise in the perovskite structure.

A perovskite has the chemical formula of ABX_3 with the cations A and B and anion X . The anion is commonly oxygen, which is why the perovskite structure is often simplified to ABO_3 . Its unit cell is shown in Figure 2.2.1. The enormous functionality of the perovskite structure stems from its variability: It can accommodate virtually all elements of the periodic table.[41] This leads to a wide range of properties this structure can exhibit, which can be individually customised by the respective choice of elements. The prototype perovskite features a cubic structure. Along with the variation of the cations, however, compensation for the different ionic sizes leads to other symmetries as well. An indicator of the stability of the perovskite structure depending on the different ionic radii is given by Goldschmidt's tolerance factor f :[42]

$$f = \frac{r_A + r_X}{\sqrt{2}(r_B + r_X)} \quad (2.10)$$

In this equation, r_i are the ionic radii of the respective elements. The ideal cubic perovskite has a tolerance factor of 1, while the cubic structure is generally stable in the range of $0.95 < f < 1.04$. If the A -cation ratio decreases, the tolerance factor decreases as well and the structure compensates by tilting of the oxygen octahedra. For decrease of the B -cation size on the other hand, this cation becomes too small to fill out the oxygen octahedra and, hence, is shifted away from the central position, creating a polarisation. Over time, many correlations between fundamental properties and the change in the tolerance factor have been unveiled, making it a popular design criterion to tailor properties of perovskites in a desired way.[41]

2.2.1 Antiferroelectric Materials

Since the cubic structure of a perovskite features no ion displacements in the ideal case and, hence, no polarisation, the cations have to be chosen appropriately to result in a localised polarisation to produce an AFE material. As described in the previous section, an increase of the tolerance factor is accompanied by a shift of the B -cation out of the central position. This structural compensation commonly results in a FE material and is termed a ferrodistorive instability. On the other hand, decreasing the tolerance factor has been observed to result in antiferrodistorive instabilities.[12] Utilising this trend has become one of the main design strategies in optimising the stability of the AFE phase of known AFE materials by creating solid solutions affecting the tolerance factor in the desired way. Notable compounds considered as AFE with this crystal structure include the lead containing materials which are usually modifications of PbZrO_3 (PZ), while new compositions based on PbHfO_3 (PH) and PbNbO_3 (PN) appeared recently as well. Lead-free alternatives on the other hand are commonly based on NaNbO_3 , AgNbO_3 or BiFeO_3 . [2] For some of these materials, however, doping is necessary to stabilise the AFE phase sufficiently to achieve the double hysteresis loop. Among AFE materials, the lead-containing compounds feature so far the best properties, with a stable double-hysteresis loop and high recoverable energy density W_{rec} .

Contrary to the lead-free compounds, pure PbZrO_3 , the first discovered AFE material, features such a high stability of the AFE phase at room temperature that the breakdown field is reached before the transition to the FE phase occurs.[38] Thus, the AFE double-hysteresis can only be observed at elevated temperatures or with doping which shifts the energy balance in favour of the FE phase.[39, 5] Suitable doping candidates are La and Ti, leading to the PLZT-system which is heavily investigated as a possible AFE material for application.[5] Due to the toxicity of lead, however, most research is focused on making lead-free materials viable for application. Thus, the focus of this work is on NaNbO_3 and

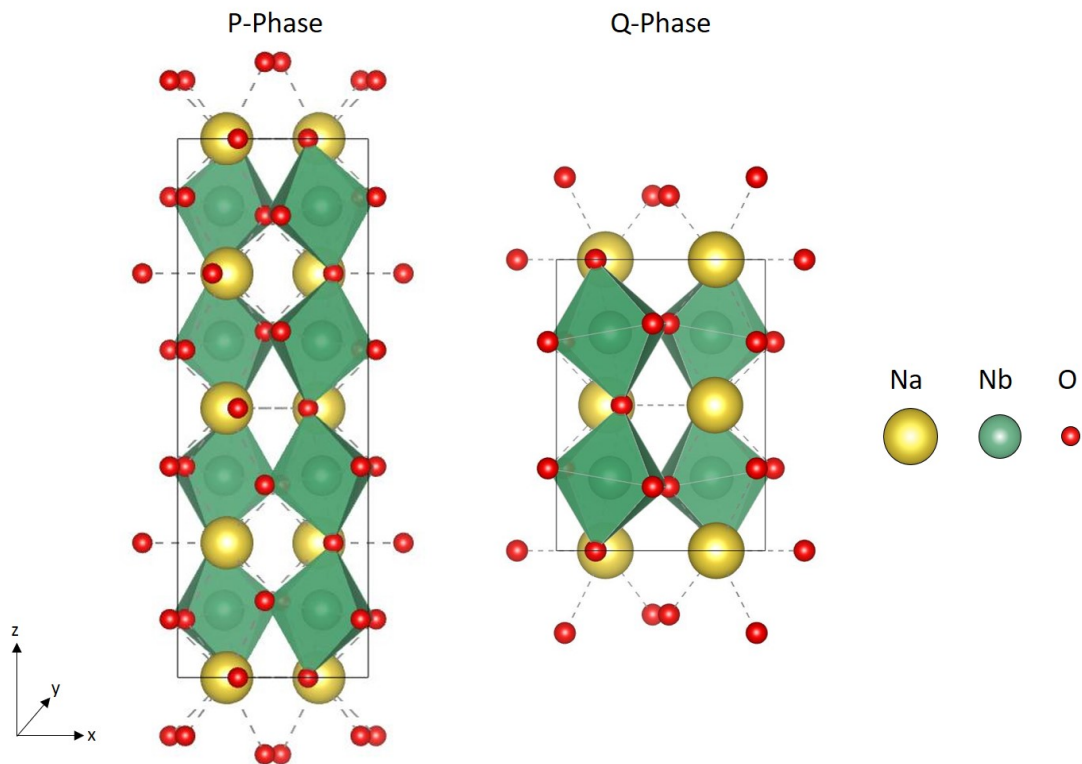


Figure 2.2.2: Unit cell of the antiferroelectric P- and ferroelectric Q-Phase of NaNbO_3 . [44]

AgNbO_3 .

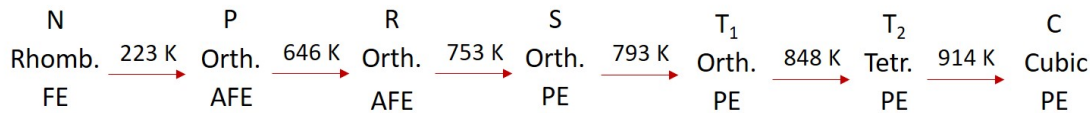
2.2.2 The Antiferroelectric Perovskite NaNbO_3

NaNbO_3 is an orthorhombic perovskite with lattice parameters of $a = 5.5687 \text{ \AA}$, $b = 15.523 \text{ \AA}$ and $c = 5.5047 \text{ \AA}$. [43]

Unravelling the fundamental structure and properties of NaNbO_3 has been proven to be challenging. First assumed to be FE, [45] it was shortly after shown to have an antipolar ground state. [46] Through much experimental effort, the latter hypothesis was confirmed and the material recognised as an AFE. [47, 13] One of the difficulties in defining the ground structure was shown to be the low energetic difference between the AFE P-phase and FE Q-phase. This can result in the coexistence of both structures depending on the

fabrication route, as the phase balance is affected by even the slightest off-stoichiometries or strains in the resulting sample.[48, 14] Computational works have confirmed the energetic similarity of the P- and Q-phase, with the P-phase being slightly favourable.[48] The AFE P-phase crystallises in the space group $Pbcm$ while the FE Q-phase is characterised to be $Pmc2_1$, see Figure 2.2.2. Due to the ion displacements and octahedral tilts, the unit cell of both phases is rotated by 45° in the a/c -plane compared to the simple perovskite unit cell. Considering the b -direction, the P- and Q-phases show a clear difference: while the P-phase features a lattice parameter four times that of the simple perovskite cell, the Q-phase only shows a doubling of it.[14] This allows for a clear differentiation between both structures, which is commonly exploited via diffraction techniques to identify the present phase in NaNbO_3 . [15]

Beyond the ambiguity of the phases at the ground state, NaNbO_3 undergoes many phase transitions with increasing temperature up to the cubic parent compound:[49, 50, 51]



Here, the first row denotes the shortcut for the respective phase, the second the crystal symmetry and the last the type of dielectric. The exact transition temperatures between the phases are very sensitive to the strain in the sample.[52]

For application of an electric field perpendicular to the b -axis of single crystal NaNbO_3 , a double-hysteresis loop can be achieved, see Figure 2.2.3a, while no polarisation response is detected parallel to it, see Figure 2.2.3b.[13] Meanwhile, for polycrystalline ceramics, the small energy difference between the AFE and FE phases leads to an insufficient driving force for the system to return to the AFE phase after application of an electric field. Thus, the P-E behaviour resembles a FE hysteresis rather than an AFE double hysteresis, see Figure 2.2.3.[53] Therefore, most research concerning NaNbO_3 is focused on the stabilisation of the AFE phase to make NaNbO_3 a viable alternative to the established lead-based AFE materials.[15, 2]

The strategies to affect the phase balance in favour of the AFE phase have been mainly centred around the doping approach. Hereby, all substitutions aim to stabilise the AFE phase via reduction of the tolerance factor.[2] Hence, alloying NaNbO_3 with the compounds CaZrO_3 , [54, 55] SrZrO_3 [53] (Figure 2.2.3c) and CaHfO_3 [56] has been shown to result in double-hysteresis loops, indicative of an increased stabilisation of the AFE phase. However, these compounds usually exhibit low dielectric breakdown strength

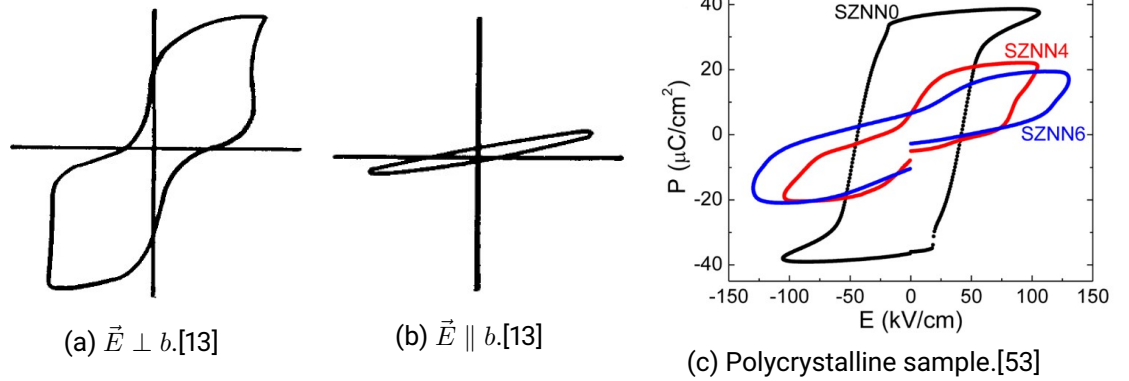


Figure 2.2.3: P-E behaviour of NaNbO_3 as a), b) single crystal and c) polycrystalline ceramic. For the latter, the X in $\text{SZNN}X$ refers to the percent of SrZrO_3 added to NaNbO_3 , i.e. $\text{SZNN}0$ corresponds to pure NaNbO_3 . Reprinted with permission.

as well as recoverable energy densities W_{rec} below $1 \text{ J} \cdot \text{cm}^{-3}$ due to a combination of a remaining remnant polarisation and large hysteresis leading to low efficiencies. [15] Therefore, further improvements were focused on minimising the hysteresis by aiming for FE relaxor properties. Combination of NaNbO_3 with Bi_2O_3 effectively increased the breakdown strength while reducing the hysteresis, leading to a W_{rec} of $4.03 \text{ J} \cdot \text{cm}^{-3}$ with $\eta = 85.4\%$. [57] Mixing with the relaxor FE $(\text{Bi}_{0.5}\text{Na}_{0.5})\text{TiO}_3$ lead to $W_{rec} = 7.02 \text{ J} \cdot \text{cm}^{-3}$ with $\eta = 85\%$, [58] while the highest energy density so far can be found in $0.76\text{NaNbO}_3 - 0.24(\text{Bi}_{0.5}\text{Na}_{0.5})\text{TiO}_3$ with $W_{rec} = 12.2 \text{ J} \cdot \text{cm}^{-3}$, which can be mainly attributed to the high breakdown strength of this material. [59]

2.2.3 The Antiferroelectric Perovskite AgNbO_3

AgNbO_3 shares many structural similarities with NaNbO_3 and features an orthorhombic perovskite structure with the lattice parameters $a = 15.64773 \text{ \AA}$, $b = 5.55199 \text{ \AA}$ and $c = 5.60908 \text{ \AA}$. [60]

Again, the exact space group remains heavily debated, with many works concluding the coexistence of two different space groups due to their similar energies. These are the space groups $Pbcm$ [61, 62, 63] and $Pmc2_1$, [60], shown in Figure 2.2.4, where the first is isostructural to NaNbO_3 and fully antipolar while the latter possesses a weak polarisation,

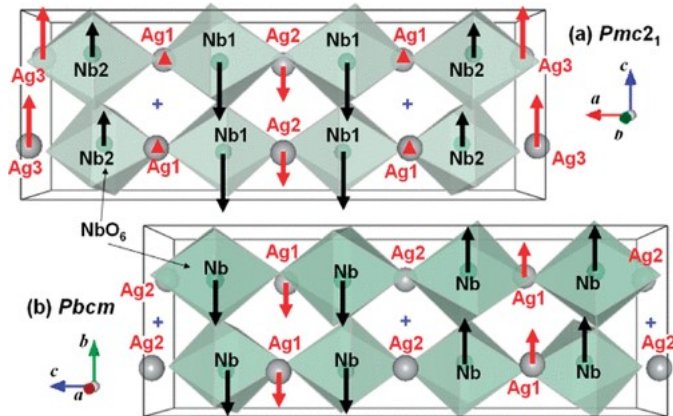
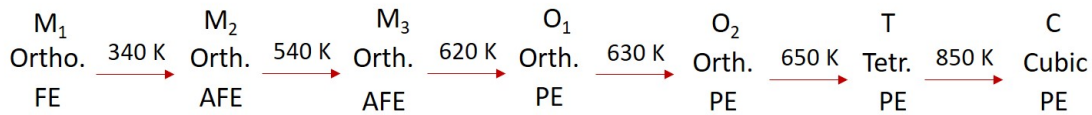


Figure 2.2.4: Crystal structure of AgNbO_3 refined from neutron diffraction data based on a) the $Pmc2_1$ and b) the $Pbcm$ structure. Ag and Nb are depicted by grey and green spheres, respectively, while the green polyhedra represent the NbO_6 oxygen octahedra. The red and black arrows denote the displacements of the Ag and Nb, respectively. Reprinted with permission.[60]

thus classifying AgNbO_3 as a non-compensated AFE.[64, 65]

Similar to NaNbO_3 , AgNbO_3 shows a series of phase transitions with increasing temperature, up to the parent cubic compound. The nature and symmetry of these phases has been extensively investigated and concluded as follows:[65]



$M_1 - M_3$ denote orthorhombic phases in rhombic orientation, while O_1 and O_2 represent the orthorhombic phases in parallel orientation.

Due to the non-compensated nature of the ground state, the polarisation versus electric field behaviour does not show the pure double-hysteresis loop characteristic of AFE materials and features a non-negligible remanent polarisation, see Figure 2.2.5.[16] However, as clearly recognisable from the hysteresis behaviour, AgNbO_3 switches back to the ground state after field application, in contrast to NaNbO_3 . This results from the larger energy difference between the ground state and the FE phase for AgNbO_3 . Hence, unlike for

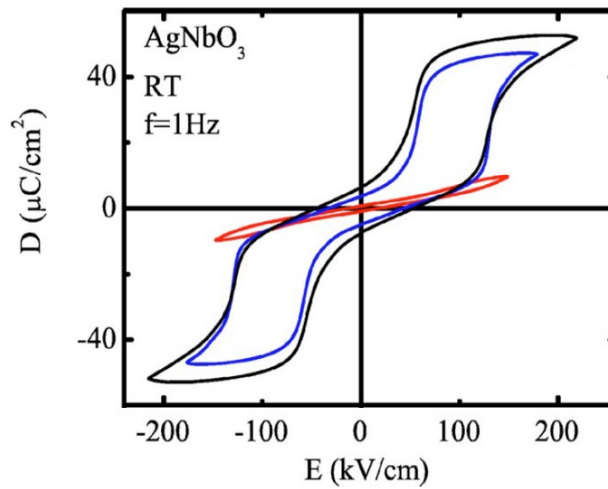


Figure 2.2.5: Displacement current versus electric field behaviour for AgNbO_3 ceramics. Reprinted with permission.[16]

NaNbO_3 , optimisation strategies focus on the improvement of the energy storage properties rather than the stability of the AFE phase.[15]

Both A-site and B-site doping has been extensively investigated to improve the energy storage properties for AgNbO_3 . Pure AgNbO_3 features already a W_{rec} of $2.1 \text{ J} \cdot \text{cm}^{-3}$, however the efficiency η reaches only 39%, due to the large hysteresis, as seen from Figure 2.2.5.[66] One of the most successful dopants is Ta on the B-site, leading to W_{rec} and η of $6.3 \text{ J} \cdot \text{cm}^{-3}$ and 90%, respectively, for the composition $\text{Ag}(\text{Nb}_{0.45}\text{Ta}_{0.55})\text{O}_3$. [67] Notably, the increased AFE stability cannot be attributed to a change in the tolerance factor, as the ionic radii for Nb and Ta are nearly identical. Rather, the authors attributed it to a lowering in electronegativity from Nb to Ta, while the improvement in the efficiency is ascribed to a relaxor behaviour of the high field FE phase.[67, 65] Meanwhile, A-site substitutions focus on heterovalent elements like Bi^{3+} [68], La^{3+} [69, 70] or Sm^{3+} [71, 72], which are simultaneously reducing the tolerance factor of the system while forming vacancies on the A-site to maintain charge neutrality in the system. From the increase in the switching field from the AFE to FE phase, it is inferred that the AFE phase is further stabilised due to the reduction of the tolerance factor. The highest energy density for AgNbO_3 based ceramics so far has been found for the combination of both approaches, with the system $(\text{Ag}_{0.94}\text{La}_{0.02})(\text{Nb}_{0.8}\text{Ta}_{0.2})\text{O}_3$ with $W_{rec} = 6.9 \text{ J} \cdot \text{cm}^{-3}$, however with an efficiency of only 61%. [73]

2.2.4 Electrode Material LaNiO_3

Beyond the AFE materials, the electrode material LaNiO_3 is also necessary for this work in forming parallel MIM capacitor structures for the electrical characterisation. The requirement for this electrode material beyond a high electrical conductivity is a similar structure to the AFE materials NaNbO_3 and AgNbO_3 . This is necessary to guarantee epitaxial growth (see Section 2.3) and achieve strained films.

LaNiO_3 is a rhombohedral perovskite which can be approximated via a pseudo-cubic lattice with a lattice parameter of $a_{PC} = 3.838 \text{ \AA}$. [74] Due to the overlap of Ni-3d with O-2p orbitals, the material exhibits metallic conductivity rendering it an interesting candidate for use in oxide electronics. [75, 76] Thus, it has become an established electrode material and as such has been shown to improve fatigue behaviour in the PLZT system. [77, 78]

The conductivity of LaNiO_3 has been found to be strongly dependent on the induced strain as well as oxidation conditions during fabrication. In this regard, tensile strain as well as Ni deficiency has been found to have a detrimental effect on the conductivity and, thus, should be avoided. Optimised thin film samples with low strain and near stoichiometric ion ratio can reach a resistivity below $100 \mu\Omega \cdot \text{cm}$. [79]

These properties combined with the isostructural perovskite structure have rendered LaNiO_3 a prominent electrode material in the field of AFE materials as well. [80, 81, 4]

2.3 Thin Films

The term 'thin film' has generally a very loose definition, referring to materials which are below $1 \mu\text{m}$ in one dimension, while the other two dimensions are usually above 1 mm . Along this reduction of the thickness in one dimension, many properties show drastic changes with some effects appearing solely in thin films. Hence, they have gained significant technological relevance and hold particular interest due to their integration potential in heterostructures for microelectronic and electromechanical devices. Moreover, thin film deposition enables the induction of substantial bi-axial lattice strains through epitaxial growth on substrates with lattice mismatch.

Among the properties showing significant change with thickness, the dielectric breakdown strength is of particular interest for AFE materials. As shown in Figure 2.3.1, it is significantly reduced with decreasing material thickness. Mediated mainly by defects, a reduction of the thickness lowers the probability of defects close to each other, effectively increasing the breakdown strength to an intrinsic level below $1 \mu\text{m}$. [25] This benefits the investigation into the AFE effect, since often the dielectric breakdown is achieved before switching to the FE phase is observed, resulting in the destruction

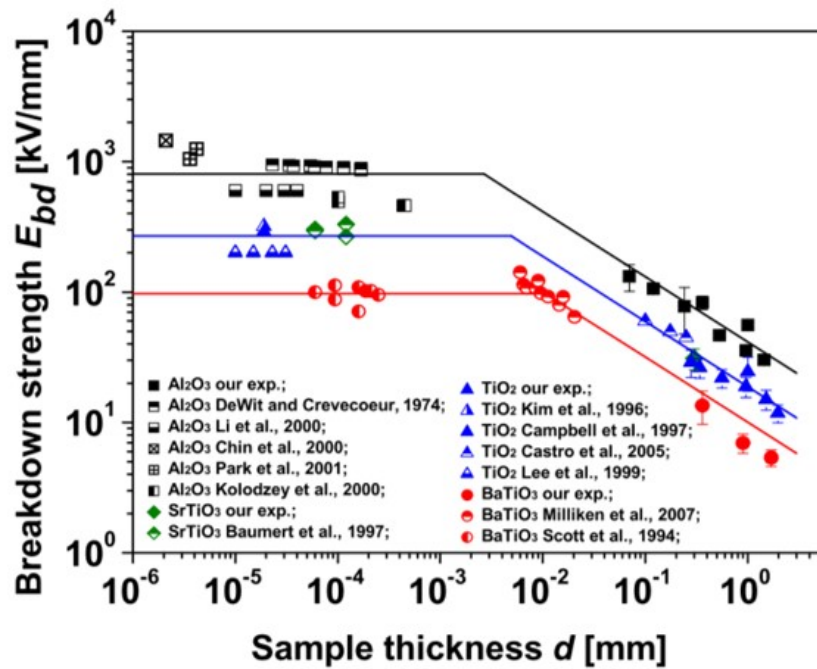


Figure 2.3.1: Dielectric breakdown strength of various dielectrics depending on their respective thickness. Reprinted with permission.[25]

of the sample. A direct effect of the increase in breakdown strength is the ability to achieve significantly increased W_{rec} of $23.1 \text{ J} \cdot \text{cm}^{-3}$ in $\text{Pb}_{0.85}\text{La}_{0.1}\text{ZrO}_3$ [82], $32.7 \text{ J} \cdot \text{cm}^{-3}$ for $\text{Pb}_{0.979}\text{Y}_{0.023}\text{Zr}_{0.56}\text{Sn}_{0.372}\text{Ti}_{0.077}\text{O}_3$ [83] or even $61 \text{ J} \cdot \text{cm}^{-3}$ for $\text{Pb}_{0.96}\text{La}_{0.04}\text{Zr}_{0.98}\text{Ti}_{0.02}\text{O}_3$ thin films.[84]

The impact of the reduction in one dimension on FE properties is a highly investigated topic, since the theory of FE as a continuum theory is only valid for length scales much longer than a lattice constant. Therefore, a critical thickness below which FE ceases to exist is expected. However, it is repeatedly confirmed that the theory of FE applies to films and heterostructures down to the nanoscale.[85] Modern investigations reveal films remaining FE even at a thickness of three unit cells (1.2 nm) when overcoming extrinsic effects like electrical and mechanical boundary conditions.[86] For AFE on the other hand, only few studies attempt to predict the impact of film thickness on the respective properties.[2] In a phenomenological study by Charnaya *et al.*, the phase transition behaviour as well as polarisation was discussed and a complete destruction of the AFE state below a critical thickness was described.[87] Eliseev *et al.* on the other hand predict a transition from

AFE to FE with decreasing film thickness.[88] However, experimental verification of these predictions is lacking so far.[2]

2.3.1 Thin Film Growth

Thin film synthesis relies on a 'bottom-up' approach, which utilises atoms or particles to assemble a thin film. Thus, first the desired elemental species have to be provided. Depending on how these particles are supplied, it is differentiated between physical and chemical vapour deposition (PVD and CVD, respectively). In CVD, thin films are grown via chemical reactions from appropriate precursors. In PVD, physical approaches are utilised to achieve free particles of the desired elements. Common examples are via temperature to reach sublimation, employed in molecular beam epitaxy, via bombardment of ions, achieved through high voltages in sputtering or via laser impact on the source material, for pulsed laser deposition (PLD).

These free particles are subsequently transported to a substrate, which is usually done in a reduced pressure environment. This substrate serves as a growth template for the accumulation of the different elemental species. Upon arriving at the substrate, various interactions can occur between the particles and the solid, see Figure 2.3.2. Depending on the energies involved, the particles can be reflected, penetrate into the substrate or be adsorbed. Lower energies promote the desired adsorption, too high energies upon impact are more likely to result in reflection or penetration or can even lead to the removal of atoms from the substrate or freshly formed thin film. A fraction of the adsorbed particles desorbs again, depending on the binding energy and substrate temperature. The others can diffuse over the substrate surface and nucleate to form a thin film.

Depending on the involved surface energies of the substrate and film, different growth modi can be realised. This is approximated by Young's equation, which describes the wetting of an ideal solid and is commonly utilised to describe thin film growth as well. It establishes a relationship between the interfacial tensions of the three phases involved: the liquid-vapour interface, the solid-vapour interface, and the liquid-solid interface, see Figure 2.3.3. Mathematically, Young's equation can be stated as:

$$\gamma_{sv} = \gamma_{sl} + \gamma_{lv} \cdot \cos(\theta) \quad (2.11)$$

where γ_{sv} is the surface tension between the solid and vapour phases, γ_{sl} is the surface tension between the solid and liquid phases, γ_{lv} is the surface tension between the liquid and vapour phases, and θ is the contact angle formed between the tangent to the liquid-vapour interface and the solid surface.

With this equation three different cases for the thin film growth can be identified. First,

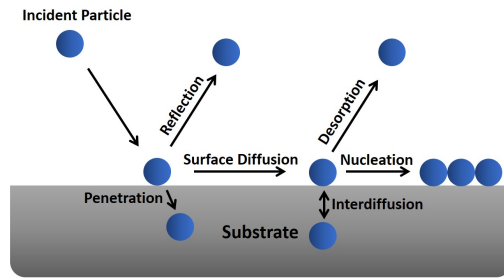


Figure 2.3.2: Schematic illustration of various particle-substrate interactions during thin film growth. Adapted from [89].

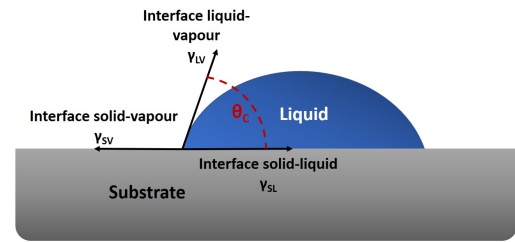


Figure 2.3.3: Schematic illustration of Young's equation.

assuming good wetting behaviour, i.e. $\gamma_{sv} = \gamma_{lv} + \gamma_{sl}$, θ would be 0° and the film grows by a layer-by-layer growth mode, also known as Frank-van der Merwe mode. For the case of $\gamma_{sv} < \gamma_{lv} + \gamma_{sl}$, θ would be larger than 0° and the new particles preferentially nucleate on already existing film areas, thus forming islands, known as Volmer-Weber growth mode. The last mode is a combination of the former ones, observed when the interface energies change, e.g. due to accumulating strain in the film. Then, the film may switch from initial layer-by-layer growth to island growth, also called Stranski-Krastanov growth mode. These different growth modes are illustrated in Figure 2.3.4 for increasing monolayer coverage Θ . [90]

2.3.2 Strain

Utilisation of strain to improve essential properties is a common strategy in many fields. Due to the strong coupling between FE and strain, FE properties can be greatly enhanced via strain engineering. [20] Hence, also AFE materials are expected to greatly benefit from this approach. However, the interplay between strain and AFE properties is complex due to interactions on multiple levels. First, strain has a direct impact on the phase balance as it affects the formation energy of both phases. Further, strain influences the phase transition from the AFE to the FE phase as well, as this transition is associated with a large strain variation. [26] Attempts to improve AFE properties in ceramics via strain engineering is solely focused on compressive strain due to the ease of its introduction. For uniaxial compression, it is generally found that the transition from the AFE to the FE phase shifts to higher fields indicating a stabilisation of the AFE phase. Simultaneously, the saturation

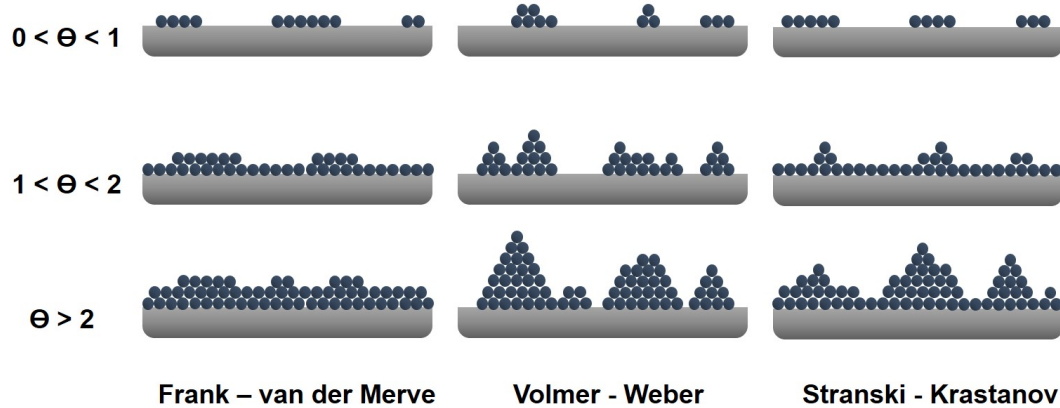


Figure 2.3.4: Schematic illustration of the three growth modes for different monolayer coverage Θ . Adapted from [90].

polarisation of the FE phase is reduced, albeit the measurements were conducted only along the axis of compression.[91, 24, 92]

An advantage to thin films is, that strain can be introduced via epitaxial growth. Epitaxial growth refers to a unique characteristic of thin film growth in which the deposited material adopts the same crystal structure and orientation as the underlying substrate, if suitable conditions are met. This enables the variation of strain induced in a material by an appropriate choice of substrate from compressive to tensile and with variation in the respective magnitude. This even enables strain levels where bulk materials would break from the tension.[20] Furthermore, since epitaxial strain is directly affecting the unit cell, see Figure 2.3.5, intrinsic changes of the material become accessible. In contrast, strain applied to bulk materials might be accommodated by extrinsic effects. Notably, the only strain state accessible in thin films is the bi-axial one, i.e. two dimensions are affected by the strain while the other dimension can relax freely to accommodate this strain. This so-called misfit strain ε between film and substrate can be calculated as follows:

$$\varepsilon = \frac{a_f - a_s}{a_f} \cdot 100\% \quad (2.12)$$

In this equation, a_f and a_s are the lattice parameters of film and substrate, respectively. For the case of orthorhombic cells, the strain can be anisotropic, creating the necessity to estimate the strain in both in-plane directions. The resulting compensation in the free

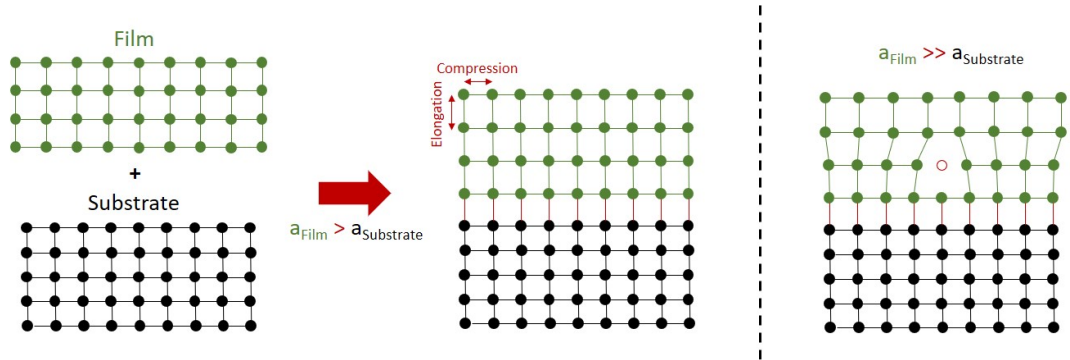


Figure 2.3.5: Schematic of epitaxial growth of a film with a larger lattice parameter than the substrate. *Right*: Exemplary formation of defect mediated relaxation to the bulk lattice.

direction is approximated by the Poisson effect:

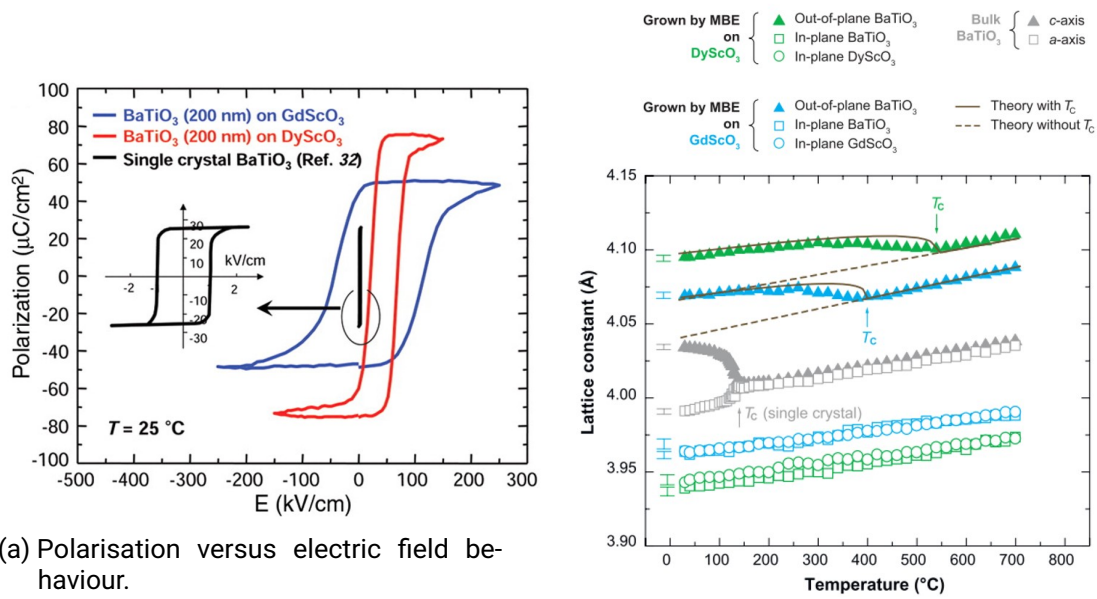
$$z = z_0 \cdot \left(\frac{2\nu}{\nu - 1} \cdot \frac{\varepsilon_x + \varepsilon_y}{2} + 1 \right) \quad (2.13)$$

This formula is derived from the general strain-stress relation of a three dimensional body and describes the resulting lattice parameter in the perpendicular direction z based on the unstrained value z_0 , the Poisson ratio ν and the strain in the other two dimensions, ε_x and ε_y , respectively. The Poisson ratio depends on the material, with ~ 0.3 for many perovskite materials.[93]

An essential requirement is consequently the availability of substrates with similar lattice parameters as the desired thin film to assure the possibility of epitaxial growth. Relaxation to the bulk structure occurs for films when the strain energy exceeds the formation energy of defects. The thickness at which this happens depends on the lattice misfit between film and substrate, and the film's specific defect formation energy.

The impact of epitaxial strain on the properties of FE materials has been investigated thoroughly. A strong correlation between the saturation polarisation P_{sat} and the magnitude of compressive strain was found. Figure 2.3.6a shows an increase in P_{sat} by a factor of more than 200 %.[21] Since every unit cell is compressed in-plane due to the epitaxial growth, the Poisson effect leads to an elongation in the out-of-plane direction. This gives the ions more space to displace in this direction, effectively leading to a higher achievable polarisation. This mechanism should be transferable to AFE materials as well, which would significantly profit from higher P_{sat} of their FE phase.[20]

Furthermore, the phase transitions are affected by strain as well. Figure 2.3.6b shows



(a) Polarisation versus electric field behaviour.

(b) Change of the lattice constant with temperature.

Figure 2.3.6: Comparison of characteristic properties of a BaTiO_3 single crystal with BaTiO_3 thin films grown under compressive strain. Reprinted with permission.[21]

the evolution of the lattice parameter with temperature for the previously discussed case of BaTiO₃. [21] This reveals the change of the phase transition from ~100 °C for a single crystal to nearly 600 °C for thin films under compressive strain on GdScO₃, indicating the possibility to tailor phase transitions by introducing strain.

A requirement for an AFE material is a reversible phase transition between the AFE and FE phases. This phase transition is mainly accomplished by rotation of the oxygen octahedra, however, a change of the lattice parameters is also observed. [48] Since both in-plane lattice parameters are locked with the substrate due to the epitaxial relation, a phase transition to the FE phase might be inhibited or occurs only parallel to a delamination of the thin film. Thus, thin film growth might inhibit the transition from the AFE phase to the FE phase and the material ceases its AFE properties. To validate this theory, the epitaxially strained state of a thin film needs to be verified before and after measuring a double-hysteresis loop, which has not been reported so far. Most investigations into AFE as films are rather concerned with thick films than thin films, where a relaxation to the bulk structure can be expected. For Pb-based thin films, several reports exist which measure AFE double hysteresis loops for fully strained films. [94, 95] However, no confirmation of the strain state is conducted after the measurements. Moreover, a trend towards FE behaviour is observed for thinner films, indicating a possible stabilisation of the FE phase.

2.3.3 Literature Review on NaNbO₃ Thin Films

Investigations on NaNbO₃ thin films have been relatively limited compared to bulk crystals and exclusively measured FE properties, particularly for films with micrometer-scale thicknesses. [96, 50, 29, 97] However, reproducible growth of stoichiometric thin films with high structural quality has proven to be challenging, attributed to the high volatility of sodium atoms. [50, 98] The choice of substrate strongly influences the symmetry, orientation, and polarisation direction of NaNbO₃ thin films. [99, 100, 101, 102]

Several deposition techniques have been employed to grow NaNbO₃ films, including meta-organic chemical vapour deposition (MOCVD), [100, 101] sol-gel process, [103] and PLD. [104, 105, 29, 98] However, these films often exhibit low electrical resistivity attributed to the high volatility of Na₂O. [105] To address this issue, Mn doping has been reported as an effective approach to reduce leakage current significantly. [102] Furthermore, the electrical properties of the films are influenced by deposition conditions, although a comprehensive understanding of their impact is still under investigation.

Schwarzkopf *et al.* conducted a study on 10 nm to 15 nm fully strained NaNbO₃ thin films grown on different substrates with high thin film quality, see Figure 2.3.7. Via piezoresponse force microscopy (PFM), they concluded that compressive strain potentially favours the FE phase, while tensile strain has the potential to stabilise an AFE phase. [100]

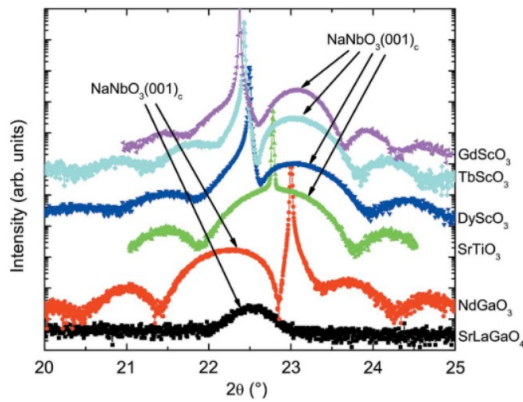


Figure 2.3.7: $\theta - 2\theta$ scans of NaNbO_3 thin films on different substrates. Reprinted with permission.[100]

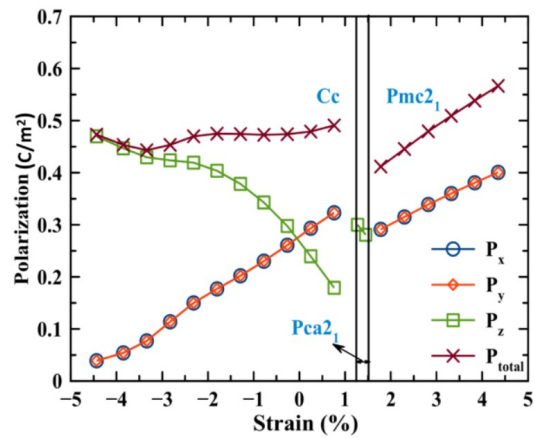


Figure 2.3.8: Calculation of phase stability for NaNbO_3 thin films under epitaxial strain. Reprinted with permission.[106]

However, only PFM was utilised for this analysis, thus, other methods are necessary for verification. Beyond theoretical predictions of the AFE state in NaNbO_3 thin films, experimental evidence supporting this claim is still lacking.[100, 106] In this regard, Patel *et al.* have investigated NaNbO_3 thin films via first principle calculations. They concluded an energy versus misfit-strain phase diagram, see Figure 2.3.8. With these calculations, they predict a monoclinic Cc phase with FE properties for compressive up to small tensile strain, an orthorhombic FE $Pmc2_1$ for large tensile strain as well as a potential orthorhombic AFE $Pca2_1$ phase in the narrow region between the other two phases.[106]

Similar to observations for thin film growth of Pb-based AFE materials, no clear evidence of a coexistence of epitaxial strain and AFE is available for NaNbO_3 . Moreover, Xu *et al.* have investigated size effects in free standing NaNbO_3 thin films and concluded a transition from the bulk AFE phase to a FE phase below 40 nm, based on indirect characterisation techniques.[32]

2.3.4 Literature Review on AgNbO_3 Thin Films

Unlike their ceramic counterparts, many AgNbO_3 thin films exhibit FE rather than AFE properties, similar to observations on NaNbO_3 thin films. Meanwhile, experiments con-


cerning the strain impact on the phase balance for bulk ceramics have shown that the AFE phase can be successfully stabilised via hydrostatic pressure.[107] Computational studies similarly reveal a potential stabilisation of the AFE phase by in-plane compressive strain.[108] Thus, the possibility of manipulating the stability of AFE or FE phases via film thickness and epitaxial strain is indicated, however, experimental results indicate that the epitaxy benefits the FE phase. Meanwhile, the scarcity of reports on high-quality AgNbO₃ thin films makes it difficult to obtain a clear picture regarding the strain impact on the phase balance. This scarcity appears to be caused by the challenging synthesis of AgNbO₃ materials.[109] Previous studies have mainly focused on AgNbO₃ thick films synthesised through techniques such as PLD[110, 111, 112, 28, 107, 83] and chemical solution deposition.[111, 113] However, these samples are not suitable for studying the impact of strain because the films are typically polycrystalline and relaxed to the bulk structure at thick film thicknesses.

Sakurai *et al.* synthesised AgNbO₃ thick films on SrTiO₃ substrates with varying orientations, revealing diverse P-E hysteresis behaviour. On SrTiO₃(100), the AgNbO₃ films exhibited AFE behaviour while, conversely, films deposited on SrTiO₃(110) displayed AFE behaviour at 150 kV · cm⁻¹ and ferroelectric (FE) behaviour above 200 kV · cm⁻¹. Moreover, AgNbO₃ films grown on SrTiO₃(111) demonstrated FE behaviour.[110] These trends are confirmed by publications from Ma *et al.* [107] for growth on SrTiO₃(100) and Ahn *et al.* for growth on SrTiO₃(111) substrates.[83]

Shu *et al.* utilised the chemical solution deposition method to fabricate AgNbO₃ films on Pt/Ti/SiO₂/Si substrates, which exhibited an AFE *M2* phase at room temperature. However, these films did not exhibit double P-E loops due to a small breakdown strength (E_b) of less than 110 kV · cm⁻¹. [113]

Finally, in a noteworthy study by Zhang *et al.*, the potential of AgNbO₃ thin films was demonstrated.[28] Thin films of AgNbO₃ were grown on SrTiO₃ substrates with a thickness of 400 nm. They exhibited AFE behaviour and a remarkable recoverable energy density of 5.8 J · cm⁻³, nearly three times higher than for pure AgNbO₃ ceramics, which typically have recoverable energy densities ranging from 1.5 J · cm⁻³ to 2 J · cm⁻³. [66, 17] This finding highlights the promising energy storage capabilities of AgNbO₃ thin films, while the strain is expected to not contribute to this result due to the large thickness.

Still, achieving the characteristic double P-E loops in thin films remains a challenge. The stability of the AFE phase in thin films is clearly affected by the epitaxy, with only little information available on the impact of the respective choice of substrate. Thus, adjusting the substrate can potentially enhance the AFE stability and enable the realisation of typical double P-E loops and high energy storage performance in thin films. Further exploration of pure AgNbO₃ and NaNbO₃ thin films can deepen our understanding of their intrinsic nature and offer valuable insights for developing thin films with improved energy storage



capabilities.

3 Experimental Methods

This chapter introduces the fundamental working principles of the various experimental techniques which are utilised in the process of this thesis. It is separated into sample preparation and analysis methods.

3.1 Sample Preparation

The samples presented in this thesis are exclusively fabricated by Pulsed Laser Deposition (PLD). Thus, this method is described in detail to facilitate the understanding of the various parameter studies applied to improve thin film growth of NaNbO_3 and AgNbO_3 . For electrical analysis of the samples, fabrication of a parallel capacitor structure is required. This is enabled by a combination of growing a bottom electrode consisting of LaNiO_3 between substrate and thin film and manufacturing top contacts with defined sizes. The latter are structured via photolithography and subsequent sputtering, which is discussed in the second part of this section.

3.1.1 Pulsed Laser Deposition

Pulsed Laser Deposition (PLD) is a thin film deposition technique that involves the use of high-energy laser pulses to ablate a target material and deposit it onto a substrate. In PLD, a laser beam is focused onto a target material, causing rapid heating and vaporisation of the target surface. This results in the generation of a plasma plume consisting of target atoms, ions, and clusters.[114, 115, 116]

The interaction between the laser and the target can conclude with an equilibrium process, thermal evaporation or an out-of-equilibrium process, termed non-thermal ablation. Which process occurs depends on the laser fluence ϕ , which needs to be above the ablation threshold, to enable non-thermal ablation, which is desired for PLD. ϕ is the energy density of the laser beam and can be calculated via the laser energy E and the laser spot size A :

$$\phi = \frac{E}{A} \tag{3.1}$$

A range of optics is employed in the beam path up to the target to focus the laser spot on a predefined size and control the energy of the laser beam.

The impact of the laser on the target surface causes a strong electronic excitation. The resulting electric field is sufficient to explosively eject ions out of the target and form a directed plume along the surface normal of the target. The rate of this ejection is sufficiently fast that phase separation does not occur, resulting in one of the prime advantages of PLD, which is the stoichiometric transfer even for complex multicomponent systems.[117]

The plasma plume expands towards the substrate due to Coulomb repulsion and recoil from the ejection process.[115] While PLD is classified as a vacuum process, regularly a gas atmosphere is introduced into the system, which serves to control the kinetic energy of the particles or even as a reactive species for the film growth, commonly oxygen for oxide thin films.[114] While PLD generates a deposition flux within 10 eV to 40 eV,[118] which is ideal for promoting surface diffusion and film growth, high-energy tails can lead to implantation, causing significant disruption to the film's crystallinity. Particles with energies exceeding ~ 50 eV can induce resputtering of the atoms at the film surface.[118] Aside from a reduction of the effective deposition rate this can alter the stoichiometry of multielemental films as certain elements are preferentially resputtered. Such preferential resputtering effects have been observed in PLD of $\text{Pb}(\text{Zr,Ti})\text{O}_3$ under low oxygen background pressures, leading to reduced Pb concentration.[119] Introduction of a background gas shifts the entire kinetic energy distribution towards lower values, rendering the fraction of particles with energies above the optimum range negligible. The presence of the background gas hampers the effectiveness of all plume species in promoting surface diffusion.[118] This is usually compensated by an energy supply to the diffusing species in form of substrate heating. Furthermore, significant increases in background gas pressure cause the plume to scatter significantly, leading to a decrease in deposition rate and a less directed plume trajectory.[115]

In the following, the different parameters affecting the PLD process and their respective impact are summarised:

- **Laser fluence ϕ :** For PLD, sufficient energy is necessary to allow for non-thermal ablation, i.e. the fluence has to be above the material dependent ablation threshold. Below this threshold, stoichiometric ablation cannot be guaranteed due to different thermal evaporation of the constituting elements.[116] As scattering events and the resulting diffusion-like behaviour of the plume can lead to significant off-stoichiometries, higher fluences facilitate a stoichiometric transfer.[120, 121] On the contrary, many processes leading to off-stoichiometry upon arrival of the particles on the substrate surface only occur for non-thermalised particles and, hence, lower fluence would support stoichiometric growth in this regard.[121] Moreover, high

fluence can lead to explosive boiling and subsequent ejection of large particles which are to be avoided for smooth thin film growth.[122]

- **Chamber pressure p :** Propagation of the different elemental species is severely impacted by the chamber pressure. Heavy and light elements experience different scattering characteristics, leading to varying distributions.[123] Furthermore, light species are scattered to larger angles, leading to an enrichment of the heavier species along the plume normal.[120] In low pressures, many materials experience desorption after condensation on the substrate, leading to off-stoichiometries.[124] Higher pressures can facilitate integration into the growing films,[98] however, increased background pressure can also lead to particle formation and decreasing growth rates.[122] For oxide materials, precise control of the oxygen content via the background pressure is essential,[124] limiting the available pressure window further.
- **Substrate-to-target distance d_{S-T} :** The distance from the target to the substrate affects the number of collisions between the travelling ions and atoms with the gas phase. As described above, a certain amount of collisions are desired to reduce the energy of the particles, hence, this parameter is strongly coupled with the chamber pressure. Too low distances increase the frequency of high-energy particles impinging and damaging the film, while too large distances lead to diminishing growth rates.[116, 125]
- **Laser repetition rate f :** The condensation of atoms on the surface of the substrate occurs on a time-scale which is much smaller than repetition rates of the laser pulses, which are commonly in the range of several Hz. Thus, the repetition rate of the laser usually has only minor influence on the film growth, except for cases with long relaxation times for surface diffusion, i.e. low substrate temperatures. In these cases, new material can arrive before atoms reach their equilibrium positions leading to pile up at multiple nucleation sites and, hence, island growth is often observed.[118, 124]
- **Substrate temperature T :** The heating of the substrate is utilised to facilitate surface diffusion, allowing the material to form single-crystals with minimised defect densities.[118] PLD at room temperature usually leads to amorphous films. With increasing temperature polycrystalline and single-crystalline films can be achieved.[122] However, high temperatures can lead to the activation of bulk diffusion as well as re-evaporation, which, due to its dependence on the atom species, results in changes of the film stoichiometry.[125]

Beyond these parameters which are most relevant for this thesis, many more influence the film growth but are difficult to identify since the PLD process remains highly debated. For a more detailed description, see sources [115, 118, 124, 125].

Still, PLD offers several advantages as a thin film deposition technique. It allows precise control over the composition, stoichiometry, and thickness of the deposited films. It is also suitable for depositing a wide range of materials, including metals, oxides, and complex compounds. Additionally, PLD enables the growth of epitaxial films with good crystalline quality, making it valuable for research and applications in fields such as electronics, optics, and energy devices.[117]

3.1.2 Photolithography

Photolithography is a fabrication process that utilises light to transfer a pattern onto a photosensitive material. This technique is widely used for high-precision patterning in various industries, including microelectronics, nanotechnology, and integrated circuit manufacturing.

The process consists of several steps, illustrated in Figure 3.1.1. First, the film or substrate is covered by a photoresist, typically via spincoating with subsequent heating to evaporate the liquid, resulting in a homogeneous layer of photoresist on the material. Photoresists are polymers which undergo a structural change upon exposure to UV light.

This is utilised in the next step, where the material is exposed to UV light with a mask shadowing parts of the photoresist from the illumination. These illuminated parts of the photoresist react differently with the corresponding developer liquid. Depending on the type of the photoresist, either the illuminated parts or the shadowed parts are removed, when the sample is immersed in the developer liquid. The first case corresponds to a positive photoresist while the latter refers to a negative photoresist.

Then, the whole surface is covered by another layer of material, which is commonly sputtered. For electrode patterning, gold is usually applied. The last step in the process is the lift-off. Utilising another chemical, often acetone, the remaining photoresist is dissolved. This leads to the removal of the material on top of the photoresist as well and only the desired structure remains on the film surface.

The thickness ratio between the additional layer and the photoresist is important: If the applied layer is too thick in relation to the photoresist, it cross-links the material in the gaps to the material on top of the photoresist and cannot be separated easily.

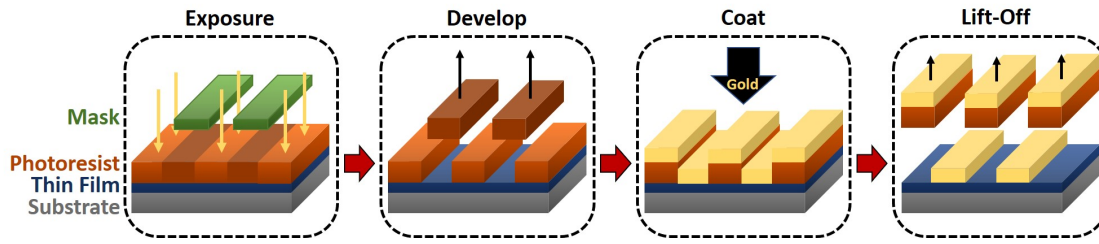


Figure 3.1.1: Schematic of the photolithography process exemplary for usage of a negative photoresist, separated into four steps.

3.2 Analysis Methods

The synthesised thin films are primarily analysed via X-ray diffraction (XRD) to determine the film's phase and quality, while X-ray photoelectron spectroscopy (XPS) is applied to characterise the stoichiometry of the thin films.

Further characterisation tools are concerned with the electrical behaviour of the thin films, including the leakage current through the dielectric film, the dielectric properties measured with a LCR meter and finally the polarisation behaviour in dependence on the electric field, which is obtained by a ferroelectric tester.

3.2.1 X-Ray Diffraction

XRD relies on the diffraction of X-rays from the lattice planes of a crystal. At certain angles, depending on the lattice spacing, the diffraction leads to constructive interference. This is described by the Bragg equation:[126]

$$n \cdot \lambda = 2 \cdot d_{hkl} \cdot \sin(\theta) \quad (3.2)$$

n is an integer, λ the wavelength of the X-rays, d_{hkl} the lattice spacing for the lattice plane indicated with the respective Miller indices h , k and l and θ the incident angle, see Figure 3.2.1. Thus, for a known wavelength, the lattice spacing can be extracted for an angle with constructive interference.[127]

Depending on the angles traversed and the angular ranges, different measurements are distinguished. In the following, the measurement types used in this thesis are described in more detail.[128]

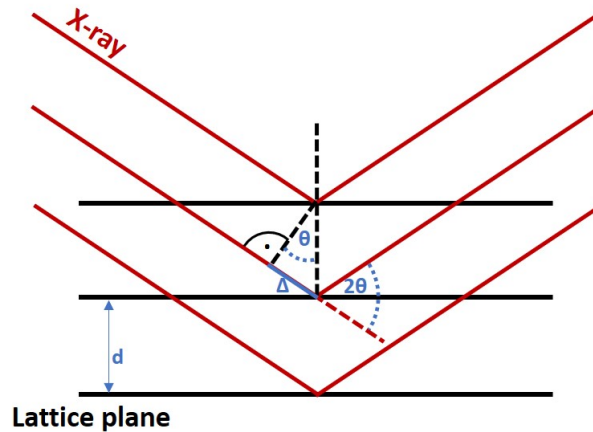


Figure 3.2.1: Schematic of X-ray diffraction at lattice planes for the derivation of the Bragg equation.

$\theta - 2\theta$ Scan

The $\theta - 2\theta$ scan is a special case of the $\omega - 2\theta$ measurement, which moves the incident angle ω and the detector angle θ simultaneously with the same speed. It is often used for epitaxial layers to determine the orientation, crystalline quality, phase, stress state, thickness and lattice constant of the investigated plane.[129] For this purpose, the optics are first aligned to the substrate lattice, i.e. the samples are positioned in the beam by moving z , ω and χ , which corresponds to the sample height, the tilt in the beam direction and the tilt perpendicular to that, respectively. In a subsequent measurement the angle ω corresponds to the angle of incidence in relation to the crystal planes within the substrate plane. For this measurement, reflections along one direction in reciprocal space are recorded. If the angle ω corresponds to the value of θ , then the measurement is called a symmetrical $\theta - 2\theta$ measurement. If the angle ω deviates by an angle $\Delta\omega$ from the value of θ , it is called an asymmetrical measurement. In the $\theta - 2\theta$ measurement, all reflections of parallel lattice planes are detected. Therefore, epitaxial relations in heteroepitaxy can be derived from the diffractograms.

If hkl -reflections of several orders are recorded, an exact determination of the lattice constants can be carried out via an extrapolation according to Nelson and Riley[130] for the case of parallel beam geometry. Furthermore, oscillations can form at reflections in

the diffractogram. These so-called Laue oscillations result from interference of coherently diffracted X-rays at the finite grating. If the grating periodicity is not extended far in the direction of measurement (e.g. in thin layers), the oscillations are visible in the X-ray diffraction pattern. From the spacing of the oscillations, the layer thickness, or more precisely the extent of the lattice planes that diffract coherently, can be calculated via the following equation:[131]

$$t = \frac{\lambda}{2(\sin(\theta_n) - \sin(\theta_{n-1}))} \quad (3.3)$$

$\sin(\theta_n)$ and $\sin(\theta_{n-1})$ denote the diffraction angles of the n^{th} and preceding oscillations and t denotes the calculated thickness from the Laue oscillations.

X-Ray Reflectivity

X-ray reflectivity (XRR) is based on the specular and total reflection of X-rays at an interface between two media with different refractive indices. In addition to the air/solid interface, internal interfaces of a medium can also be investigated.[132] From the determined reflectograms, information can be obtained in particular about the nature of the interfaces as well as the thickness and density of the layers. XRR corresponds to a $\theta - 2\theta$ measurement at low diffraction angles, typically in the range of $0^\circ \leq 2\theta \leq 6^\circ$. When X-rays enter from one medium through an interface into another medium with a different refractive index, refraction of the X-rays occurs. Constructive interference occurs when the path difference of the incoming and reflected radiation is a whole multiple of the wavelength of the radiation. This path difference depends on the expansion of the medium. From the total reflection angle θ_C , the density ρ can be determined via the following equation:

$$\rho = \frac{2\pi M \theta_C^2}{r_0 N_A Z \lambda} \quad (3.4)$$

The molar mass M , the atomic number Z , the Avogadro constant N_A , Bohr radius r_0 and the wavelength of the radiation λ are needed for the calculation.

Due to multiple reflections of the X-rays on different interfaces, oscillations are created in the intensity profile. These oscillations are called Kiessig fringes and their period is dependent on the thickness of the layers. Thus, X-ray reflectograms can be fitted by simulation in order to determine surface and interfacial roughness, as well as the film thickness. As the origin of these oscillations differs from that of the Laue oscillations, both may result in different film thicknesses if only parts of the film grow coherent.

Reciprocal Space Maps

If a series of measurements of several $\theta - 2\theta$ -scans is recorded with varying angles of incidence ω , a mapping of the determined intensities as a function of the angles 2θ and ω can be created. These images are called reciprocal space maps (RSM) since the angles are converted into directions of the reciprocal space. These maps are recorded in the vicinity of a known reciprocal lattice point. From the maps, the lattice plane spacing in the respective directions can be determined directly. However, since it measures a lattice plane of the material, information can only be obtained from two directions. Therefore, several reflections must often be mapped to determine the exact structure. A deformation of the reciprocal lattice point contains information about the film growth and quality of the epitaxial layer:

- An elongation perpendicular to the film surface results from a finite film thickness. Thus, the broadening in this direction shows a clear difference between film and substrate.
- A broadening parallel to the film surface can be observed if grain boundaries or island growth is present.
- A broadening in the direction of the scattering vector results from a variation of the unit cell parameters. This can be due to stress, defects or compositional changes in the film.
- A broadening perpendicular to the scattering vector stems from mosaicity in the film. This refers to the spread of the crystal plane orientations. This result coincides with a rocking curve measurement, for which the XRD system is focused on a film reflection and only ω is scanned in a small range.

3.2.2 X-Ray Photoelectron Spectroscopy

X-ray photoelectron spectroscopy (XPS) is a surface-sensitive technique used to analyse the elemental composition and chemical state of materials. It provides valuable information about the chemical bonding and electronic structure of a material's surface.[133]

In XPS, a sample is bombarded with X-rays, typically generated by a monochromatic X-ray source. These high-energy X-rays cause the ejection of core-level electrons from the sample's atoms. The kinetic energy of the emitted electrons E_{Kin} is then measured and used to determine the binding energy E_B of each electron:

$$E_B = E_A - E_{Kin} - \phi_S \quad (3.5)$$

where $E_A = h \cdot \nu$ is the energy of the X-ray photon, E_{Kin} is the kinetic energy of the electron and ϕ_S is the work function of the spectrometer.

The resulting binding energy is characteristic for each element and can be identified by comparison with measured standards from literature.[133]

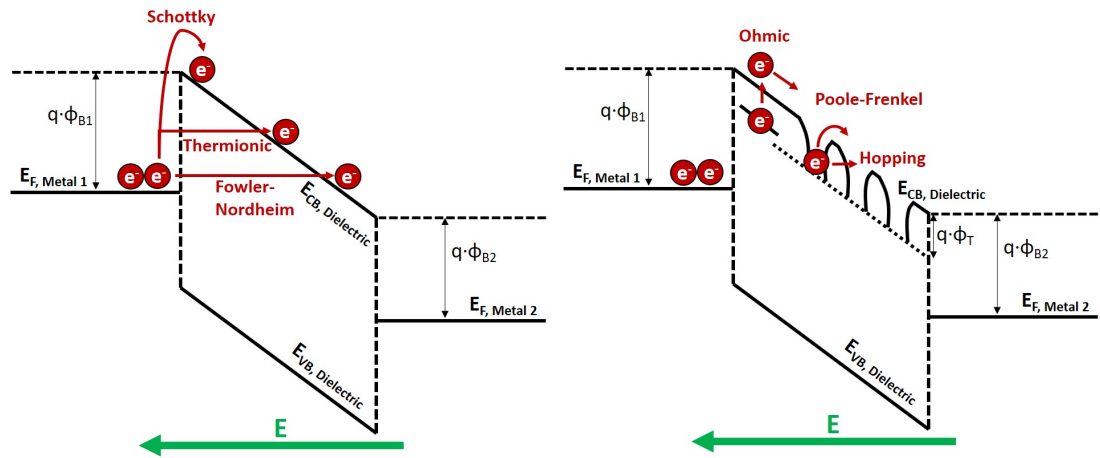
Due to the deviation of the final state from the initial state during photoionisation, various phenomena arise from the interaction between the escaping electron and the ionised system. These interactions give rise to additional peaks that need to be considered. Examples of such peaks include Auger peaks, shake-up peaks, plasmon peaks, and multiplet splittings. Auger peaks occur when outer shell electrons escape the sample powered by the energy generated by another outer shell electron filling the vacant core state. Shake-up peaks arise from the interaction between the hole and the escaping electron, which reduces the kinetic energy of the electron as it is attracted to the hole. Plasmon peaks result from the excitation of collective lattice vibrations by the escaping electron, leading to a reduction in its kinetic energy equivalent to the amount of the energy of the lattice vibration. Furthermore, when interactions occur between electrons in the core levels and unpaired electrons in the valence band, multiple final states are observed, resulting in spectra known as multiplet splittings. These processes often influence each other, making it challenging to identify the specific cause of the observed satellites in the spectra.

By analysing the spectra, valuable insights can be gained about the chemical state of elements, such as oxidation numbers of ions, bonding ratios, and coordination. This enables the identification and quantification of elements present on the surface. To achieve identification, the observed peaks are compared with reference values from literature.[133] The elemental ratios are calculated by comparing the detailed spectra of the elements. By comparing the measured intensity of each element I_i to the intensity of the other elements I_j , its concentration X_i can be calculated:[134]

$$X_i = \frac{I_i/S_i}{\sum_j I_j/S_j} \quad (3.6)$$

Additionally, the element specific sensitivity factors S_i are necessary, which account for element related variations in the photoelectron yield as well as device related variations. These are tabulated for most elements,[135] however, have to be calibrated to the specific device.[134]

The surface-sensitivity of XPS stems from the mean-free path of the photoelectrons inside the sample, which usually do not exceed several nm.[133] Thus, depending on the angle of the detector to the sample, photoelectrons of different total depths can be measured. For small detector elevation angles, the electrons need to traverse a path which is not along the surface normal, effectively limiting the measurement to smaller thicknesses.



(a) Electrode-limited conduction mechanisms. (b) Bulk-limited conduction mechanisms.

Figure 3.2.2: Schematic band diagram of a capacitor structure under an applied electric field. The principle of different conduction mechanisms are shown in red. Adapted from [136].

Comparison between measurements along the surface normal and smaller angles give an estimation of the depth distribution of different elements.

3.2.3 Leakage Current Characterisation

Essential for dielectric materials is a high electrical resistance leading to minimal current flow through the material. However, in real systems many mechanisms contribute to a current through the dielectric, making it necessary to identify and understand the corresponding mechanisms to minimise their contribution. In general, two types of leakage mechanisms in thin films can be differentiated: electrode-limited and bulk-limited conduction. The first depends on the electrical properties at the interface from the dielectric to the electrode, see Figure 3.2.2a, and the latter on the properties of the dielectric itself, see Figure 3.2.2b. [136] Based on the behaviour of the current density in dependence on the electric field, the present mechanism can be extracted. As some of the conduction mechanisms show a similar trend, fitting of the curves and calculation of the optical permittivity ϵ_{Op} can serve to differentiate these.

Electrode-limited mechanisms

- **Schottky emission:** When a metal is connected to an insulator, a potential barrier is formed if the work function of the metal ϕ_M is larger than the electron affinity of the insulator χ . Then, if no surface states are present, the Schottky barrier ϕ_B equals $\phi_M - \chi$. Thus, the energy necessary to overcome this barrier and inject charged carries with charge q into the insulator is given by $q \cdot \phi_B$. [137]

The current density J resulting from the Schottky emission is given by:

$$J = A^* T^2 \cdot \exp\left(\frac{-q(\phi_B - \sqrt{qE/4\pi\epsilon_0\epsilon_{Op}})}{k_B T}\right) \quad (3.7)$$

with q as the charge, ϵ_0 the vacuum permittivity, k_B the Boltzmann constant, T as the temperature and A^* is the effective Richardson constant. [136] Accordingly, a plot of $\log(J)$ versus \sqrt{E} gives a linear behaviour if the leakage stems from this mechanism. Then, the slope m of this linear plot can be used to calculate ϵ_{Op} :

$$\epsilon_{Op} = \frac{q^3}{4\pi\epsilon_0\epsilon_{Op}k_B^2 T^2 m^2} \quad (3.8)$$

As a result, Schottky emission is usually observed at higher temperatures, which are necessary to supply the energy for the emission of the electrons. To minimise the contribution of this mechanism, metals with large work function like gold or platinum are favourable as electrode materials. [136]

- **Fowler-Nordheim tunnelling:** In contrast to direct tunnelling, in Fowler-Nordheim tunnelling, the electrons do not penetrate the material completely but rather tunnel into the conduction band of the insulator, see Figure 3.2.2a. In contrast to direct tunnelling, this effect can occur also for thicker materials, however, large electric fields are necessary. [137]

The current density for this mechanism is given by:

$$J = \frac{q^3 E^2}{8\pi h q \phi_B} \cdot \exp\left(\frac{-8\pi\sqrt{2qm_T^*}}{3hE} \phi_B^{3/2}\right) \quad (3.9)$$

with m_T^* as the tunnelling effective mass in the insulator and h as Planck's constant. [136] Hence, for this mechanism, the plot of $\log(J/E^2)$ versus $1/E$ should be linear.

As contribution of tunnelling currents is only relevant for small distances, this

mechanism occurs predominantly at large electric fields, which lead to small distances into the conduction band. Since this mechanism is not temperature dependent it can be separated from Schottky emission when measuring at low temperatures.[136]

- **Direct tunnelling:** This mechanism describes the direct transfer of electrons through the insulator. As the probability of this mechanism is only relevant at very small thicknesses, it is commonly neglected for films used in capacitor structures.[136] For SiO₂ it has been shown that this mechanism is only significant at 3.5 nm and below.
- **Thermionic-field emission:** This mechanism describes a combination of the Schottky emission and the Fowler-Nordheim tunnelling, see Figure 3.2.2a. The electrons in this case are excited above the Fermi level, however their energy remains insufficient to surpass the energy barrier. At this level, they tunnel into the conduction band of the insulator, which requires a shorter distance than for the unexcited state.[136] This process exists only in a narrow regime between Schottky emission and Fowler-Nordheim tunnelling.[138] The current density from this mechanism can be expressed as follows:[136]

$$J = \frac{q^2 \sqrt{mk_B T} E}{2h^2 \sqrt{\pi}} \cdot \exp\left(-\frac{q\phi_B}{k_B T} + \frac{h^2 q^2 E^2}{96m\pi^2 k_B^3 T^3}\right) \quad (3.10)$$

Bulk-limited mechanisms

- **Ohmic conduction:** If mobile charge carriers are present, they move under an applied electric field, which is known as Ohmic conduction. The relation between the current density and the applied field is linear, $J = \sigma E$, with σ as the conductivity.[137] In a double-logarithmic plot, Ohmic conduction shows a line with a slope of 1.[136] Ideally, this should not be present in dielectric materials, but due to processing, charged defects often occur leading to free charges. Thus, if the other conduction mechanisms are sufficiently suppressed, this mechanism is usually observed.[136]
- **Space-charge-limited conduction:** This mechanism can occur when charges are injected into the insulator at an Ohmic contact. These charges then form a space-charge similar to that of a vacuum diode. The conduction behaviour can then be described by Child's law, for which the current density is proportional to the square of the applied electric field. Hence, in a double-logarithmic plot, a linear behaviour with a slope of 2 is expected.[136]

- **Poole-Frenkel emission:** Poole-Frenkel emission is, similar to Schottky emission, based on the thermal excitation of charges. The concerning charges contributing to the current, however, are generated from internal traps for this mechanism.

The resulting current density conforms to the following expression:[136]

$$J = q\mu N_C E \cdot \exp\left(\frac{-q(\phi_T - \sqrt{qE/\pi\epsilon_0\epsilon_{Op}})}{k_B T}\right) \quad (3.11)$$

where μ is the electronic drift mobility, N_C is the density of states in the conduction band and $q\phi_T$ corresponds to the trap energy level.

For this mechanism, a linear relation is expected for the plot of $\log(J/E)$ versus \sqrt{E} and via its slope the optical permittivity can be extracted:

$$\epsilon_{Op} = \frac{q^3}{\pi\epsilon_0\epsilon_{Op}k_B^2 T^2 m^2} \quad (3.12)$$

Due to the necessity for thermal excitation, this mechanism is usually observed at higher temperatures and high fields.[137]

- **Hopping conduction:** Hopping conduction is another mechanism relying on the tunnelling of charges. In this case, the concerning charges are trapped charges which tunnel from one trap site to the next and, thus, are transported through the insulator via so-called 'hopping'. A necessary requirement is the presence of sufficient trap sites, as common hopping distances are usually below 2 nm. The current density can be expressed via:[136]

$$J = qan\nu \cdot \exp\left(\frac{qaE}{k_B T} - \frac{E_a}{k_B T}\right) \quad (3.13)$$

where a is the mean hopping distance, n the electron concentration in the conduction band of the insulator, ν the vibration frequency of the electrons at the trap sites and E_a the activation energy which corresponds to $q\phi_T$.

3.2.4 Measurement of the Polarisation

Direct measurement of the polarisation of FE and AFE materials has been shown to be very challenging and the absolute value of the polarisation cannot be accessed. Therefore, modern measurement techniques quantify changes in the polarisation.[1]

In terms of indirect measurement techniques, due to the coupling of polarisation to temperature via the pyroelectric effect and to deformation via the piezoelectric effect, the

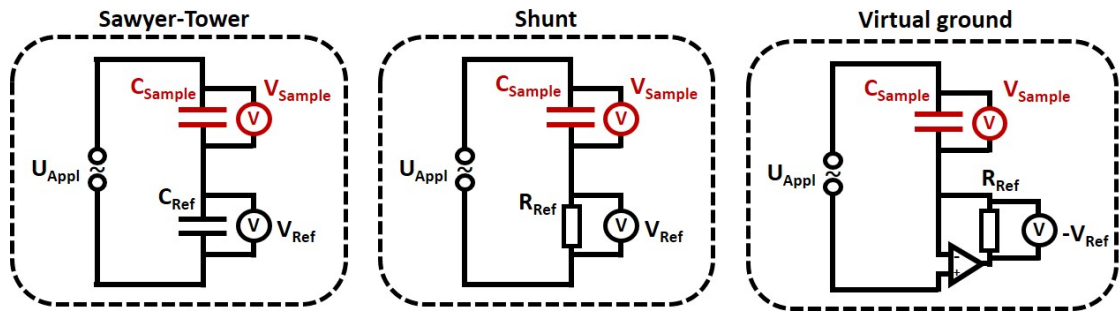


Figure 3.2.3: Equivalent circuits for the different polarisation measurement techniques.[140]

external stimulus can be manifold.[139] However, in this chapter, the most common excitation via electrical stimulus will be discussed.

The first method to measure the polarisation via application of a voltage was via a Sawyer-Tower circuit,[141] depicted in Figure 3.2.3. The sample capacitor is connected in series to a reference capacitor with a known capacitance. As the charge displacement is the same for both capacitors, the voltage across the reference capacitor is directly proportional to the polarisation charge.[140] Due to parasitic effects, the decreased precision of this setup is a disadvantage as well as problems for measurements with low frequencies.[139] To overcome the low precision of the Sawyer-Tower circuit, the shunt method is based on the measurement of the displacement current over a serial resistance, as the precision of the resistors is better than of capacitors.[139] The current is measured via the voltage drop over the resistance and integrated to access the polarisation charge.[139]

For both methods mentioned so far, the reference capacitor or resistance has to be selected appropriately to the sample capacitance. The virtual ground method overcomes this drawback by utilising an operational amplifier together with a feedback resistance.[139] This allows to measure even a small sample capacitance with high precision, which is the reason why this method is commonly used in commercial setups.[140]

The resulting polarisation behaviour is calculated from the measured current and often complicated to understand due to the presence of defects and leakage current interfering with the shape of the curve. In this regard, bloating of the polarisation curve due to leakage resembles a FE hysteresis and is often interpreted as such.[142] Thus, it is important to understand the different contributions to the polarisation versus electric field measurement.

Many origins can be untangled when the current versus electric field curve is regarded. Accordingly, several scenarios of polarisation curves along with their current versus electric

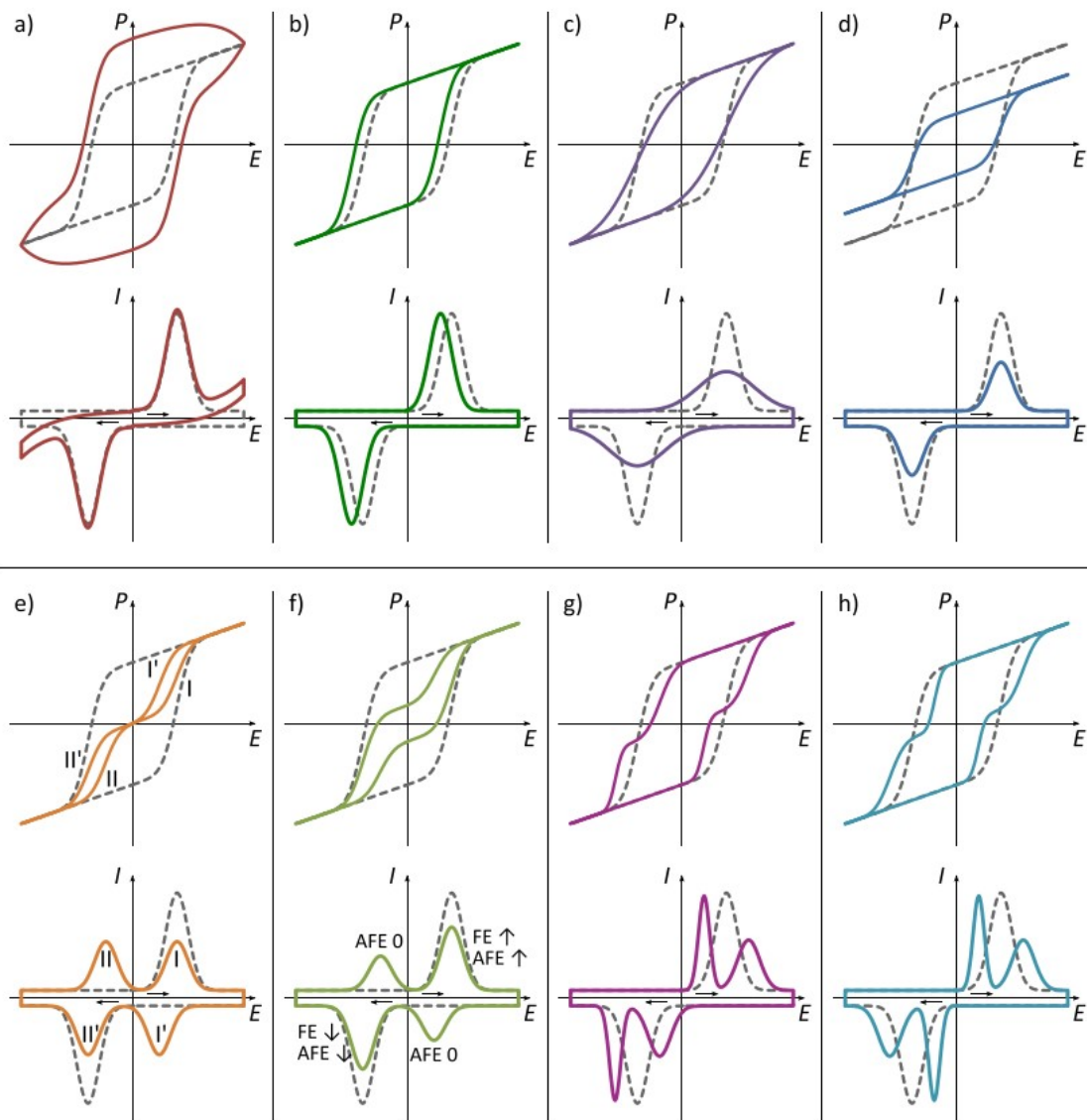


Figure 3.2.4: Polarisation versus electric field curves for different scenarios encountered in dielectrics, with the corresponding current versus electric field curve below. The dashed lines represent the behaviour for a FE material. Reprinted with permission.[140]

field curve are schematically depicted in Figure 3.2.4.

The P-E curve in *a*) shows a bloated shape, which is masking the true behaviour of the dielectric. While a FE material shows two peaks in the current curve, the contribution of leakage current can be unambiguously recognised by the current increase at larger electric fields.

Asymmetric coercive fields, shown in *b*), a so-called 'imprint', can be caused by a variety of effects. Often such a behaviour is observed when electrodes with different work functions are used.[140]

A broadening of the current peaks, as seen in *c*), leading to a slanted hysteresis is often observed due to the 'dead layer' effect, which originates in a linear dielectric layer in series with the FE layer, lowering the voltage drop over the FE.[140]

Fatigue is responsible for a number of changes in the P-E behaviour, most prominent the reduction of the remanent polarisation shown in *d*), as some domains get stuck and cannot contribute to the polarisation anymore.[140] Aging in FE has also been observed to lead to pinched loops as those shown in *e*). In this case, the back-switching originates from domain pinning on defects and, although a double hysteresis loop is observed, the material is FE and not AFE.[143] Repeated AC cycling can alleviate this pinning effect and transform the P-E behaviour to an FE hysteresis loop again.[140]

Another case resembling an AFE material is depicted in *f*). Here, two sublattices with opposite polarisation exist in the ground state, however, the magnitude of their polarisation is not equal and, hence, they do not cancel each other completely. The result is a ferrielectric material.[143] Pure AgNbO_3 is considered as a material of this class due to a small remanent polarisation.[16]

Domains with different internal bias fields, see *g*), or change in switching fields of different domains due to a local variation in defect concentration, see *h*), lead to two peaks in the current versus field (I-E) characteristic as well, however, the actual material is a pure FE.[140]

Concluding, much attention has to be paid to the interpretation of the various shapes of the P-E behaviour, taking into account the behaviour of the I-E curve as well. Ideally, in order to unambiguously identify a material as an AFE, additional measurements like structural characterisation should be conducted to solidify the true nature of the dielectric.

4 Experimental Procedures

4.1 Synthesis of Thin Films

For the growth of thin film samples, ceramic targets of the desired composition are necessary. These are fabricated via a solid state synthesis route, resulting in dense specimen which are confirmed to be phase-pure by XRD.

4.1.1 PLD

Experimental Setup

The film depositions are conducted with the DAISY-BAT (DARMstadt's Integrated SYstem for BATtery research) PLD, equipped with a KrF excimer laser (LPX-Pro 210 F, Coherent) with a wavelength of 248 nm. As depicted in the schematic illustration of the PLD system in Figure 4.1.1, this laser is guided through an attenuator for energy control and focused via several lenses and mirrors into the vacuum system. There, it impacts on the target, which is stored in a target carousel of six targets. Via rotation and sweep of the circular target, most of the surface can be accessed by the laser spot. Movement of this target carousel out of the laser path allows the laser to shoot through the chamber into the laser detector (EnergyMax Sensor, Coherent) positioned on the outside of the chamber, which is coupled to an energy meter (FieldMaxII, Coherent). Thus, the laser energy can be measured and calibrated accordingly via feedback to the applied laser voltage and attenuator position.

The substrate column is positioned parallel to the target with a variable distance. A shutter is installed in front of the substrate to avoid material deposition before the actual process begins. The back of the substrate holder is heated via a near-infrared laser diode (JOLD-x-CPXF-2PW, Jenoptik) with a wavelength of 988 nm and a maximum power of 140 W. Precise temperature control is enabled via feedback from a pyrometer (METIS MP 25, SensorTherm), which measures the temperature of the back side of the substrate holder via the emitted infrared radiation. This signal is adapted to the emissivity of the

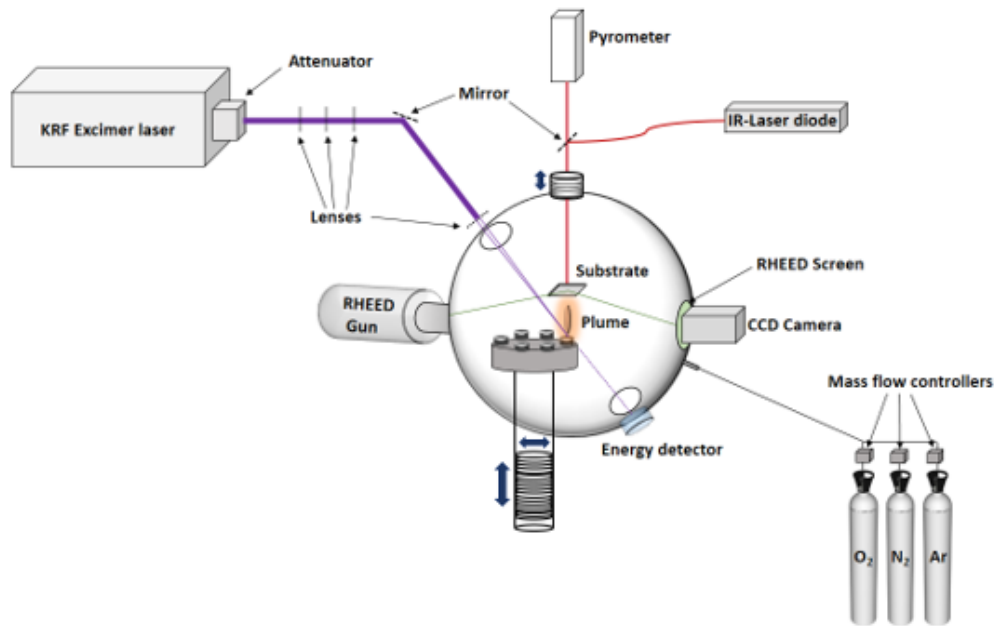


Figure 4.1.1: Illustration of the PLD device utilised in this thesis.

substrate holders which consist of oxidised inconell steel.

The pressure can be monitored by a range of pressure gauges for different pressure ranges including capacitance monometers and an ion gauge, such that the precise pressure can be determined from high vacuum until atmospheric pressure. The atmosphere inside the PLD chamber can be controlled by a mass flow controller (PR4000b, MKS) connected to oxygen, nitrogen and argon gas bottles with a purity of 99.998 %. Additionally, the connection to the turbo molecular pump of the main chamber is equipped with an incremental gate valve, which can be closed partially to limit the pumping power and increase the pressure.

4.1.2 Process

The substrate holders are polished with sandpaper before each deposition and cleaned with acetone in an ultrasonic bath. The substrates are glued to the cleaned substrate holders with silver glue and baked for approximately 15 min at 120 °C on a hot plate to evaporate solvent residues of the glue. The targets are also polished with sandpaper and freed from powder particles with nitrogen. Immediately before injection, targets and

substrates are blown off with nitrogen to avoid flying impurities. Before deposition, the laser energy is measured and adjusted via adaption of the attenuator and the voltage applied to the laser. Small corrections are performed via adjustment of the laser spot size, which can be precisely controlled via a motorised lens. The corresponding spot size is initially set to 1.8 mm^2 and varied by a maximum of 0.5 %, which is considered negligible for the the process. The targets are then moved into the laser beam and the position of the laser is centred by moving the target. The maximum deflection of the targets is programmed into the system so that the largest possible area of the target surface is scanned during deposition by translation and rotation of the target. After programming the target movement, the surface of the target is cleaned by laser pulses with the substrate shutter closed. For this cleaning of the target surface, 1000 laser pulses are used. For growth of heterostructures, this process is conducted for all targets used in the deposition process. After cleaning the target surface, the substrate is transferred into the chamber and the atmosphere for the first ablation process is introduced into the chamber. For all growth processes, pure oxygen atmosphere is applied. Then, the substrate holder is heated with the diode laser from the back side. The heating rate is set to $50 \text{ K} \cdot \text{min}^{-1}$. Once the substrate reaches the deposition temperature, the ablation is started. If heterostructures are grown, once the programmed amount of laser shots for the first deposition is reached, the pressure and substrate temperature are adapted for the next growth process. Meanwhile, the other target is selected from the target carousel and the height adjusted such that the laser spot impacts on its centre. Finally, after the substrate-to-target distance is adjusted, the next deposition is started. After all depositions are completed, the sample is cooled down to room temperature with $30 \text{ K} \cdot \text{min}^{-1}$. Then, the atmosphere is removed, returning the system to the original state. Once the substrate is removed from the vacuum system, it is detached mechanically from the substrate holder and is ready for analysis via XRD or XPS or further processing via photolithography. In the process of this thesis, many parameters of the PLD process are optimised to achieve phase pure thin films and further improve the film quality. These are described in the corresponding sections concerned with the optimisation of the film growth of NaNbO_3 and AgNbO_3 . The parameters which are discussed during the optimisation are the laser fluence Φ , the substrate temperature T_S , the oxygen pressure P_{O_2} , the substrate target distance d_{S-T} and the frequency f . The number of laser shots is constant for all optimisation processes with 2000 laser pulses and is later adapted to adjust the film thickness as desired. The electrode material LaNiO_3 is similarly optimised in the scope of this thesis, concluding with the parameters in Table 4.1.1. The thin film is optimised in regards to phase purity, strain state and resistivity. The final parameters result in single-crystalline films, which

Table 4.1.1: PLD parameters for the growth of LaNiO₃ thin films. Given are the laser fluence Φ , the substrate temperature T_S , the oxygen pressure P_{O_2} , the substrate target distance d_{S-T} , the frequency f and the number of laser shots.

Φ (J/cm ²)	T_S (°C)	P_{O_2} (mbar)	d_{S-T} (mm)	f (Hz)	Laser Shots
1.25	650	0.04	35	2	2000

are shown to grow fully strained on all utilised substrates in this thesis. The resistivity is measured by a four-bar structure sputtered with gold via a shadow mask and amounted to 250 $\mu\Omega$ cm for growth on SrTiO₃, which is sufficient for application as a bottom electrode. While the resistivity of LaNiO₃ can reach values below 100 $\mu\Omega$ cm, it strongly depends on the cation stoichiometry and strain state.[79] The thickness of this layer is kept constant for all heterostructures, and the 2000 laser pulses result in 25 nm.

The substrates which are utilised in this thesis are single crystals supplied by Crystec. The employed substrates are: (LaAlO₃)_{0.3}(Sr₂TaAlO₆)_{0.7}(100) (LSAT), SrTiO₃(100), DyScO₃(110) and GdScO₃(110). Optimisation studies are carried out on the substrate with the lowest mismatch, which corresponds to SrTiO₃ for NaNbO₃ and DyScO₃ for AgNbO₃.

4.1.3 Photolithography Process

The processing for the photolithography is done in the in-house cleanroom. First, a negative resist (ma-N 1420, Microresist) is applied via spin-coating. This step is conducted with 6000 rpm for 34 s, resulting in a thickness of ~ 1.4 μ m. Next, the resist is subjected to a baking process on a heating plate at 105 °C for 2 min. This step reduces the solvent in the resist. During the spin-coating process, the centripetal force causes the photoresist to accumulate at the edges and corners, forming an edge bead. This bead can cause issues during exposure in the mask aligner. To address this, the edge bead is removed carefully from the corners using a thin razor blade.

The photoresist is then structured using a mask aligner (MJB4, Süss MicroTec). This device is equipped with a microscope and is used to precisely align a glass mask over the substrate and bring them into contact. A mercury lamp emitting g-line ($\lambda = 436$ nm), h-line ($\lambda = 405$ nm), and i-line ($\lambda = 365$ nm) UV light is used to expose the sample. The exposure time is adjusted for each exposure by an initial energy check to result in a dose of 0.81 mW \cdot cm⁻² \cdot s. In the case of a negative resist, this UV exposure leads to hardening

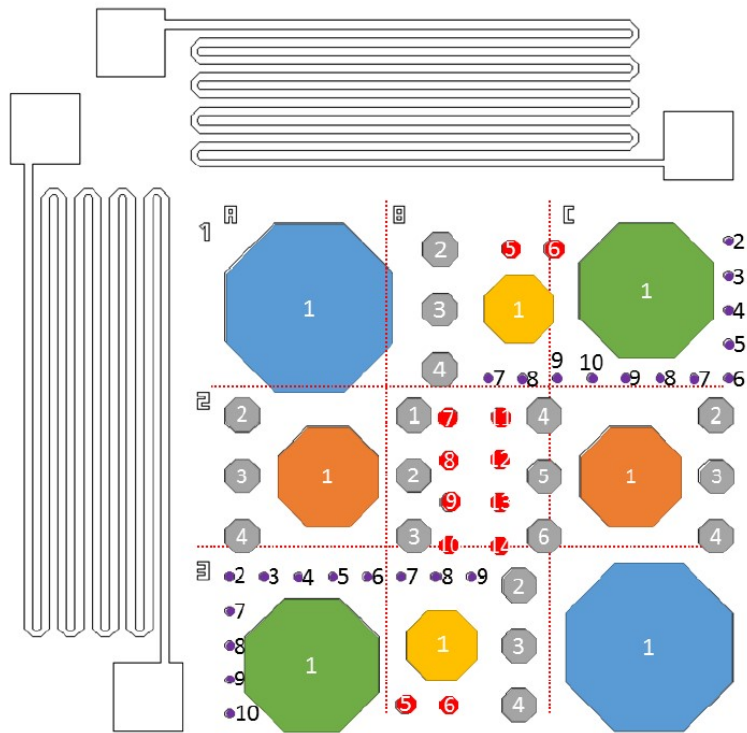


Figure 4.1.2: Layout of the photolithography mask utilised in this thesis. The size of the pattern corresponds to the substrate size of 5x5 mm. The electrode areas range from 0.0019 mm² to 0.7842 mm².

of the resist. Thus, the area where the electrodes are desired, is covered by the mask, shown in Figure 4.1.2. This mask features octagonal electrodes with various sizes to study the impact of electrode size on the dielectric properties.

After exposure, the sample is immersed in the appropriate developer (ma-D-533s, Microresist) for 70 s, which removes the unexposed parts of the resist, leaving only the hardened areas intact. After these 70 s, the samples are removed from the developer and rinsed in deionised water and dried with nitrogen gas. Following a final quality control inspection using an optical microscope (Axio Lab.A1, Carl Zeiss), the surface is cleaned using O₂ plasma etching (Femto, Diener electronic) for 1 min at 70 W, to facilitate good interface formation of the contacts.

For the contacts, first a thin layer of Pt is sputtered for good adhesion and then Au is sputtered on top. Both materials are sputtered with a DC magnetron sputter coater (Q300T, Quorum Technologies). Pt is sputtered with 30 mA for 100 s, while Au is sputtered with 50 mA for 250 s. Both processes are conducted in an Ar atmosphere of 1 Pa. The sputter rate for both materials is calibrated with a profilometer (Dektak XT, Bruker), and the given conditions resulted in 100 nm of Pt and 500 nm of Au.

Finally, the samples are immersed in acetone, removing the remaining photoresist and leaving only the desired pattern behind. The samples are then dried with nitrogen gas. To access the bottom electrode for the electrical measurements, part of the film is mechanically removed in one corner and a connection between one sputtered electrode and the bottom electrode is fabricated via silver paste.

4.2 Sample Analysis

After synthesis, all samples are characterised by XRD and XRR. Depending on the sample, further characterisation in regards to the strain state via RSMs or their stoichiometry via XPS is conducted. Once film growth optimisation is concluded and the bottom electrode is integrated into the growth process, further electrical characterisation is added after contact fabrication via photolithography.

4.2.1 XRD

Experimental Setup

A X-ray diffractometer (SmartLab, Rigaku) equipped with Cu-K α radiation and a parallel beam geometry is used for all relevant measurements. In this geometry, the generated X-rays are parallelised by means of a parabolic multi-layer mirror and directed onto the sample. While the beam remains divergent in-plane, a manual slit system is employed to

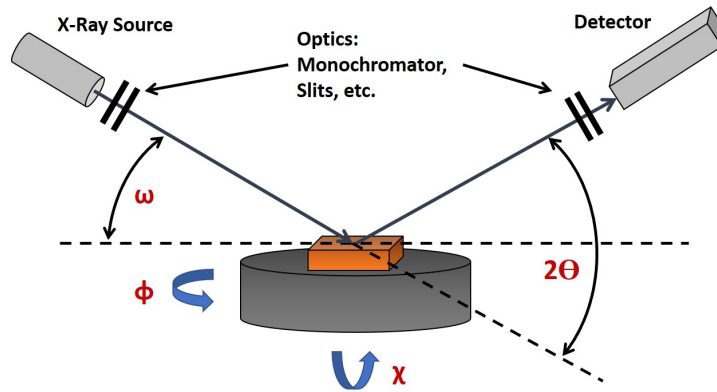


Figure 4.2.1: Simplified sketch of a four circle diffractometer.

control the height limitation. For most measurements, a germanium 2-bounce monochromator is used. Inside the monochromator, two germanium crystals are oriented in (220) orientation and cut at a 22.6° angle relative to the beam direction. This setup allows for a measurement resolution below 20 arc seconds.

The specimen is placed onto a sample stage which can be moved in all three dimensions. Further, it can be rotated by the angle ϕ and tilted about an axis in the measuring plane by the angle χ . The angle of incidence of the X-rays is designated as ω . The sum of the angle of incidence and exit angle is called diffraction angle 2θ , which defines the diffraction planes. A schematic diagram for X-ray diffraction of thin films is shown in Figure 4.2.1.

Process

Before each measurement, the sample is aligned via a direct beam half-cut alignment for small differences in height and tilt upon which the XRR is conducted. Then a surface normal alignment to the most intense substrate reflection is employed to account for the miscut angle. Then all perpendicular reflections are recorded via a $\theta - 2\theta$ scan from 10° to 110° which measures all $(00l)$ reflections of the utilised materials up to the fourth order. For the analysis of characteristic values from the XRR measurements, model structures are simulated and fitted to the measured curves (RCRefSiW, IHP Solutions). The extracted parameters include film thickness, density and surface and interface roughness. The RSM measurements are conducted on the 103 substrate reflection for all cases,

featuring an in-plane component to extract the strain state of the films. For the case of the orthorhombic substrates, the pseudo-cubic notation is utilised. To get the full relation for all directions, RSM measurements are repeated with rotation of ϕ by 90° , leading to the measurement of the 013, -103 and 0-13 substrate reflections. The resulting data is converted into reciprocal coordinates (3D Explore, Rigaku) for further analysis.

4.2.2 XPS

Experimental Setup

The X-ray photoelectron spectroscopy (XPS) measurements are conducted using the DAISY-BAT XPS system. The employed spectrometer (Versaprobe 5000, PHI) allows for angle-dependent XPS measurements. The system is connected to the DAISY-BAT PLD setup via a distribution chamber, enabling convenient in-situ sample transfer between the PLD and XPS systems.

In the experiments, a monochromatic Al-K α radiation source with a photon energy $h\nu$ of 1486.6 eV is utilised. The measurements are carried out at room temperature under an ultra-high vacuum condition of 5×10^{-9} mbar. Unless otherwise specified, the detector is positioned at an elevation angle of 75° with respect to the substrate, resulting in an information depth of approximately 5 nm to 8 nm. For XPS measurements on the dielectric materials, a dual-beam neutraliser is used due to the very low electrical conductivity. Irradiation with electrons and argon ions compensate for the charging effects. However, an exact determination of the absolute binding energy E_b is only possible by comparison with reference measurements.

Process

XPS measurements are conducted for the optimisation series with the goal of stoichiometric thin films, as well as regular checks of the stoichiometry for the films after the optimisation is concluded. These checks reveal only small variations and show a conservation of the stoichiometric relation with the utilised parameters.

For all measurements, a survey spectrum and detailed spectra of the relevant elements are taken. The survey spectrum is measured with a pass energy of 187.5 eV and a resolution of 0.8 eV while for the detailed spectra a pass energy of 23.5 eV and a resolution of 0.1 eV are employed.

The resulting survey spectra are investigated in regards to the presence of impurity elements. The detailed spectra are analysed in terms of intensity for their relative con-

centration and peak distribution for the presence of different oxidation states. This is done via fitting of simulation curves (Casa XPS, Casa Software Ltd), after subtraction of a Shirley-based background.[144] Then, a Voigt profile with a 30 % Lorenz character is fitted to the relevant peaks, and the intensity is integrated.

4.2.3 Leakage Current Measurement

The leakage current of the samples is measured with a semiconductor characterisation system (4200-SCS, Keithley Instruments). The sample is connected on a probe station (TTPX, Lake Shore Cryotronics) via beryllium-copper tips with a diameter of 25 μm . A DC voltage is applied to the top electrode while the bottom electrode is grounded. For each measurement, alternating positive and negative voltages are applied with increasing magnitude. This is conducted until the compliance current of 0.1 A is reached or a saturation of the current versus voltage behaviour is observed.

4.2.4 Polarisation Measurement

The P-E behaviour of the samples is measured with a custom built probe station. It is enclosed within a lidded structure made of film-faced plywood to minimise external mechanical noise. The exterior of the enclosure is covered with metallic plates and electrically grounded to ensure proper insulation of the measurement setup. This common electrical ground is shared by the probe tips positioners and, when necessary, the sample itself. The probe station is equipped with micropositioners (S-725, Signatone), onto which tungsten tips with a diameter of 25 μm are mounted.

The polarisation behaviour is recorded using a P-E loop tracer (TF Analyzer 2000, aixACCT Systems), equipped with a FE module. This setup employs the 'virtual ground' method, allowing precise measurements also for small sample capacitance.[140] The samples are electrically contacted using the custom-built probe station. As the exact electrode area is necessary for the calculation of the polarisation and current density, the top electrode is kept grounded and the sample is driven by the bottom electrode. Thus, field spreading is minimised and the area of the top electrode can be used for calculation of the current densities, which is known exactly due to the photolithography process.

To measure the P-E loops, dynamic hysteresis measurements are conducted by applying a triangular waveform with a frequency of 100 Hz to 1000 Hz. The frequency determines the time required for the sample to complete a full P-E loop, affecting the relaxation time between each data point.[139] Therefore, a higher frequency can lead to successful measurements on samples with higher leakage current, as part of this current is suppressed. Prior to the hysteresis measurements, a pre-polarisation pulse loop is applied to establish

the initial, defined polarisation state. This state is consecutively treated as the negative remanent polarisation.

It is important to note that P-E loops are influenced by the sample's electrical and mechanical history, as well as the measurement method employed. Thus, if multiple electrical characterisation techniques are employed for a sample within this thesis, it is only compared to other samples with the identical electrical history.

5 Towards High Quality Thin Films

5.1 Motivation

This chapter is concerned with the optimisation of the growth of NaNbO_3 and AgNbO_3 thin films via PLD. The growth optimisation is conducted with only few literature describing the PLD growth of NaNbO_3 [145, 102, 29, 97, 146, 98, 147, 105] or AgNbO_3 thin films.[110, 112, 30] Even among these few publications, most focus on the growth of films with thicknesses above $1\ \mu\text{m}$, which are not single-crystalline and, hence, not optimised towards high quality thin films. Further, among these publications, the parameters which are utilised for the film deposition vary greatly. Thus, despite the high interest in these materials and the AFE effect, the literature remains surprisingly scarce, indicating the difficulty of thin film growth of these materials.

The goal of this chapter is, therefore, to get a conclusive picture about the critical points of the film growth for NaNbO_3 and AgNbO_3 and how to overcome these problems:

1. **What is the central difficulty for growth of NaNbO_3 and AgNbO_3 thin films?**
2. **How can this difficulty be overcome to achieve growth of epitaxial thin films?**
3. **How do the growth parameters translate to other substrates to achieve different strain states for NaNbO_3 and AgNbO_3 ?**

5.2 NaNbO_3

5.2.1 Achieving Phase Pure Films via Growth Parameter Optimisation

Initial parameters for growth of NaNbO_3 films are adapted from literature, however, a wide variation for the few literature of PLD grown NaNbO_3 thin films is found, see Table 5.2.1. Further, most of these feature thick films with polycrystalline (PC) structures and, thus, are not optimised for coherent layer-by-layer growth. The starting parameters are taken based on one of the references with single crystalline structure[98] and adjusted from there. Initial growth is optimised on $\text{SrTiO}_3(100)$ substrates which show the smallest

Table 5.2.1: PLD parameters for the growth of NaNbO_3 thin films from literature. Given are the laser fluence Φ , the substrate temperature T_S , the oxygen pressure P_{O_2} , the substrate target distance d_{S-T} , the frequency f , the thickness t , crystallinity C , either polycrystalline (PC) or single-crystalline (SC) and the corresponding reference.

Φ (J/cm^2)	T_S ($^\circ\text{C}$)	P_{O_2} (mbar)	d_{S-T} (mm)	f (Hz)	t (nm)	C	Reference
2-3	1123	-	-	10	160/240	PC	[145]
0.5	850	0.013	40	-	100	SC	[97]
0.9	750	0.27	90	10	3100	PC	[146]
0.9	850	0.27	90	10	2800	PC	[29]
2.2	600/900	0.05-2	54	5	15	SC	[98]
0.9	850	0.3	90	10	4500	PC	[102]
-	700	0.1	-	-	250	-	[105]

mismatch to NaNbO_3 , see Table 5.2.3.

Growth experiments with the chosen parameters are unable to achieve the NaNbO_3 phase even with substantial variations to the temperature, the fluence or the pressure. The origin for this poor film quality is traced to a significant off-stoichiometry of the cations. In all these initial growth attempts, a severe deficiency of Na can be detected. This deficiency is commonly observed for bulk NaNbO_3 ceramics as well, which suffer from the volatility of Na at elevated temperatures.[148] This can be compensated by an over-stoichiometric addition of Na in the starting materials.[149, 148] For growth of thin films, on the other hand, a relation between the background pressure and the cation stoichiometry is found, which is ascribed to a counteracting effect of the higher pressure on the volatility of Na_2O , effectively decreasing the amount of sodium and oxygen vacancies in the film.[98] Therefore, the background pressure during the process is increased significantly, and the phase formation and cation stoichiometry of the NaNbO_3 thin films is investigated, while all other parameters are kept constant. The resulting $\theta - 2\theta$ -scans and cation stoichiometry of the thin films are shown in Figure 5.2.1.

Both from the structural analysis and the film stoichiometry, a large impact of the pressure variation is apparent. While for low and high oxygen pressures, multiple peaks due to the film growth are recognisable in Figure 5.2.1a, for pressures of 0.53 mbar and 0.6 mbar, a single phase is achieved. Further, the two films grown under these pressures show Laue oscillations, which are indicative of high film quality. These results coincide with the

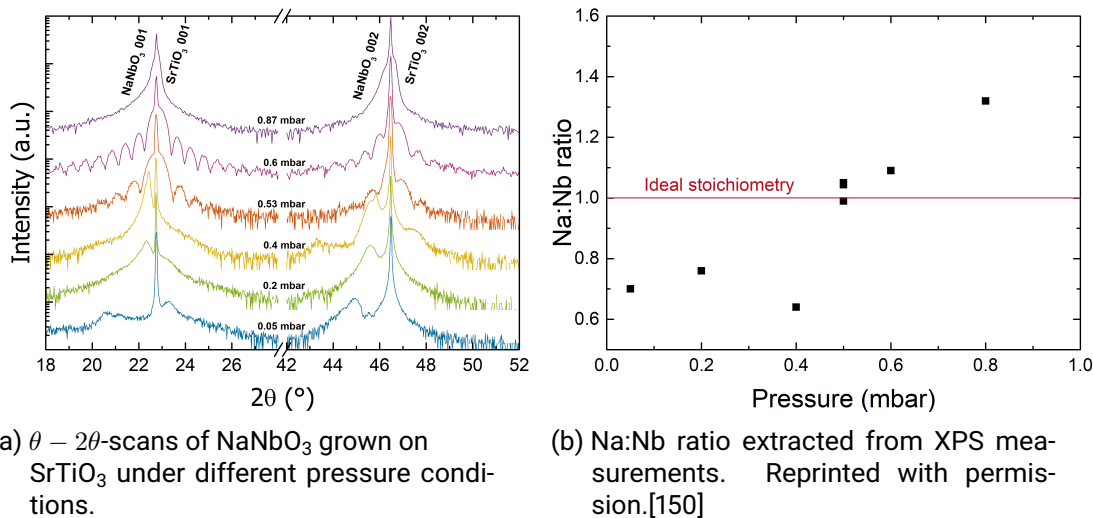


Figure 5.2.1: Impact of pressure variation on the film growth of NaNbO_3 thin films. Displayed are the 001 and 002 reflections of the $\theta - 2\theta$ -scans in a) and the cation ratio of these films in b).

cation ratios extracted from XPS measurements, shown in Figure 5.2.1b. An increase of the sodium to niobium ratio with pressure is visible, and thin films with ideal stoichiometry can be found close to a background pressure of 0.53 mbar. In Figure 5.2.1b additional points at this pressure confirm the reproducibility. These results clearly correlate the phase formation with the cation stoichiometry, emphasising the delicate balance between the pressure and film stoichiometry for NaNbO_3 thin films. The final parameters, which are obtained after optimisation of the other parameters for a pressure of 0.53 mbar to further improve the film quality are given in Table 5.2.2. These parameters result in single-phase NaNbO_3 thin films with extensive Laue oscillations and a stoichiometric cation ratio. The growth rate varies, depending on the film thickness, by a few percent and corresponds to $\sim 100 \text{ pulses} \cdot \text{nm}^{-1}$ for films grown with 2000 laser pulses on $\text{SrTiO}_3(100)$ substrates.

5.2.2 Heterostructures

For a thorough investigation into the dielectric properties of the thin films, fabrication of a capacitor structure is necessary. This can be arranged via a parallel plate capacitor structure or via interdigital electrodes. The first requires a bottom electrode below the dielectric film and electrodes with a defined area on top, while the latter only necessitates

Table 5.2.2: Optimised PLD parameters for the growth of NaNbO_3 thin films. Given are the laser fluence Φ , the substrate temperature T_S , the oxygen pressure P_{O_2} , the substrate target distance $d_{\text{S-T}}$, and the frequency f .

Φ (J/cm^2)	T_S ($^\circ\text{C}$)	P_{O_2} (mbar)	$d_{\text{S-T}}$ (mm)	f (Hz)
1	750	0.53	40	10

deposition of patterned electrodes on top of the film. The latter accesses the in-plane properties of the films, however, entails a complex analysis as the simulation of the field distribution is necessary and the substrate contributes to the measured behaviour as well. On the other hand, a parallel plate capacitor features a homogeneous electric field and the measurement directly provides the properties of the dielectric. Thus, this method is selected for the analysis of the films grown in this thesis.

The bottom electrode is required to feature a similar crystal structure, enabling epitaxial growth of this material, and, consequently, transfer of the epitaxial relation from the substrate to the dielectric thin film. Further, high conductivity is necessary such that the electrode can be grown sufficiently thin, resulting in no relaxation even at larger lattice mismatch to the substrate. LaNiO_3 fulfils these requirements sufficiently.[79, 151]

Therefore, the growth of LaNiO_3 is optimised with regards to its crystalline quality and conductivity. Special attention is paid to the cation stoichiometry for this material as well, as the control of the Ni content is essential to low resistivities.[79, 152] The optimised parameters are shown in Table 4.1.1, resulting in LaNiO_3 thin films with a resistivity of $250 \mu\Omega \text{ cm}$ for growth on $\text{SrTiO}_3(100)$, as characterised with a four-bar structure. Then, the growth of the previously optimised NaNbO_3 thin films is translated onto the stack structure consisting of $\text{LaNiO}_3/\text{substrate}$, as differences in the growth can arise due to a change in the involved surface energies.

However, no significant impact on the growth of NaNbO_3 and its crystalline quality can be detected with the change to the stack structures. The corresponding structural analysis is shown in Figure 5.2.2.

The $\theta - 2\theta$ -scan reveals single phase thin films with high quality for both the NaNbO_3 as well as the LaNiO_3 , as indicated by the presence of two sets of Laue oscillations, see Figure 5.2.2a. A RSM is recorded to investigate the strain state of both thin films, see Figure 5.2.2b. This RSM reveals the same Q_x for all involved materials, thus, the in-plane lattice parameter of the substrate coincides with those for LaNiO_3 and NaNbO_3 , confirming the strained growth. It should be noted, that for NaNbO_3 the reflection in the RSM is

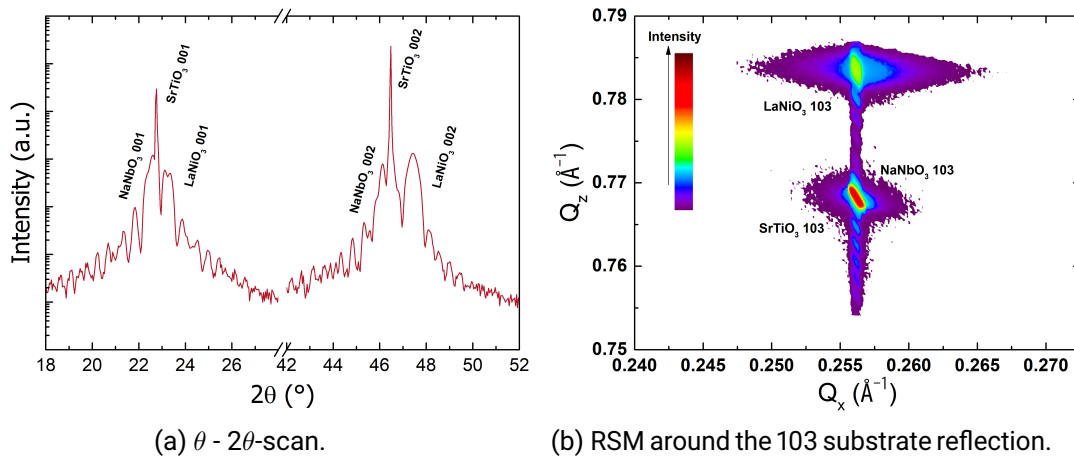


Figure 5.2.2: XRD analysis of a NaNbO_3 thin film grown on the stack structure of $\text{LaNiO}_3/\text{SrTiO}_3(100)$.

hidden behind that of SrTiO_3 due to the small difference in their lattice parameters. Thus, the previously optimised parameters are also applicable for growth with the addition of the LaNiO_3 bottom electrode and the strain can be transferred through the bottom electrode into the dielectric layer for growth on $\text{SrTiO}_3(100)$.

5.2.3 Translation of the Growth to other Substrates

To quantify the impact of strain on the AFE properties, thin films of NaNbO_3 have to be optimised on a variety of substrates to induce different amounts of strain. Appropriate substrates are chosen such that an evolution of the properties from films under compressive to tensile strain can be observed. The lattice parameters from NaNbO_3 , the relevant substrates, as well as for LaNiO_3 , which serves as a bottom electrode for electrical characterisation, are given in Table 5.2.3. For NaNbO_3 , the substrates conforming to this criterion are LSAT for compressive strain, SrTiO_3 for compressive or tensile strain with a low magnitude and DyScO_3 and GdScO_3 for tensile strain of different magnitudes. The strain of NaNbO_3 for the different combinations are included in Table 5.2.3 as well.

For growth on the different substrates, the deposition parameters which have previously been optimised for growth on $\text{LaNiO}_3/\text{SrTiO}_3$ are chosen. XRD and XPS measurements reveal good applicability of these parameters, leading to high quality, stoichiometric thin films on the other substrates as well. The shift of the NaNbO_3 reflections in $\theta - 2\theta$ scans, see Figure 5.2.3, indicates incorporation of the strain. While the largest angle of the

Table 5.2.3: Lattice parameters of NaNbO_3 , [43] LaNiO_3 [79] and the substrates investigated in this section. For non-cubic perovskites, the corresponding pseudo-cubic lattice parameters are calculated. [31] The induced strain for epitaxial growth of NaNbO_3 is given in the last column. For this calculation it is assumed that the orientations align such that the lowest mismatch is achieved and the LaNiO_3 layer is considered to be fully strained. Note that, in the case of $\text{NaNbO}_3/\text{SrTiO}_3$, the strain calculation depends on the growth orientation, leading to either tensile or compressive strain.

Material	a (Å)	b (Å)	c (Å)	Strain in NaNbO_3 (%)
NaNbO_3	3.881	3.915	3.915	
LaNiO_3	3.84	3.84	3.84	
LSAT	3.868	3.868	3.868	0.77
SrTiO_3	3.905	3.905	3.905	0.26/-0.18
DyScO_3	3.945	3.943	3.943	-0.72
GdScO_3	3.965	3.961	3.961	-1.17

reflection, and, hence, the lowest out-of-plane lattice parameter is detected for growth on GdScO_3 , the reflection shifts gradually to lower angles for growth on DyScO_3 , SrTiO_3 and finally LSAT. This effect originates from the Poisson effect: For growth on GdScO_3 with the largest tensile strain, the out-of-plane lattice parameter is reduced to compensate this strain while for growth with compressive strain on LSAT, the Poisson effect results in an elongation of the out-of-plane lattice parameter. The same effect is visible for the LaNiO_3 reflection. Comparison of the position of the reflection with literature values of similar thickness [23] shows coinciding lattice parameters for a given substrate, indicating further that the addition of the LaNiO_3 bottom electrode does not affect the growth of NaNbO_3 in a detrimental way.

5.3 AgNbO_3

5.3.1 Achieving Phase Pure Films via Growth Parameter Optimisation

Similarly to NaNbO_3 thin films, initial growth parameters are adapted from literature, see Table 5.3.1. [30] However, again, the correct phase is not achieved by adaption of these parameters. From literature on bulk ceramics of AgNbO_3 , problems with the synthesis of

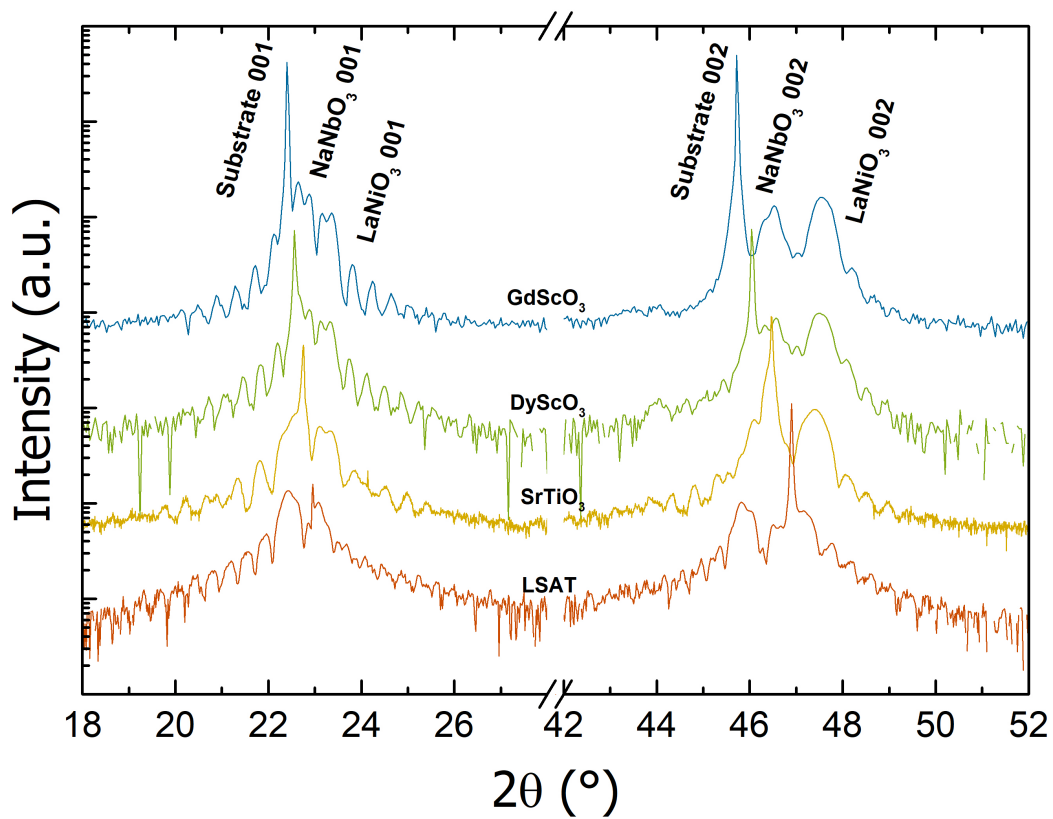


Figure 5.2.3: $\theta - 2\theta$ scans of NaNbO₃ thin films grown on different substrates. The areas around the 001 and 002 substrate reflections are magnified to visualise the Laue oscillations on the former and the peak shift of the NaNbO₃ due to the strain incorporation for the latter.

Table 5.3.1: PLD parameters for the growth of AgNbO₃ thin films from literature. Given are the laser fluence Φ , the substrate temperature T_S , the oxygen pressure P_{O_2} , the substrate target distance d_{S-T} , the frequency f , the thickness t , crystallinity C , either polycrystalline (PC) or single-crystalline (SC) and the corresponding reference.

Φ (J/cm ²)	T_S (°C)	P_{O_2} (mbar)	d_{S-T} (mm)	f (Hz)	t (nm)	C	Reference
0.5	750	0.13	40	-	50-150	SC	[30]
0.9	700	-	90	10	2100-3000	PC	[110]
-	550	500	70	-	200	SC	[112]

this material is found to be due to Ag.[153, 109] The silver shows difficulty integrating into the structure and features a high volatility at elevated temperatures, leading to deficiency in thin films as well.[154] Thus, the focus during the film optimisation is the cation stoichiometry and parameters which potentially influence this stoichiometry (see Section 3.1.1) are scanned. Primary focus is set on the pressure, which has been shown to be the critical parameter for the stoichiometry of NaNbO₃ thin films with its potential to prevent desorption. Secondly, the temperature is considered, due to the increased volatility of Ag at high temperatures. The film optimisation is conducted on DyScO₃(110) substrates, which show the closest lattice match to AgNbO₃, see Table 5.3.3.

However, no matter the parameter variation, Ag deficiency and correspondingly no AgNbO₃ phase is detected for any of the synthesised thin films, see Figure 5.3.1. These parameter sweeps included pressure variations from 0.13 mbar to 1.07 mbar, temperatures from 400 °C to 800 °C, laser fluences from 0.3 J · cm⁻² to 3 J · cm⁻², frequencies from 4 Hz to 10 Hz and variations of the substrate-to-target distance from 29 mm to 40 mm, see Figure 5.3.2.

The variation of the pressure has been shown in the optimisation of the growth of NaNbO₃ thin films to impact the desorption behaviour. Viewing the results of AgNbO₃ thin films grown under different pressures, a similar trend is discernible, see Figure 5.3.2a. However, it reaches a plateau at 0.53 mbar, at which the thin films are still far away from the desired stoichiometric ratio. Thus, desorption appears to contribute to the off-stoichiometry if the pressure is neglected, but another, more significant path of silver loss remains. Another parameter which is considered likely to cause silver loss due to its high volatility is the temperature during the process, see Figure 5.3.2b. With this in mind, a decrease of the silver content with increasing temperatures is expected. The reality as given by the XPS

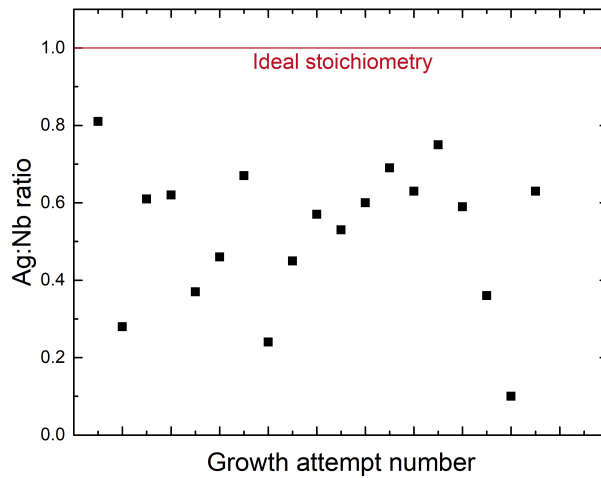
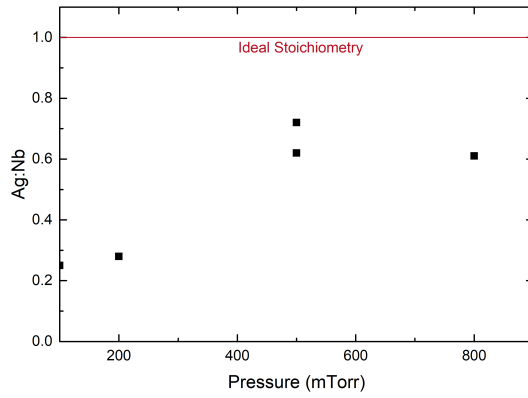


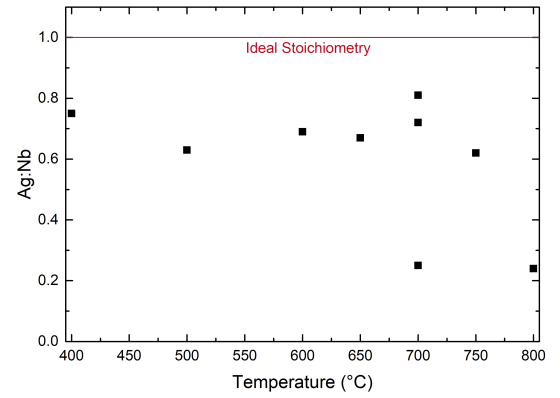
Figure 5.3.1: Cation stoichiometry of AgNbO_3 thin films grown via PLD with variation of process parameters. Each data point represents a sample, synthesised under different conditions.[155]

analysis, on the other hand, reveals the contribution of the temperature only at values above 700°C . Below, the stoichiometry does not depend on the chosen temperature. Further, this allows to exclude loss during the cooling down, as cooling times are decreased greatly for the processes with lower temperatures, which indicate no further change of the stoichiometry. Thus, the problems with the stoichiometric transfer may be found due to a non-stoichiometric ablation of the target, or processes in the gas phase. For the former, the laser fluence should influence the ablation behaviour, while the latter is impacted by the change of pressure as well as the distance the atoms need to overcome in the gas phase. In both cases, Figure 5.3.2c and Figure 5.3.2d, respectively, however, no trend can be discerned which encourages the respective assumption. For the variation of the laser fluence, only at a very low fluence of $0.3 \text{ J} \cdot \text{cm}^{(-2)}$ a decrease of the silver content is recognisable. This corresponds to the fluence threshold necessary for the ablation of the silver species.

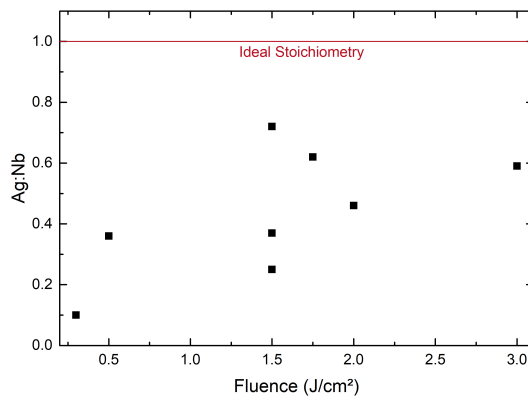
While these results show the difficulty of the stoichiometric transfer from the AgNbO_3 target into the film, they are no proof that this obstacle cannot be overcome by an appropriate choice of parameters. As the many different parameters are heavily influencing each other, the optimisation space is a multi-dimensional space and correspondingly a near limitless number of parameter combinations are possible. Meanwhile, compensation



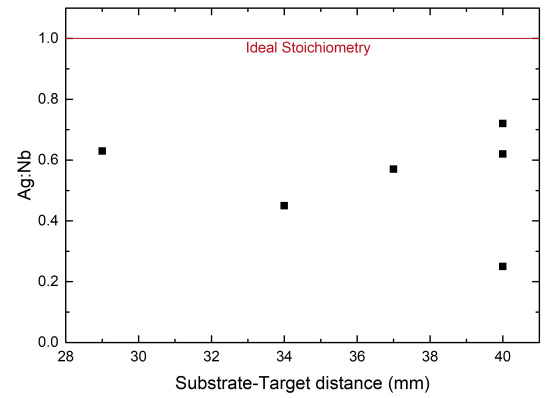
(a) Dependence on oxygen pressure.



(b) Dependence on substrate temperature.



(c) Dependence on laser fluence.



(d) Dependence on the target to substrate distance.

Figure 5.3.2: Cation stoichiometry of thin films grown from a stoichiometric AgNbO_3 target in dependence on various PLD parameters.[155]

of the off-stoichiometry via an external approach promises to significantly reduce the required effort. Further, the required parameter combination for a stoichiometric thin film could limit the control over the film growth and quality, making an external approach more attractive.

5.3.2 Ag Compensation Method

An external approach corresponds to a compensation of the Ag deficiency by a method not directly related to the PLD process. A common external approach to compensate off-stoichiometric transfer in the PLD process is the additional supply of the deficient element in the target. This can be accomplished via rotating segmented targets, with part stoichiometric material and part pure supply of the volatile element, [156] or fabrication of an off-stoichiometric target with excess of the volatile compound. [98] Both approaches are disadvantageous due to the large deficiency of Ag in the films. This leads to complicated processing or low target density for addition of a large amount of excess Ag, as AgNbO_3 has shown significant troubles when preparing bulk ceramics. [28] Low densities or segregation which are likely to occur would then be detrimental to the PLD process. [124] Instead, a novel approach is designed which is based on the high mobility of Ag ions at elevated temperatures: [157] Before the film deposition from a stoichiometric target, a thin layer of pure silver is sputtered on the substrate. During the subsequent PLD process, the silver from this layer can diffuse through the growing film and supply the necessary amount for AgNbO_3 phase formation by filling the vacancies which are created during the film growth process. This is enabled by the elevated temperatures during the PLD process. A schematic of this process is given in Figure 5.3.3.

To validate the feasibility of this approach, a series of thin films are grown from a stoichiometric AgNbO_3 target on $\text{DyScO}_3(110)$ substrates covered with Ag compensation layers of different thicknesses. For the approximation of the necessary thickness of the Ag compensation layer a simple calculation is conducted: Assuming all silver atoms of this layer contribute to the compensation of the off-stoichiometry of the thin films, the necessary thickness of the Ag compensation layer can be calculated by matching the amount of silver supplied from the Ag compensation layer $n(\text{Ag})_{\text{Ag}}$ with the deficiency in

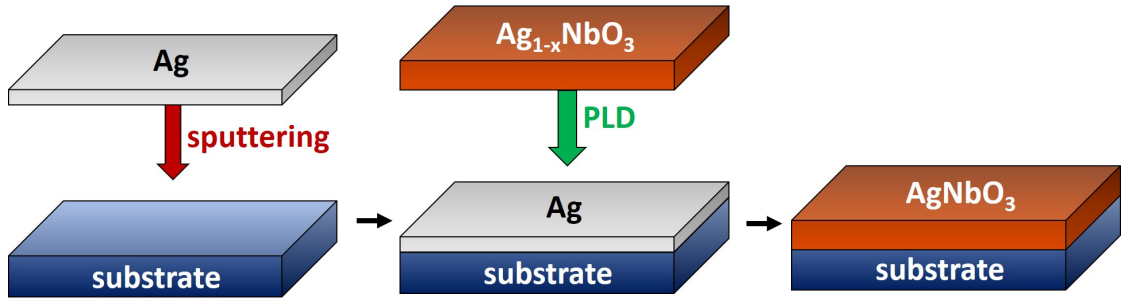


Figure 5.3.3: Schematic illustration of the method applied to compensate for the Ag deficiency in thin films grown from a AgNbO₃ target in PLD.[155]

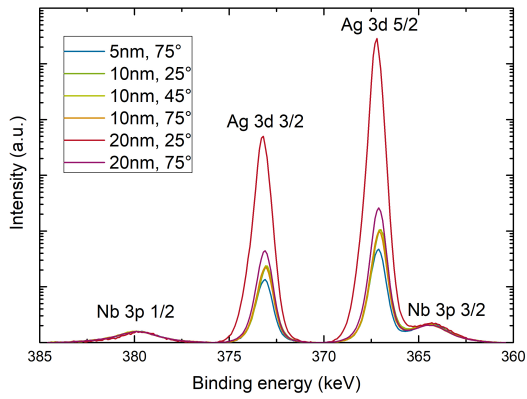
the grown thin film, Ag_{1-x}NbO₃:

$$\begin{aligned}
 n(\text{Ag})_{\text{Ag}} &= x \cdot n(\text{Ag})_{\text{AgNbO}_3} \\
 \frac{V_{\text{Ag}} \cdot \rho_{\text{Ag}}}{M_{\text{Ag}}} &= x \cdot \frac{V_{\text{AgNbO}_3} \cdot \rho_{\text{AgNbO}_3}}{M_{\text{AgNbO}_3}} \\
 t_{\text{Ag}} &= x \cdot \frac{t_{\text{AgNbO}_3} \cdot \rho_{\text{AgNbO}_3} \cdot M_{\text{Ag}}}{M_{\text{AgNbO}_3} \cdot \rho_{\text{Ag}}}
 \end{aligned} \tag{5.1}$$

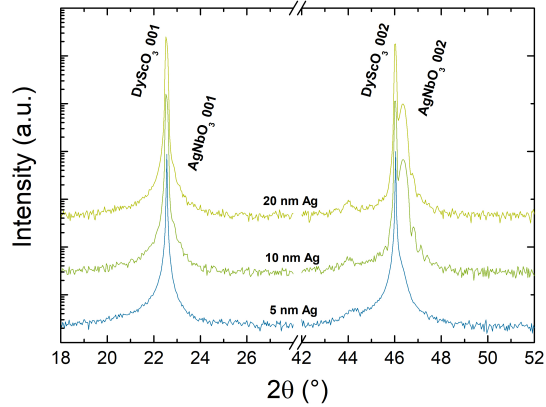
In these equations x refers to the amount of silver deficiency, V_i is the volume of layer i , ρ_i its density, M_i the molar mass and t_i the thickness of the respective layer. Exemplary, for a deficiency of $x = 0.3$, which is among the films with the best composition during the parameter sweep, see Figure 5.3.1, this results in the following ratio:

$$t_{\text{Ag}} = 0.084 \cdot t_{\text{Ag}_{0.7}\text{NbO}_3} \tag{5.2}$$

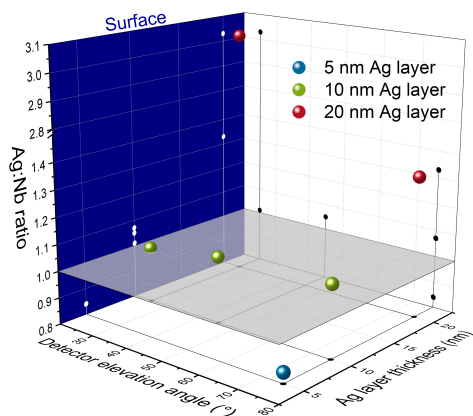
Therefore, in this case, for the growth of a 20 nm thick AgNbO₃ film, a compensation layer of 1.7 nm would be sufficient. However, additional effects like evaporation of silver before the film deposition starts, or diffusion of silver into the substrate creates the necessity of a thicker Ag compensation layer for a successful compensation. Thus, the AgNbO₃ growth on DyScO₃ substrates which are covered with 5 nm, 10 nm and 20 nm thick Ag compensation layers is investigated. The films are grown with an oxygen pressure of 0.67 mbar, a temperature of 700 °C, a fluence of 1.5 J · cm⁻², a substrate-target distance of 40 mm and a frequency of 4 Hz, corresponding to one of the films with the smallest off-stoichiometry. Each film is grown with 2000 laser pulses. The resulting XPS measurement of the Ag-3d and Nb-3p orbitals, the $\theta - 2\theta$ scans and the extracted cation stoichiometry are shown in



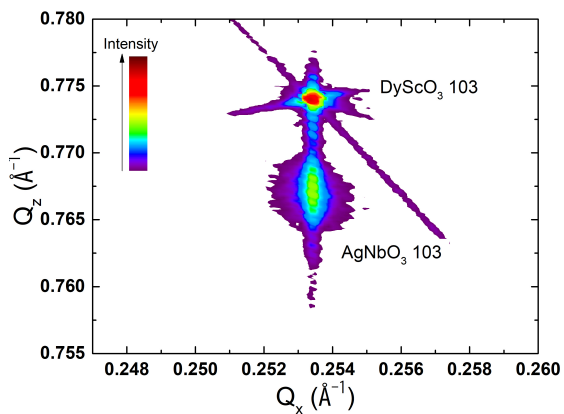
(a) XPS measurement of the Ag-3d orbital. All spectra are normalised to the Nb-3p peak.



(b) θ - 2θ -scans of thin films grown from a stoichiometric AgNbO_3 target.



(c) Cation stoichiometry of the thin films extracted from the XPS measurements in dependence on the Ag layer thickness and the detector angle.



(d) RSM of the AgNbO_3 thin film with a Ag compensation layer of 10 nm.

Figure 5.3.4: Evaluation of the impact of the Ag compensation layer on the film growth and phase formation of AgNbO_3 . Three samples with increasing Ag compensation layer thickness of 5 nm, 10 nm and 20 nm on DyScO_3 are investigated.[155]

Table 5.3.2: Cation stoichiometries of thin films grown from an AgNbO₃ target with an Ag compensation layer. The stoichiometries are extracted from the XPS measurements shown in Figure 5.3.4a.

Ag layer thickness (nm)	5	10	10	10	20	20
Detector angle (°)	75	75	45	25	75	25
Ag:Nb ratio	0.84	1.07	1.05	1.01	1.33	3.03

Figure 5.3.4.

As observed in the vicinity of the 002 substrate reflection of the $\theta - 2\theta$ scans (Figure 5.3.4b), for the sample with a silver thickness of 10 nm, distinct phase formation of AgNbO₃ is evident. The film reflection is accompanied by the presence of Laue oscillations, indicative of high crystalline quality. This suggests successful compensation of the Ag deficiency, as none of the previously grown samples from Figure 5.3.1 exhibit the AgNbO₃ reflection in XRD. The analysis of the Laue oscillations reveals a film thickness of approximately 30 nm for the thin film with a 10 nm Ag compensation layer thickness.

To investigate if the Ag compensation layer can counteract the deficiency throughout the entire film, XPS measurements are conducted to quantify the composition at the film surface (see Figure 5.3.4a). Additional measurements are performed for the films grown on Ag compensation layers with thicknesses of 10 nm and 20 nm, taken at different elevation angles of the XPS detector to extract the depth distribution of the Ag content. At an elevation angle of 75°, the detector is nearly perpendicular to the sample surface, resulting in the maximum analysis depth of the spectrometer. With the detector positioned at 25°, the analysis depth is reduced by a factor of $\cos(50^\circ) = 0.64$.

The cation stoichiometries obtained from the XPS analysis are presented in Table 5.3.2 and visualised in Figure 5.3.4c. When using an Ag compensation layer with a thickness of 5 nm, an increase in the silver content is observed compared to previous attempts without this compensation layer (Figure 5.3.1). However, a silver deficiency in the film still persists. By increasing the Ag compensation layer thickness to 10 nm and 20 nm, substantial improvement is achieved towards a stoichiometric thin film. The latter case exhibits a slight Ag excess with a cation ratio of 1.33 at an elevation angle of 75°.

For the 10 nm thick film, the stoichiometry remains relatively constant at different elevation angles, indicating a saturation of Ag throughout the film at the stoichiometric ratio of AgNbO₃. However, in the case of the 20 nm thick film, the extracted Ag content varies by more than 200% with the detector elevation angle. While the ratio shows a small Ag excess at an angle of 75°, a stronger Ag excess is revealed at 25°, with more

than 3 Ag atoms for every Nb atom. This observation unveils the behaviour of the Ag compensation layer during thin film growth: As the AgNbO₃ thin film is deposited, Ag tends to diffuse through the growing film towards the surface, filling up the Ag vacancies along the way. The fraction of Ag that does not contribute to the phase formation by filling the vacancies within the film continues its diffusion and accumulates at the newly formed surface. Continuing the film growth would lead to a repetition of this process until the Ag is used up. As a result, even AgNbO₃ films with thicknesses exceeding 30 nm can be successfully grown by employing the Ag compensation layer method. Further, little to no Ag appears to remain in the thin film as interstitial, which would deteriorate the crystalline quality.

In contrast to the calculated amount of Ag required for compensation, less than 2 nm for a 20 nm thick film, the actual necessary thickness appears to be 10 nm. Consequently, a significant fraction of Ag from the Ag compensation layer does not contribute to compensation but sublimates or diffuses into the substrate. This occurs likely already before the deposition starts, as the substrate is heated with a rate of 50 K · min⁽⁻¹⁾ to the deposition temperature, resulting in relatively long times at elevated temperatures. Considering the high volatility of Ag, it is not surprising that most of the Ag compensation layer disappears before the growth of AgNbO₃. This secondary effect, however, can simply be covered by an additional increase of the thickness of the Ag compensation layer, as the results have shown.

Although the compensation method presented above allows for the growth of stoichiometric, phase-pure AgNbO₃ thin films, the question of their epitaxial nature remains. This uncertainty arises due to the presence of an amorphous Ag layer between the substrate and the growing thin film. To address this issue, a RSM of the AgNbO₃ film grown with the 10 nm thick Ag compensation layer is taken, see Figure 5.3.4d. For both the reflection of the AgNbO₃ as well as that of DyScO₃, an identical in-plane lattice parameter is observed, proving the epitaxial nature of the AgNbO₃ thin films. How exactly the epitaxial growth can be preserved through the Ag compensation layer has not been investigated, however, this behaviour is likely related to the formation of the Ag compensation layer by sputtering: While the discussion so far considered a rigid film of Ag, the sputtering of such thin coverage is rather resulting in local islands of silver than in a rigid layer. Thus, the AgNbO₃ film in PLD can grow directly on the substrate, while the extra silver ions are supplied from these islands. Consequently, the proposed method allows for the growth of fully strained epitaxial stoichiometric AgNbO₃ films. Considering this image, with increasing thickness of the Ag compensation layer, there should exist a critical thickness, upon which this segregation into islands would cover the whole substrate. Then, no epitaxial growth is possible anymore. This question will be addressed in the following in more detail.

Table 5.3.3: Lattice parameters of AgNbO₃[60] and the substrates investigated in this section. For non-cubic perovskites, the corresponding pseudo-cubic lattice parameters are calculated.[31] The induced strain for epitaxial growth of AgNbO₃ is given in the last column. For this calculation it is assumed that the orientations align such that the lowest mismatch is achieved.

Material	<i>a</i> (Å)	<i>b</i> (Å)	<i>c</i> (Å)	Strain in AgNbO ₃ (%)
AgNbO ₃	3.911	3.942	3.942	
SrTiO ₃	3.905	3.905	3.905	0.55
DyScO ₃	3.945	3.943	3.943	-0.05
GdScO ₃	3.965	3.961	3.961	-0.52

5.3.3 Versatility of the Ag Compensation Method

The experimental results so far revealed the feasibility of the compensation method for the chosen thickness and substrate. However, for investigations into the nature of the AFE for AgNbO₃ thin films, different film thicknesses and substrates become necessary. Therefore, the Ag compensation method has to be extended to apply to other film thicknesses and substrates as well. Similar to NaNbO₃, for AgNbO₃ appropriate substrate are chosen such that the impact of the strain from compressive to tensile can be investigated. The corresponding substrates and strains are given in Table 5.3.3.

The angle dependent XPS analysis in the last section exposed the behaviour of the excess silver in case of thicker Ag compensation layers: The surplus diffuses through the growing layer and accumulates on the surface of the growing films. This result indicates the possibility to grow thicker, stoichiometric films as well. However, the relation between an increase of the film thickness and the necessary thickness of the Ag compensation layer needs to be clarified. In the previous part, it has already been analysed that around 80 % of the Ag compensation layer does not contribute to the film growth but disappears in the process. Assuming this occurs during the heating step, before the actual deposition is started, an extrapolation of the necessary Ag compensation layer thickness by a linear equation $t_{Ag} = m \cdot t_{Ag_{1-x}NbO_3} + b$ with b corresponding to the loss before the deposition starts should be sufficient to calculate the necessary Ag compensation layer thickness for the desired film thickness.

First, this function needs to be fitted to data points to extract the actual slope m and the loss b . Hence, a series of AgNbO₃ films with increasing thickness are grown on LaNiO₃/SrTiO₃ substrates, where LaNiO₃ is added to enable electrical characterisation of AgNbO₃. To

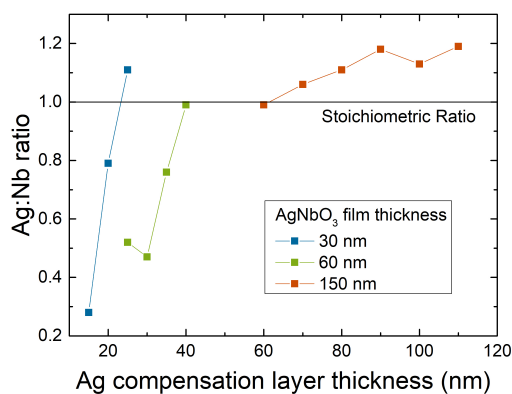


Figure 5.3.5: Dependence of the cation ratio on the Ag compensation layer thickness for different film thicknesses for growth of AgNbO_3 thin films on $\text{LaNiO}_3/\text{SrTiO}_3$. [155]

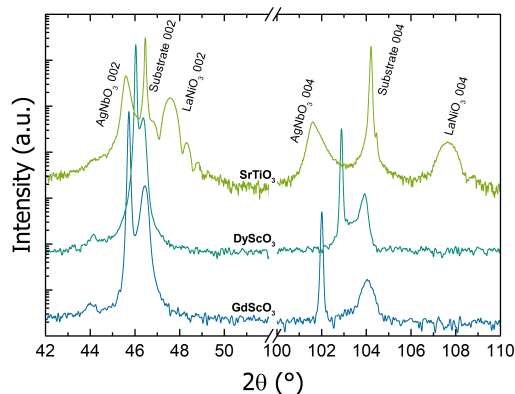


Figure 5.3.6: $\theta - 2\theta$ -scans of AgNbO_3 grown on different substrates, utilising the developed Ag compensation method. [155]

construct the fitting curve, three thicknesses are selected, controlled by the number of laser pulses: 2000, 4000 and 10000 laser pulses. For each thickness, multiple AgNbO_3 films are grown with different thicknesses of the Ag compensation layer. These are then analysed via XRD in regards to their phase and via XPS to extract the cation stoichiometry. The resulting cation ratio in dependence on the AgNbO_3 film thickness and Ag compensation layer thickness is shown in Figure 5.3.5. The given thickness values are extracted from the Laue oscillations for the film with 2000 shots. For thicker films, no Laue oscillations could be resolved anymore and the thickness is calculated based on the growth rate calculated from the thinner films. This amounts to an AgNbO_3 film thickness of 30 nm for 2000 laser pulses, 60 nm for 4000 laser pulses and 120 nm for 10000 laser pulses.

An approximately 23 nm thick Ag compensation layer is necessary to achieve a stoichiometric AgNbO_3 film with a thickness of 30 nm (see Figure S1 for the XRD analysis). Interestingly, this Ag compensation layer needs to be more than twice as thick as the AgNbO_3 film on DyScO_3 with the same thickness, indicating a significant impact of the change of the material below the Ag compensation layer. Nonetheless, this approach clearly demonstrates the adaptability of the method for growing epitaxial heterostructures with stoichiometric AgNbO_3 films on different substrates by adjusting the thickness of the Ag compensation layer.

For AgNbO₃ films with thicknesses of 60 nm and 150 nm, the ideal Ag compensation layer thicknesses are 40 nm and 60 nm, respectively (see Figure S1 for the XRD analysis). Hence, the required Ag compensation layer thickness t_{Ag} is not directly proportional to the AgNbO₃ film thickness. It is important to note that temperature dependence has not been considered in this analysis and the temperature has been kept constant throughout the different PLD processes. Based on the simplified model that a portion of the Ag is removed before the film deposition, an extrapolation of this linear behaviour for the growth on LaNiO₃/SrTiO₃ results in approximately 18 nm of Ag being dispersed before the deposition starts.

$$t_{Ag} = 0.29 \cdot t_{Ag_{1-x}NbO_3} + 18 \text{ nm} \quad (5.3)$$

This calibration curve can be utilised to extract the necessary thickness of the interfacial Ag compensation layer for any desired AgNbO₃ film thickness. It should be noted, that at larger thicknesses of this compensation layer, no epitaxial growth is expected, as the material deposits on the amorphous silver instead of the substrate and, thus, cannot form an epitaxial relation. Surprisingly however, even the AgNbO₃ film grown on 60 nm of Ag still grows fully strained (see Figure 5.3.7). Since it is doubtful, that the epitaxial growth can be maintained through such a thick amorphous layer, rather the image of the Ag compensation layer as a rigid layer is misleading, as mentioned before. This interfacial layer is more likely to grow as islands on the surface of the substrate by the sputtering process, allowing the PLD deposited material to reach the substrate in the gaps and grow the epitaxial film there. The identification, above which thickness the epitaxial growth is prevented, however, goes beyond the scope of this thesis. However, with films at 150 nm revealing epitaxial growth, relaxation due to the accumulated strain energy might precede the loss of the epitaxial relation.

As the transfer of the growth from DyScO₃ to LaNiO₃/SrTiO₃ has shown, change of the material below the Ag compensation layer has a significant influence on the necessary thickness for stoichiometric growth of AgNbO₃ thin films. For the investigation of the strain dependence on the AFE behaviour of AgNbO₃, growth on different substrates is necessary, and, has to be optimised individually. The substrates are chosen such that the impact of strain from compressive to strained growth can be investigated, see Table 5.3.3. For the investigation of the strain impact, the growth of AgNbO₃ thin films on DyScO₃ and GdScO₃ is optimised for 150 nm thick films, comparable with the thickest film on LaNiO₃/SrTiO₃. The growth on these substrates shows similar behaviour in regards to the Ag compensation layer and stoichiometric films are obtained for a Ag compensation layer with a thickness of 50 nm, the XRD results of these films are shown in Figure 5.3.6. This similarity is likely related to their chemical resemblance. Also for AgNbO₃, the variation of the substrate and, correspondingly, the epitaxial strain manifests in a change of the

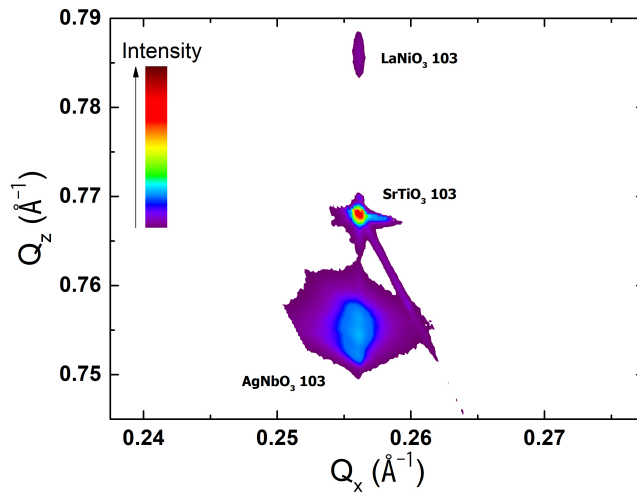


Figure 5.3.7: RSM of 150 nm thick AgNbO_3 on $\text{LaNiO}_3/\text{SrTiO}_3(100)$, grown with a Ag compensation layer thickness of 60 nm.[155]

out-of-plane lattice parameter due to the Poisson effect. The AgNbO_3 thin film grown on $\text{LaNiO}_3/\text{SrTiO}_3$ shows the largest out-of-plane lattice parameter, which then subsequently decreases for increasing tensile strain.

5.4 Conclusion

This chapter, which is concerned with growth optimisation of epitaxial thin films of NaNbO_3 and AgNbO_3 , investigates the challenges associated with growth of phase pure thin films. It can be concluded, that, despite complications in the film growth process, for both materials epitaxial films can be achieved via PLD. The specifics of this process are summarised by regarding the initial questions of this chapter:

1. **What is the central difficulty for growth of NaNbO_3 and AgNbO_3 thin films?**
For both materials, the A-site cation is the origin of complications. This is known for the synthesis of bulk materials, but is shown to apply to thin film growth as well. While one of the strengths of PLD is the stoichiometric transfer of material from a target to the film, for these materials additional measures have to be taken. Hereby, in both cases, a deficiency of the A-site cation is observed, which can be related to a desorption for sodium due to its high volatility, while the precise origin of the silver

loss remains unclear.

2. How can this difficulty be overcome to achieve growth of epitaxial thin films?

For the film growth of NaNbO_3 by PLD, the loss of sodium can be effectively mitigated by an increase in the pressure of the oxygen background gas. This prevents the desorption of the volatile Na_2O species, and at a background pressure of 0.53 mbar during the PLD process, stoichiometric NaNbO_3 thin films are obtained.

For the film growth of AgNbO_3 on the other hand, parameter optimisation does not lead to a compensation of the silver loss in the growth process. Instead, a novel compensation method is designed, based on the high diffusivity of silver ions at elevated temperatures. A thin layer of silver sputtered on the substrate before the deposition serves as an additional supply of silver for the film growth and can compensate the loss in the PLD process. The film growth has been shown to be epitaxial despite this interfacial layer, enabling the investigation of strain dependent parameters with this method.

3. How do the growth parameters translate to other substrates to achieve different strain states for NaNbO_3 and AgNbO_3 ?

The translation of the growth of NaNbO_3 onto different substrates or with the addition of a bottom electrode consisting of PLD grown LaNiO_3 can be achieved without variation of growth parameters. The same parameters as previously optimised are found to lead to high quality thin films on the other substrates as well.

The translation of the compensation process for growth of AgNbO_3 thin films, however, shows the necessity for individual optimisation of the thickness of the Ag compensation layer. Due to the different surface energies involved, the silver behaves different depending on the material it is deposited on, resulting in different dissipation behaviour before the deposition of the AgNbO_3 thin film. Thus, for a translation of the growth to other substrates, as well as to change the AgNbO_3 film thickness, the thickness of this Ag compensation layer has to be calibrated.

6 Strain Impact on the Crystallographic Structure

6.1 Motivation

With the ability to synthesise high quality thin films of NaNbO_3 and AgNbO_3 on different substrates, the investigation into the impact of strain on the AFE effect is enabled. For both materials, available literature of thin films suggests a stabilisation of the FE phase by epitaxial growth. Especially for NaNbO_3 which shows only a small energy difference in bulk ceramics between the AFE and FE phase, all investigations into thin films conclude with FE properties, independent of the synthesis method and film thickness.[101, 97, 146, 29, 100, 102, 105] This result is either concluded based on the measurement of a FE hysteresis loop[97, 146, 29, 102, 105] or via piezoresponse force microscopy (PFM).[101, 100] The latter measures the deformation of the material under an applied AC voltage from a nanometer sharp probe tip, i.e. it directly measures the converse piezoelectric effect. However, those methods would characterise bulk NaNbO_3 as a FE material as well, due to the metastability of the FE phase.[158] Thus, a thorough analysis of the structural properties is necessary to identify the true ground state of NaNbO_3 thin films.

For AgNbO_3 on the other hand, both reports of FE[30, 110] as well as AFE[159, 113, 28] thin films exist. This poses the question, where this difference in their dielectric behaviour originates and how this can be manipulated in the desired way. So far no comprehensive study on the AgNbO_3 thin films has been conducted to clarify the appearance of the AFE or FE phase.

One characteristic difference between the FE and AFE structure of NaNbO_3 and AgNbO_3 is the multiplicity of the unit cell based on the simple perovskite cell: While the FE structure has to be extended to twice the basic perovskite cell to take the ion displacements and octahedral tilts into account, the antiparallel ion displacements and accompanying octahedral tilts result in the length of one direction of the AFE structure being four times that of the original perovskite cell, with the others lattice parameters are doubled. This difference can be identified by additional reflections in structural characterisation techniques. As the $\frac{1}{4}$ superlattice peaks originate partially from the ion displacements,

XRD can be utilised to identify the ground state, as the ions provide sufficient scattering contrast.[27, 14]

Thus, a thorough structural analysis of the properties of NaNbO_3 and AgNbO_3 thin films is necessary to clarify not only the fundamental structural properties of the films, but also to differentiate between the FE and AFE phases:

1. **What is the stability range of epitaxial thin films of NaNbO_3 and AgNbO_3 on different substrates until a relaxation occurs?**
2. **Does the epitaxial growth retain the AFE phase or does it stabilise the FE phase?**
3. **What is the impact of different magnitudes of strain on the phase balance? Do different levels of strain stabilise different phases or does epitaxial growth favour only one phase?**

6.2 NaNbO_3 Heterostructures

In case of NaNbO_3 , the analysis of the ground state is carried out for the same samples which are later analysed electrically, to get a fully conclusive picture of the AFE effect from the structural and electric point of view. Hence, all thin films discussed in this part consist of the following layer structures: $\text{NaNbO}_3/\text{LaNiO}_3/\text{Substrate}$. For each substrate, films with increasing NaNbO_3 thickness are grown to investigate the behaviour of increasing strain energy on the phase formation and examine strain incorporation and the relaxation threshold.

For consistency, in the following the notation utilised for the description of the different growth orientations of NaNbO_3 and reference to lattice parameters is based on the PC notation, as given in Table 5.2.3.

6.2.1 Strain State

An increase of film thickness is accompanied by an increase of the total strain energy in the films. Hence, once the strain energy exceeds the defect formation energy, the film relaxes to the bulk structure by formation of defects.

To investigate how the strain energy affects the phase balance, films with increasing thickness are grown on each substrate chosen for the investigation of the strain impact, see Table 5.2.3. These films are characterised by XRD to identify the formation of additional phases or changes in the out-of-plane lattice parameters.

The results of the $\theta - 2\theta$ scans on the different substrates together with the extracted

out-of-plane lattice parameter of the NaNbO_3 thin films are shown in Figure 6.2.1. The film quality can be determined by examining their reflections in the XRD patterns. The 001 reflection demonstrates two sets of extensive Laue oscillations for thinner films. These sets originate from the two grown thin films, NaNbO_3 as well as LaNiO_3 . This effect can be observed on all substrates, indicating the successful transfer of the growth conditions to the different substrates, as discussed in the last chapter. For increasing thickness of the NaNbO_3 , the oscillations corresponding to this layer gradually disappear and only those of LaNiO_3 remain. The thickness of the films is determined by analysing the Laue oscillations. For thicker films, where Laue oscillations cannot be resolved, the thickness is calculated based on the number of laser pulses and the growth rate of NaNbO_3 , which is calibrated with the thinner films.

Meanwhile, the 004 reflection is more effective in distinguishing between different phases and orientations as the relative angle difference between the reflections leads to a larger effective angle difference at higher angles. Thus, the 004 reflections are used to identify a transition from one reflection for the NaNbO_3 thin film to the appearance of other contributions on each substrate. The lattice parameters of the corresponding NaNbO_3 films are determined by fitting the 001/100 reflections and applying the Nelson-Riley method for correction.[130] These values are plotted against the film thickness of NaNbO_3 below the XRD scan of the respective film-substrate combination. The graphs also display the lattice parameter of the bulk structure and the expected lattice parameter for a fully strained film, based on the Poisson effect. The latter is calculated using the general strain-stress relation, where ν is the Poisson ratio, approximated as 0.3.[93] In the case of growth on SrTiO_3 , the strained lattice parameters of the different orientations are given, which is more suitable for the following discussion.

Figure 6.2.1a shows XRD patterns for NaNbO_3 films grown on LSAT under compressive strain. Even at a low thickness of 70 nm, two contributions from NaNbO_3 (NaNbO_3 004 and NaNbO_3 004*) are detected, both possessing a lattice parameter close to the expected value for a strained film. A third reflection (NaNbO_3 400) appears at thicknesses around 250 nm with a lattice parameter close to the bulk lattice parameter of NaNbO_3 (a_{PC}). Thus, this contribution can be attributed to a relaxation phenomenon. This assumption is further investigated by RSMs recorded around the 103 substrate reflection, confirming partial relaxation at thicknesses of 250 nm and above, see Figure 6.2.3a (All RSMs are given in Figure S2). Meanwhile the secondary contribution at lower thicknesses (NaNbO_3 004*) appears to be fully strained. The appearance of this reflection can originate from a rotation of the orientation of NaNbO_3 or defect formation in the thin film. The first is unlikely for this case, as the lattice parameter change is small compared to the expected change for an orientation change. The latter is often observed to cause lattice parameter shifts in perovskite thin films,[161, 162] and, as NaNbO_3 is prone to defect formation,[163]

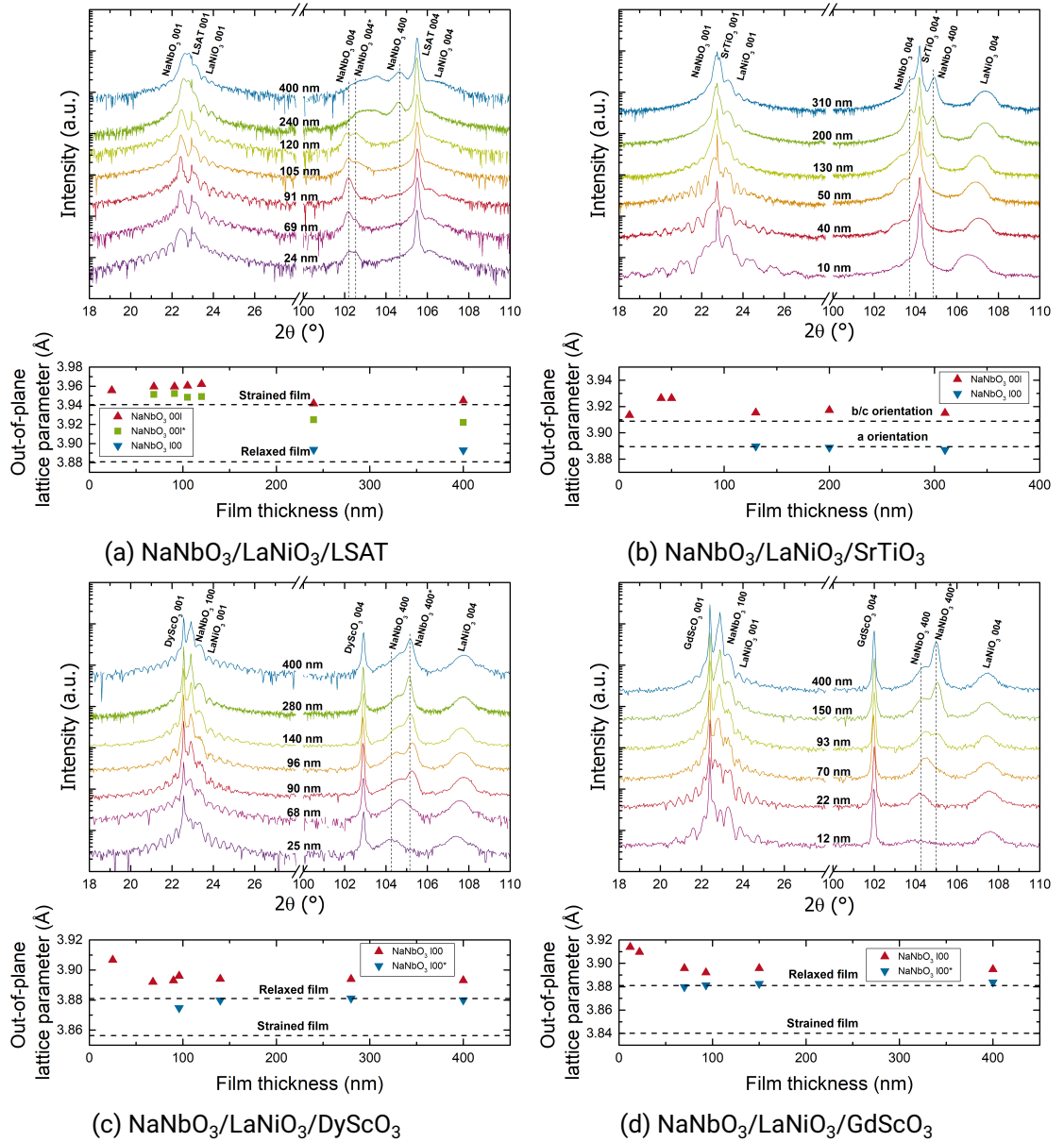


Figure 6.2.1: $\theta - 2\theta$ scans of NaNbO_3 thin films grown on different substrates. Shown are the regions around the 001 and 004 substrate reflections and the extracted lattice parameters from these scans. For the latter, the different contributions of NaNbO_3 are marked with the corresponding orientation, as given in Table 5.2.3. For multiple reflections related to one orientation, the additional one is marked with a “*”. Reprinted with permission.[160]

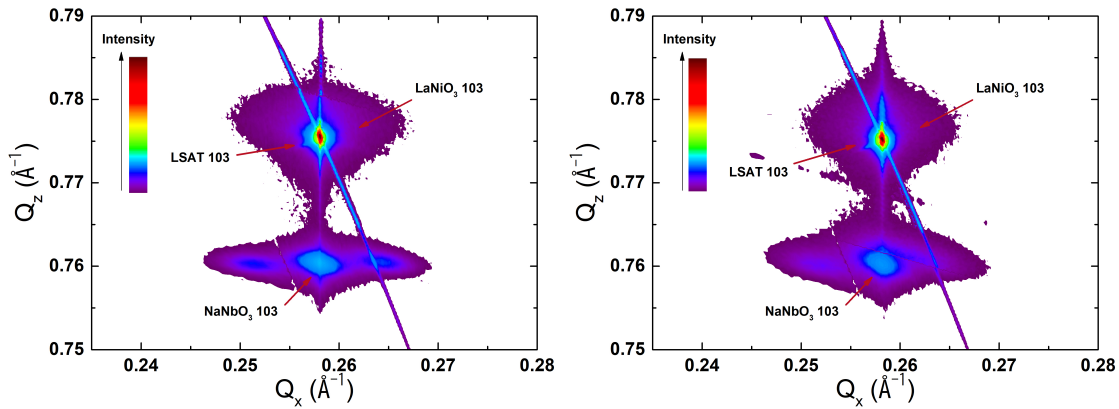


Figure 6.2.2: RSMs of NaNbO_3 grown on $\text{LaNiO}_3/\text{LSAT}$ around the 103 substrate reflection with a NaNbO_3 thicknesses of 91 nm (*left*) and 105 nm (*right*). Satellite peaks horizontally adjacent to the thin film reflection are visible. Reprinted with permission.[160]

remains a plausible cause for this observation. RSMs on these thin films reveal the presence of satellite peaks with different Q_x but the same Q_z value as the NaNbO_3 film reflection for NaNbO_3 films with thicknesses of 91 nm and 105 nm, see Figure 6.2.2. This is an indication for the presence of an in-plane periodic modulation, and, thus, the existence of a structural ordering in the film plane, with a periodicity of ~ 15.5 nm. A possible origin for this is a modulation of the out-of-plane polarisation component, which has already been observed for PbTiO_3 thin films and heterostructures.[164, 165]

For the SrTiO_3 substrate, the film can grow under compressive as well as tensile strain depending on the orientation, see Table 5.2.3. Growth under tensile strain should be favourable due to a smaller magnitude of strain. Indeed, as seen in Figure 6.2.1b, the b/c lattice parameter grows initially in the out-of-plane direction, corresponding to growth under tensile strain. Beyond a critical thickness between 50 nm to 130 nm, another reflection appears in the XRD pattern for growth on SrTiO_3 . Calculation of the corresponding out-of-plane lattice parameters reveals different growth orientations of the NaNbO_3 thin films, where the initial orientation matches the growth with the b/c lattice parameter in the out-of-plane direction, while the second reflection appearing between 50 nm and 130 nm matches the growth with the a lattice parameter in the out-of-plane direction. RSMs confirm that both contributions are fully strained, see Figure 6.2.3b, even up to the 310 nm thick film (All RSMs are given in Figure S3). Hence, no relaxation is responsible for this change in the growth of NaNbO_3 , but rather a strain relief mechanism. This is

enabled by the unique combination of the lattice parameters from NaNbO_3 and SrTiO_3 : the material can change the growth orientation to switch from the initial growth under tensile strain to compressive strain. This reduces the overall strain energy in the film, allowing to grow thicker films before a relaxation to the bulk structure occurs. As only small shifts in the lattice parameters are necessary for this change, along with different octahedral rotations, it appears to be favourable to a relaxation by defect formation. Whether this orientation change is reversible, i.e. if the orientation changes back to the initial orientation before the relaxation would occur, has not been investigated.

For growth of NaNbO_3 under tensile strain on DyScO_3 and GdScO_3 , a single contribution for thin films (NaNbO_3 400) is detected until relaxation occurs, and a second contribution with a bulk-like lattice parameter appears (NaNbO_3 400*). This relaxation is confirmed by RSM measurements with a critical thickness of around 90 nm for growth on DyScO_3 and between 22 nm to 70 nm for growth on GdScO_3 (All RSMs are given in Figure S4 and Figure S5, respectively). Due to the larger lattice mismatch for growth on GdScO_3 , this relaxation occurs at a lower thickness. Despite the strained growth, the out-of-plane lattice parameter of the strained phase on both DyScO_3 and GdScO_3 is larger than that of the relaxed phase, whereas the strain should lead to a decrease of the out-of-plane lattice parameter. Further, in both cases, a decrease of the out-of-plane lattice parameter with film thickness is visible until relaxation occurs, upon which it remains at a constant level. This effect could be due to the increase in strain energy in the film, shifting the out-of-plane lattice parameter gradually to lower values due to the Poisson effect. This shift, however, does not mitigate the increase of the out-of-plane lattice parameter compared to the bulk structure. This effect can originate from off-stoichiometry, defect formation or oxygen deficiency.[161] As the film stoichiometry has been optimised via XPS, and synthesis conditions are kept constant, off-stoichiometry of the cations can be excluded. Defect formation, however, is known to shift XRD reflections by several degrees.[161, 162] In combination with the low defect formation energies in NaNbO_3 , especially for Na and O vacancies,[163] this presents a possible origin for the lattice parameter shift. The oxygen content is not analysed from the XPS measurements due to the exposure to air and corresponding adsorption of oxygen on the surface. Thus, oxygen deficiency can contribute to the unexpectedly large increase of the lattice parameter for NaNbO_3 growth under tensile strain, and can also be the cause for the peak splitting observed for growth on LSAT (NaNbO_3 004 and NaNbO_3 004*). That no such effect is visible for growth on SrTiO_3 can be due to the tendency of SrTiO_3 to give away oxygen ions during film growth, which can compensate for the oxygen deficiency in NaNbO_3 . DyScO_3 and GdScO_3 on the other hand have been shown to be stable against oxygen loss,[166] allowing no compensation in the growing thin film.

6.2.2 AFE versus FE Structure

The difference in crystal structure between the AFE and FE phases of NaNbO_3 can be utilised as a criterion to determine its ground state.[158, 14] Thus, additionally, the area of the reciprocal space where the $\frac{1}{4}$ superlattice reflections, characteristic for the AFE phase, are expected, is measured via RSMs. The measurements are taken in the vicinity of the 103_{PC} reflection which has been previously utilised to identify the strain state of the thin films. Hence, the corresponding reflection is $\frac{3}{4}03$ in the in-plane direction or $103\frac{1}{4}$ in the out-of-plane direction for the pseudo-cubic notation. Figure 6.2.3 displays the results for the thickest films on each substrate.

The presence of a $\frac{1}{4}$ superlattice reflection can be identified for two of the four selected substrates, on LSAT and SrTiO_3 . Meanwhile no intensity is detectable in the measured regions for the DyScO_3 and GdScO_3 substrates. This indicates that compressive or small tensile strain supports the formation of a bulk-like AFE ground state, while a larger tensile strain prevents the formation of this phase and most likely leads to the stabilisation of the FE phase. This effect even extends beyond relaxation to the bulk lattice parameters as the measurements are conducted on the thickest films, which are 400 nm thick for both DyScO_3 and GdScO_3 , while the relaxation occurs below 100 nm.

In the case of compressive strain on LSAT, both the in-plane, $\frac{3}{4}03$, as well as the out-of-plane, $103\frac{1}{4}$, direction show superlattice peaks. These can be linked to the respective orientation of NaNbO_3 which produces this reflection, via matching of the reciprocal lattice parameters. This reveals, that the in-plane superlattice reflection stems from the strained NaNbO_3 film, while the out-of-plane superlattice reflection originates from the relaxed fraction. Analysis of the RSM of thinner films on LSAT indeed shows the disappearance of the out-of-plane superlattice reflection while the in-plane one remains (see Figure S8). Thus, the relaxation is accompanied by a rotation of the NaNbO_3 unit cell orientation from the b/c lattice parameter to the a lattice parameter growing out-of-plane. This matches the expected orientations based on the bulk structure of NaNbO_3 : The a lattice parameter, which corresponds to the direction of the fourfold multiplicity, is smaller and, thus, would be predicted to grow in-plane for the strained growth, resulting in the in-plane superlattice reflection. After the relaxation, the crystal structure coincides with that of bulk NaNbO_3 , as validated by the matching lattice parameters and direction of the fourfold lattice parameter.

Similarly, the growth on SrTiO_3 confirms the similarity with the bulk structure of NaNbO_3 . Both orientations of the NaNbO_3 thin film feature the fourfold modulation and result in a superlattice reflection. The b/c -orientation leads to the in-plane superlattice peak and the a -orientation results in the out-of-plane superlattice peak, as expected from the direction of the unit cell multiplicity. Noticeably, the superlattice peak also appears for the

orientation growing with small tensile strain.

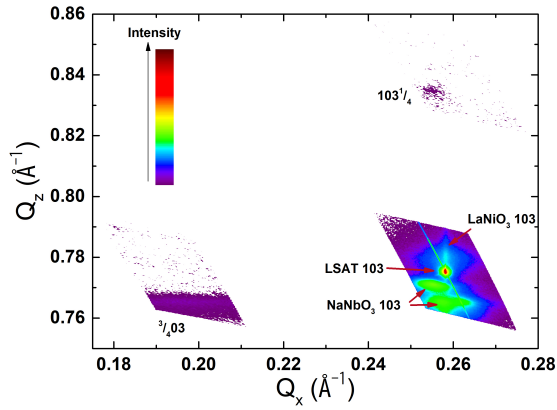
However, for both DyScO₃ and GdScO₃ substrates, the films do not exhibit any intensity beyond background noise in the regions where the superlattice peaks are expected to appear, even though the films are mostly relaxed to the bulk structure. The epitaxial relation on substrates causing tensile strain appears to destabilise the formation of the bulk AFE phase even above the relaxation thickness.

Looking critically at this analysis, the appearance of this superlattice reflection only represents a superstructure with a periodicity of four times the pseudo-cubic lattice parameter of NaNbO₃. Indeed, other effects can be responsible for the appearance of this reflection as well, which are not tied to an AFE ordering. Such a misinterpretation of reflections is not uncommon and can lead to wrong assumptions about the effect in question.[167] Thus, other contributions have to be considered. Ordering phenomena relevant for the present structure which can lead to additional reflections include chemical ordering, octahedral tilts, ion displacements and polarisation modulation.[168, 167, 164, 165]

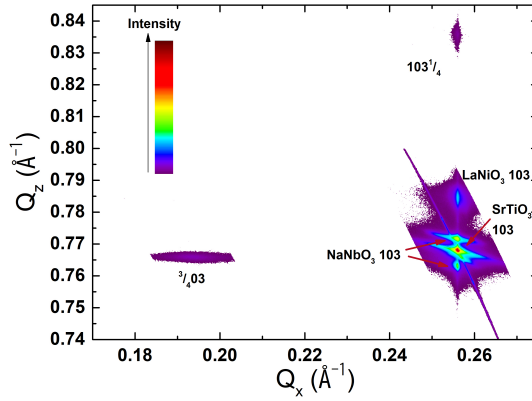
The first effect is commonly regarded for double-perovskites, which are synthesised with two different cations for the *A* or *B*-site in ABO₃ perovskites. These can form ordering structures, leading to superlattice reflections.[169] As NaNbO₃ is a single perovskite, this ordering phenomena can only occur with antisite defects, i.e. Na⁺ on a Nb⁵⁺ site and vice versa. Due to the large difference in the valence state between the cations, this type of defect is highly unlikely.[169]

Octahedral tilts play a significant role in the stabilisation of the perovskite structure for perovskites with a tolerance factor deviating from 1. They can become very complex in AFE perovskites, and can well establish additional superstructures.[170] However, oxygen ions feature a low scattering contrast in X-ray scattering. This is verified via simulation of the intensities of the relevant reflections for X-ray scattering. To compare the influences of the different ordering phenomena on the intensities of the superlattice reflections, the intensity ratio $I_{\frac{3}{4}03}/I_{103}$ is calculated with the program Vesta[44] for Cu K_{α} radiation. This intensity ratio for single crystal NaNbO₃ amounts to 25 %.[50] Removal of Na ion shifts reduces this intensity ratio to 14.3 % while removal of the Nb ion shifts leads to only 0.6 % left. If both cation shifts are neglected, only the octahedral rotations which contribute to the superlattice reflection remain, and only 0.01 % of the intensity of the 103 reflection is left for the superlattice reflection. Given the measured peak heights of less than 2000 cps for the most intense NaNbO₃ 103 reflections, this would amount to 0.2 cps and disappear in the background, unlike the measured reflections.

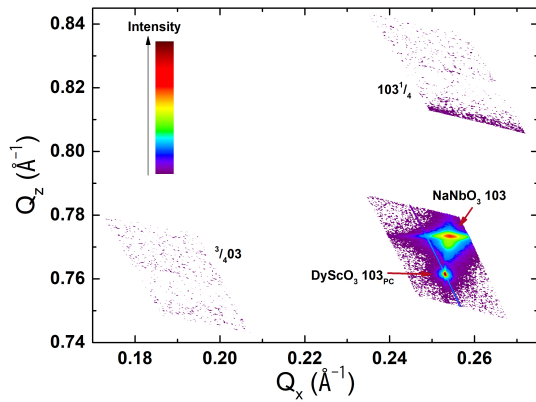
The last two effects, ion displacements and polarisation modulation, are both corresponding to displacements of the cations, among which the AFE ordering is included. For bulk NaNbO₃, specifically the expansion of the unit cell to four times the length of the



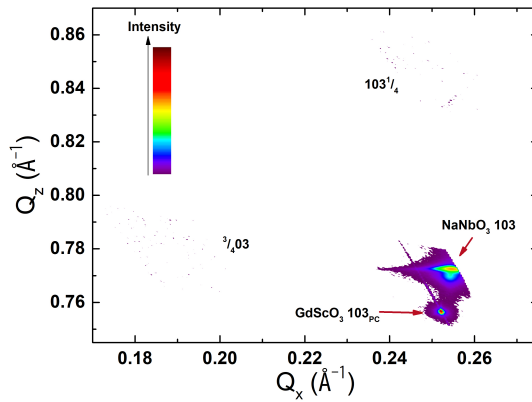
(a) NaNbO₃/LaNiO₃/LSAT



(b) NaNbO₃/LaNiO₃/SrTiO₃



(c) NaNbO₃/LaNiO₃/DyScO₃



(d) NaNbO₃/LaNiO₃/GdScO₃

Figure 6.2.3: RSMs of NaNbO₃ thin films grown on different substrates around the 103 substrate reflection as well as at the regions for the $\frac{3}{4}03$ and $103\frac{1}{4}$ superlattice reflections. Reprinted with permission.[160]

basic perovskite unit cell is due to the antiparallel ion ordering. While other kinds of polarisation ordering cannot be fully excluded, the similarity of the effect observed for the thin films to bulk NaNbO_3 , up to the matching directions for the superlattice reflection, hints strongly at the presence of AFE ordering rather than an exotic polarisation ordering which additionally would need to exhibit the same multiplicity as AFE in bulk NaNbO_3 . For the 310 nm thick film on SrTiO_3 , additional high-resolution transmission electron microscope (HRTEM) pictures are taken to further investigate the structural behaviour of NaNbO_3 . These provide validation of the indications suggesting an antipolar ground state in the NaNbO_3 thin films. As depicted in Figure 6.2.4a, the HRTEM image reveals a distinctive structural modulation, characteristic of the AFE phase.[171] Notably, this modulation undergoes an orientation change, consistent with the observations from XRD. For a more detailed analysis, the modulated feature is magnified and processed with false colour, see Figure 6.2.4b. This processing highlights two types of modulation: a fourfold modulated antipolar phase with a modulation length of 1.532 nm, and a sixfold modulated planar defect with a modulation length of 2.298 nm. The former describes well the AFE unit cell of NaNbO_3 , with alternating of two ions displaced parallel followed by two ions displaced antiparallel to these.[158] The latter on the other hand is more difficult to interpret, possibly a deviation from the antipolar phase modulation is created due to the vicinity of the orientation change in the thin film.

To gain additional insights, a fast-Fourier transform (FFT) of the HRTEM image is presented in Figure 6.2.4c. The FFT clearly shows the emergence of $\frac{1}{4}$ -superlattice reflections. It is worth noting that these reflections appear in both directions since the imaging area is selected across the boundary where these two modulated structures meet. Further, regions devoid of this modulation also exist in the sample. The nature of these regions remains uncertain; they might indicate a coexistence of a FE phase alongside the AFE phase, or the fourfold lattice parameter could be parallel to the zone axis, rendering it invisible in the FFT and HRTEM analysis. Further investigation is required to ascertain these possibilities conclusively.

Thus, a clear trend for the ground state of NaNbO_3 in dependence on the strain can be formulated: For compressive strain, independent of the magnitude, as well as for small tensile strains, a bulk-like AFE structure can be detected. Meanwhile for larger tensile strains, the formation of this phase appears to be inhibited. This finding strikes as contradictory to present literature on thin film NaNbO_3 , which exclusively report the FE phase. However, in these reports, the phase is concluded based on the behaviour upon application of an electric field, which would result in a misinterpretation of the ground state for bulk NaNbO_3 as well.[29, 23] Computational predictions on the other hand so far point towards a stabilisation of the AFE state for tensile strain, while films under compressive strain are expected to exhibit FE behaviour.[106, 31] This is contradictory

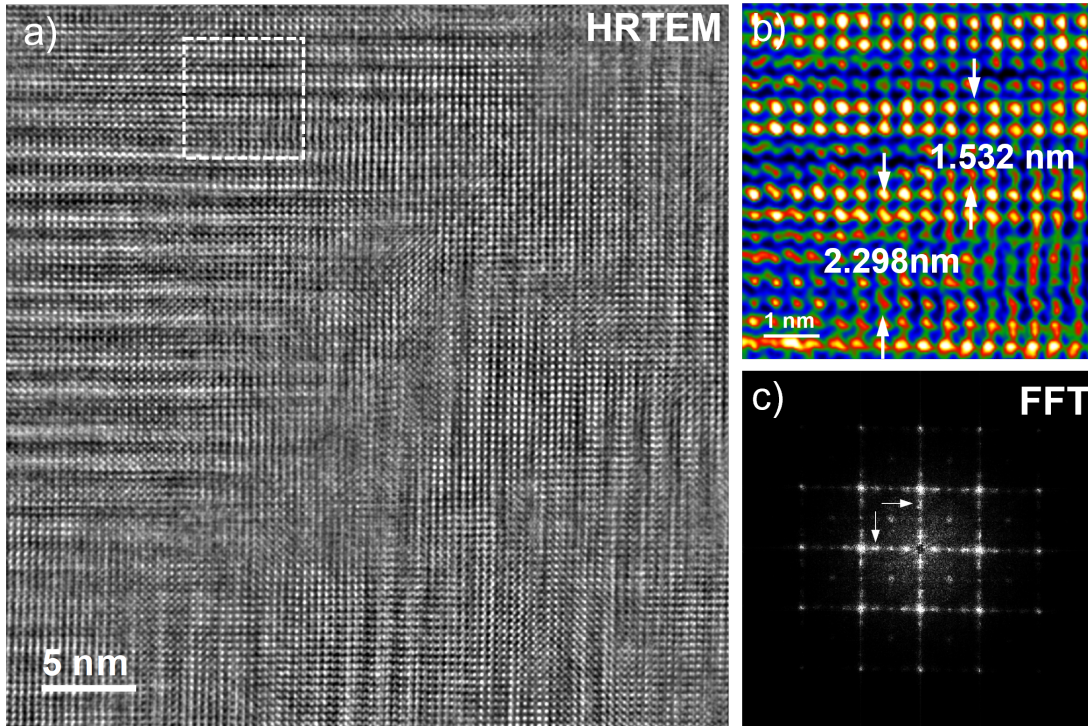


Figure 6.2.4: TEM micrographs of the 310 nm thick NaNbO_3 film. *a)* HRTEM picture revealing the modulation characteristic for AFE materials, which changes from in-plane (bottom) to out-of-plane (top). *b)* Enlarged picture from the dashed white rectangle in *a)*, indicating different modulations, processed with false colour *c)* FFT of the region shown in *a)*. One set of $\frac{1}{4}$ -superlattice reflections can be seen for the horizontal as well as vertical direction, indicated by the arrows, due to the change from in- to out-of-plane modulation. Reprinted with permission.[150]

to the presented observations on the structure of NaNbO_3 thin films. Given the complex nature of AFE as well as NaNbO_3 many assumptions are made in these computational works, which could be essential to the phase balance in the end. With the growth of epitaxial NaNbO_3 thin films, the symmetry of the substrates also play a role, which adds another variable to this calculation.

It should be noted, that in the discussion so far, either of a bulk-like AFE structure due to the similarities to bulk NaNbO_3 , or an antipolar structure is mentioned. This stems from the complex definition of AFE, which corresponds to a combination of two phases: a low energy antipolar phase and a FE phase at slightly higher energy. As the experiments in this chapter have only probed the ground state, no conclusion towards the classification as an AFE material can be made. Only the presence of a necessary condition, an antipolar ground state, can be concluded. Due to the similarities with the bulk AFE structure of NaNbO_3 , the term “bulk-like AFE” is occasionally used. To determine whether the NaNbO_3 thin films can be classified as true AFE materials, proof of a higher-energy FE phase is essential. Thus, further characterisation is necessary to describe the NaNbO_3 thin films and reveal and explain the differences to results in literature. Therefore, the next chapter covers the electrical characterisation of these films.

6.3 AgNbO_3

For AgNbO_3 , due to the complexity of the growth optimisation, films with a thickness of ~ 150 nm are compared on the three substrates chosen for the strain investigation, see Table 5.3.3. For growth on DyScO_3 and GdScO_3 , these are grown without a bottom electrode, while for growth on SrTiO_3 , the optimised film with LaNiO_3 between the AgNbO_3 and the substrate is compared. However, as LaNiO_3 grows fully strained, no structural difference to direct growth on SrTiO_3 is expected.

Similar to the discussion on NaNbO_3 , all growth orientations of AgNbO_3 and reference to lattice parameters is based on the PC notation, as given in Table 5.3.3.

6.3.1 Strain State

The strain state of the films is evaluated by RSMs around the 103 substrate reflection, see Figure 6.3.1. For all three films, the reflection features the same in-plane lattice parameter as the corresponding substrate, indicating a fully strained growth. For the growth on GdScO_3 a broadening of the AgNbO_3 film reflection is observed, which is perpendicular to the scattering vector and, thus, an indication of increased mosaicity on this substrate.[172] For growth on SrTiO_3 , also the reflection of LaNiO_3 is clearly visible and fully strained with

the substrate. In contrast to the growth of NaNbO_3 , no additional reflections or orientation changes are observed for AgNbO_3 up to a thickness of 150 nm with $\pm \sim 0.5\%$ strain. NaNbO_3 on the other hand showed relaxation or orientation changes already at lower thicknesses. This indicates that the AgNbO_3 growth is more stable towards relaxation.

6.3.2 AFE versus FE Structure

Due to the structural similarity of AgNbO_3 and NaNbO_3 , the difference between the AFE and FE structures of AgNbO_3 can be evaluated based on the unit cell multiplicity as well. The antipolar shifts of the cations lead to an enlarged AFE unit cell compared to the FE unit cell, which allows differentiation via scattering techniques. [62, 71]

The RSMs shown in Figure 6.3.1 include measurements of the areas for the expected superlattice peaks of the films grown on SrTiO_3 , DyScO_3 and GdScO_3 . Based on these graphs, a superlattice peak is evident only in the in-plane direction, $\frac{3}{4}03$, for AgNbO_3 grown under compressive strain, on SrTiO_3 . However, when AgNbO_3 is grown on the other two substrates, intensities neither for in-plane nor for out-of-plane superlattice reflections can be detected. Thus, AgNbO_3 grown under compressive strain appears to feature an AFE phase, while tensile strain inhibits the formation of this phase. This coincides well with the results from the analysis of the strain impact on the AFE phase formation of NaNbO_3 . The same trend for the stabilisation of the AFE phase is detected for both perovskites. Due to the chemical similarity of AgNbO_3 and NaNbO_3 , the previous discussion about the origin of the superlattice reflections holds for AgNbO_3 as well. Only the different behaviour of the films grown under small tensile strain is unexpected. While for bulk materials, the AFE phase of AgNbO_3 is stable as compared to NaNbO_3 , the epitaxial growth results in destabilisation of this phase already at low strains, where the ground state of NaNbO_3 thin films grown under small strains still features the superlattice reflection.

Furthermore, the direction of the fourfold lattice parameter coincides with the expected direction based on the bulk lattice parameters for AgNbO_3 as well. For bulk materials, it is parallel to the a lattice parameter in Table 5.3.3. Given that the lattice parameter of SrTiO_3 is smaller than that of AgNbO_3 , the orientation of the lattice parameter a in the in-plane direction helps minimise overall strain, which is the observed case. Therefore, not only the trend of the strain impact on phase formation, but also the similarity to the bulk structure remain for AgNbO_3 . Thus, these results might apply to other AFE perovskites as well and could represent a general relation between the strain and AFE stability.

Sakurai *et al.* [110] and Zhang *et al.* [28] observed AFE behaviour for AgNbO_3 films grown on $\text{SrTiO}_3(100)$ substrates, similar to the structural results presented so far. This is evaluated based on electrical characterisation for the publications, and a double hysteresis loop is recorded. Thus, the AFE structure on AgNbO_3 thin films under compressive stress

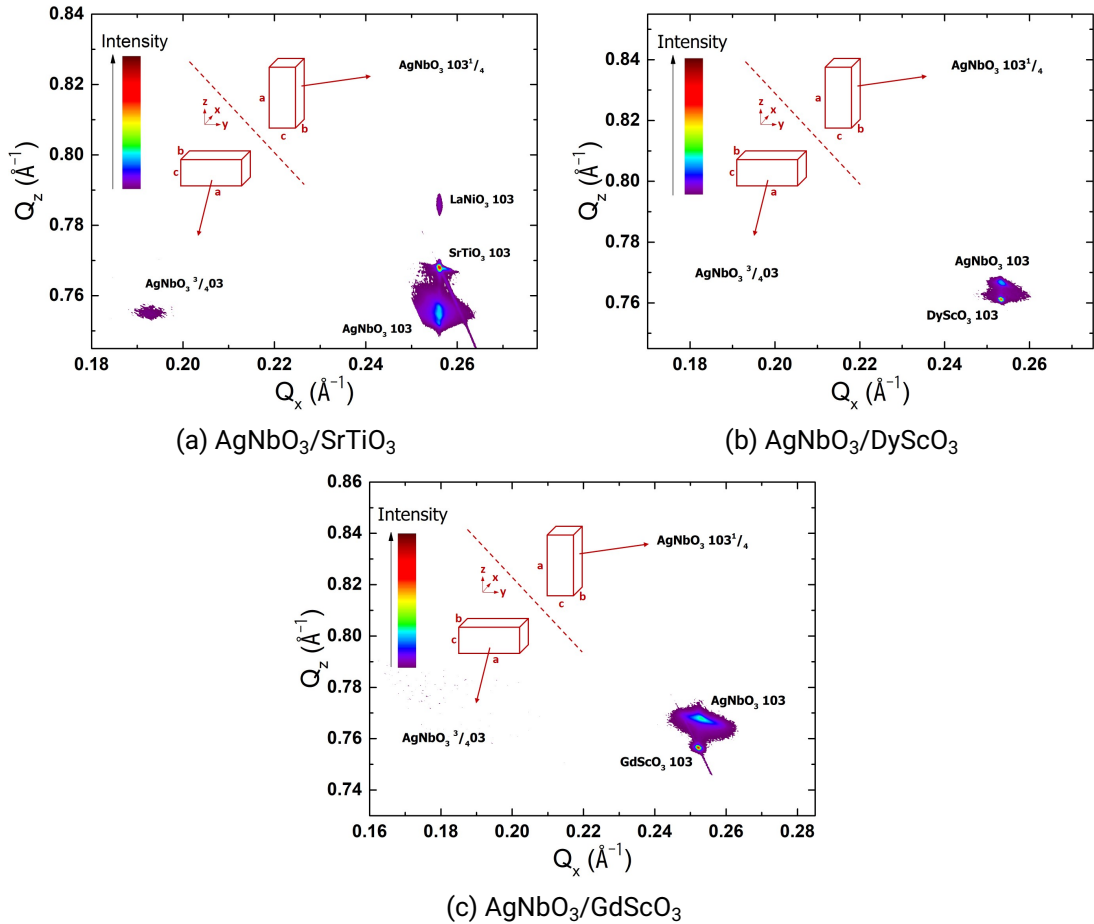


Figure 6.3.1: RSMs of AgNbO_3 thin films around the 103 substrate reflection on different substrates. Additionally, the areas for the superlattice peak in in-plane, $3/4$ 03, and out-of-plane direction, $103^{3/4}$, are shown. The direction of the fourfold axis for the corresponding superlattice peak is indicated via the added schematic.[155]

appears to be sufficiently stable to result in a reversible phase transition. Meanwhile no literature exist for AgNbO₃ thin films grown under tensile strain, making a comparison of the obtained results for growth on DyScO₃ and GdScO₃ impossible.

6.4 Conclusion

This chapter concludes with an in-depth analysis of the structural properties of NaNbO₃ and AgNbO₃ thin films. For both materials, fully strained thin films are obtained utilising the growth conditions which have been optimised in the previous chapter. The critical thickness of relaxation is determined for NaNbO₃, with the exception for the growth on SrTiO₃, where a stress relief mechanism is observed rather than a relaxation. AgNbO₃ films are found to be stable against relaxation up to a thickness of 150 nm on the substrates SrTiO₃, DyScO₃ and GdScO₃.

The ground state is further characterised via the presence of $\frac{1}{4}$ superlattice reflections in the RSMs, characteristic for the AFE structure of both materials. It should be noted, that due to the epitaxy a difference to the bulk structure is inevitable, as the in-plane lattice parameters are locked to the ones from the respective substrate. For growth on the cubic substrates LSAT and SrTiO₃, this leads to a cubic base of the perovskite cell, which is not present for the bulk structure. However, the superlattice reflections remain indicative of an antipolar ion displacement, as other influences can be effectively excluded. Rotation and tilting of the oxygen octahedra can lead to superstructures in perovskites, however, due to the low scattering contrast of X-ray on oxygen species, no superlattice reflections should be detectable with the low thicknesses of thin films. Other ordering phenomena can be excluded as cation ordering by antisite defects is unlikely due to the large size and charge difference between the A-site and B-site cations for these materials.[169] This is further validated by HRTEM results of NaNbO₃ grown on SrTiO₃, which reveal similar modulation structures to bulk AFE NaNbO₃. [173]

The main findings are summarised in regards to the initial questions in the introduction of this chapter:

- 1. What is the stability range of epitaxial thin films of NaNbO₃ and AgNbO₃ on different substrates until a relaxation occurs?**

For NaNbO₃, the critical thickness upon which the films relax to the bulk structure is dependent on the chosen substrate. This critical thickness is found to be significantly higher for growth of compressively strained films on LSAT at ~200 nm than for films grown under tensile strain, on DyScO₃ at ~90 nm, although the magnitude of the strain is similar, see Table 5.2.3. The cause of this difference can be due

to the increased defect concentration for growth on DyScO₃, which causes the observed enlarged out-of-plane lattice parameter as well, see Figure 6.2.1c. The behaviour of the growth of NaNbO₃ on GdScO₃ is similar to that on DyScO₃, with a further reduction of the critical thickness to ~50 nm due to the increase of the lattice mismatch. Only for NaNbO₃ thin films grown on SrTiO₃, no critical thickness is found up to 310 nm thick films. This is caused by a combination of the low lattice parameter mismatch and a strain relief mechanism, where the NaNbO₃ changes the growth orientation. Due to the unique lattice parameter combination, this results in a change from growth under tensile strain to compressive strain and, thus, minimises the strain energy in the film. This orientation change happens at a thickness of ~100 nm.

For the growth of AgNbO₃, no relaxation is detected on the three chosen substrates up to a thickness of 150 nm. However, a broadening of the AgNbO₃ reflection in the RSM for the growth on GdScO₃ is observed, indicative of an increased mosaicity. For all films, the epitaxial relation to the substrate is kept during growth, despite the interfacial Ag compensation layer, which amounts to a thickness of 60 nm for growth of 150 nm thick AgNbO₃ films on LaNiO₃/SrTiO₃.

2. Can epitaxial growth be employed to stabilise the AFE phase or does it favour the formation of a FE phase?

NaNbO₃ thin films are found to exhibit a ground state which resembles the bulk AFE phase for low epitaxial strain, grown on SrTiO₃. This is characterised by the presence of a fourfold superlattice structure, which is exclusive to the AFE phase. Further, even the direction in which this fourfold structure is oriented matches with the lattice parameters of the bulk AFE structure. For the case of NaNbO₃, this has not been observed before, with literature describing a stabilisation of the FE phase due to the epitaxial strain.[100, 29]

For AgNbO₃, on the other hand, when grown with small epitaxial strain on DyScO₃, no presence of a superlattice reflection can be detected. This indicates, that in this case the thin film growth indeed favours the FE or a completely different phase over the AFE phase.

The difference between the behaviour of NaNbO₃ and AgNbO₃ is surprising, given the energy difference between the AFE and FE phases is larger for AgNbO₃ than for NaNbO₃. NaNbO₃ should be very sensitive to even the smallest changes on the energy levels of the AFE and FE phases, indicating that the epitaxial growth either stabilises the AFE phase or has a negligible impact. The results of AgNbO₃ reveal the opposite, with the observation of an apparent destabilisation of the AFE phase. As the epitaxial strains for this comparison of NaNbO₃ and AgNbO₃ thin films are not

identical, this variation could explain the measured behaviour, which is discussed in the context of the following question.

3. What is the impact of different magnitudes of strain on the phase balance? Do different levels of strain stabilise different phases or does epitaxial growth favour only one phase?

The strain is found to change the ground state of the films. Both materials reveal a similar trend, with the presence of the superlattice reflections for compressively strained films. Meanwhile they are not observed for thin films grown under tensile strain, indicating the change from an AFE phase to a different phase, possibly the FE phase. The stability region of the AFE phase is different for NaNbO_3 and AgNbO_3 , with NaNbO_3 featuring the AFE phase for growth under a tensile strain of -0.18% while AgNbO_3 shows no indication of its AFE phase for growth under tensile strain of -0.05% . Therefore, while the trend is similar for both materials, the impact of thin film growth on the energetic balance of the AFE and FE phases is different. The origin of this behaviour might be related to the growth conditions on different substrates: Both materials show the superlattice reflections for growth on cubic substrates, LSAT and SrTiO_3 , while growth on the orthorhombic scandates DyScO_3 and GdScO_3 leads to no superlattice reflections. Due to the orthorhombic nature of NaNbO_3 and AgNbO_3 , however, the strain incorporation can be anisotropic for both cases. This anisotropy has been shown to influence the domain formation for FE thin films,[23], but due to the small changes between the substrates, no impact on the phase balance of AFE materials is expected. Further investigation in this regard can be conducted via growth on NdGaO_3 , which is another orthorhombic perovskite and features a smaller lattice parameter than NaNbO_3 and AgNbO_3 , allowing to induce compressive epitaxial strain. Beyond this argument, the involved surface energies could be relevant for the formation of the individual phases. This has not been considered so far and, hence, further investigation is necessary to validate this hypothesis. Confirmation of this assumption can be provided by computational investigation into the relevant surface energies and their consequences.

The observed trend of phase balance in dependence on the induced strain has not been detected in literature so far. For NaNbO_3 , all thin film studies reveal FE behaviour, however, as mentioned before, this can be ascribed to the metastability of the FE phase of NaNbO_3 after application of an electric field. For AgNbO_3 , previous studies have already detected the presence of an AFE behaviour, exclusively for compressively strained films grown on $\text{SrTiO}_3(100)$. [28, 110] This matches the observed trend of the AFE phase stabilisation with compressive strain, which is also found in theoretic works.[108] The assumption concerning the phase balance of

AFE materials based on theoretical works so far is a stabilisation with increasing tensile strain,[106, 100] which is in contrast to the results presented here. This discrepancy between the computational and experimental results highlights the complexity of the AFE effect and the limited understanding of the relevant factors so far. Hence, the results obtained in the present study promise further improvement of the computation models on AFE materials and their predictions.

7 Electrical Characterisation

7.1 Motivation

In the previous chapter, the general trend of the phase stability in dependence on the induced strain has been evaluated. However, the obtained information serves only to differentiate whether the bulk like AFE state is retained with introduction of the epitaxial strain or whether another phase is stabilised instead. Electrical characterisation of the polarisation response of the films allows to investigate whether the thin films exhibit a FE phase which can be stabilised by application of an electric field, confirming that the material is indeed AFE. Further, it allows to identify whether strain can lead to a stabilisation of the AFE phase. In bulk ceramics of NaNbO_3 the P-E behaviour shows a FE hysteresis, thus, in case of a stabilisation of the AFE phase with the epitaxial strain, a double-hysteresis loop would become visible. The magnitude of the switching field from the AFE to the FE phase serves then as a measure of the stabilisation.

To access these electrical properties of the materials, parasitic currents through the films have to be inhibited such that the polarisation response can be characterised. These leakage currents are often problematic for thin films and can be caused by a multitude of origins, see Section 3.2.3. For the AgNbO_3 thin films synthesised in this thesis, these currents are too large to achieve electrical characterisation and are not further discussed in this section.

Thus, this chapter is concerned with the following questions:

1. **What are the leakage current properties of NaNbO_3 thin films? How can they be improved to facilitate measurement of the P-E behaviour?**
2. **What is the impact of the strain on the P-E behaviour? Can the AFE phase be stabilised by strain?**
3. **How can strain engineering be utilised to improve the properties of AFE materials?**

7.2 Leakage Current Reduction

Initial measurements show a significant amount of leakage current, see Figure 7.2.1, which is suspected to be caused by oxygen vacancies.[174, 175, 176] This idea is supported by the peak shifts observed in the XRD measurements, see Section 6.2.1. To confirm this hypothesis, NaNbO₃ thin films are grown on SrTiO₃(100) under the same conditions and with the same thickness and subjected to heat treatments under different oxygen pressures ranging from 10 mbar to 350 mbar, at a fixed temperature of 400 °C for 1 h. Figure 7.2.1 shows the resulting current by application of an increasing voltage.

A clear decrease in leakage current with increasing oxygen pressure during the heat treatment can be observed. While annealing at low oxygen pressures results in an increase in leakage compared to the as-grown sample, larger oxygen pressures successively decrease the observed current at a given voltage. The initial increase can be attributed to the formation of additional oxygen vacancies or sodium loss caused by the combination of low pressure and elevated temperature. From the shape of the leakage current, the impact of annealing on the leakage mechanism can be hypothesised: For the as-grown film as well as the film annealed under 10 mbar of oxygen pressure, symmetrical curves are obtained, indicative of a bulk-limited conduction mechanism. Meanwhile the thin films annealed under higher oxygen pressure show a different behaviour for positive and negative fields, which serves as an indicator of electrode-limited conduction mechanisms, as the electrode materials for the top and bottom contact differ. This leads to different barrier heights, and, hence, different behaviour of the charge injection.[136]

For a more in-depth look at the mechanisms behind the leakage, the data is fitted to possible leakage mechanisms of thin films. The considered conduction mechanisms include Ohmic conduction, space charge limited current (SCLC), Poole-Frenkel conduction, and Schottky conduction. To distinguish between Poole-Frenkel and Schottky conduction, the optical permittivity ϵ_{Op} is determined from the slopes of the corresponding fits. Although ϵ_{Op} values have not been measured for NaNbO₃ thin films, an estimation based on the refractive index n which is around 2.2 – 2.5 for common perovskite compounds[177] can be made. As $\sqrt{\epsilon_{Op}} = n$, ϵ_{Op} should be in the range of approximately 4.8 – 6.3.

For both the as-grown film and the film annealed with 10 mbar of oxygen pressure, only the fitting corresponding to Ohmic conduction is performed, as it matches the mechanism over the entire range, see Figure 7.2.2a and b. In both cases, the films exhibit a consistent slope over the range of applied electric fields, indicating that Ohmic conduction due to free charge carriers dominates. Deviations at low fields are attributed to measurement errors at low currents. Analysis of the thin films annealed at 100 mbar and 350 mbar of oxygen pressure reveals the presence of Ohmic conduction at low fields as well. However, the magnitude of this current changes significantly due to the heat treatment: For annealing under a low

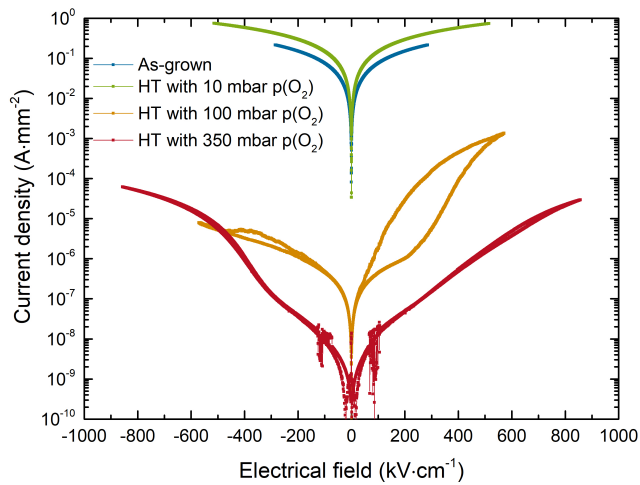


Figure 7.2.1: Leakage current depending on the applied field for heat treated NaNbO_3 thin films as well as one as-grown sample for comparison. Reprinted with permission.[160]

oxygen pressure of 10 mbar, the current density is increased, which is indicative of more free charge carriers contributing to the current. If the oxygen pressure during annealing is increased to 100 mbar and 350 mbar, the magnitude of the current density is significantly reduced. Thus, the oxygen pressure has a significant impact on the free charge carrier density. Therefore, the high leakage current in untreated films can be attributed to the presence of oxygen vacancies, which may have been caused by intermixing of the Na and Nb cations during film growth, a phenomenon observed in similar perovskites.[178]

A change to a different mechanism can be observed by a change of slope in the double-logarithmic plots for the films annealed at an oxygen pressure of 100 mbar and 350 mbar. This transition occurs at around $200 \text{ kV} \cdot \text{cm}^{-1}$, with slight variation for positive and negative bias.

In the case of the thin film annealed with 100 mbar of oxygen pressure, a clear change of slope is noticeable at fields of approximately $-100 \text{ kV} \cdot \text{cm}^{-1}$ and $220 \text{ kV} \cdot \text{cm}^{-1}$. For the negative polarity, the slope increases slightly, indicating the presence of SCLC, while for the positive side, a much larger increase of the slope becomes visible. The fitting results from the Schottky and Poole-Frenkel mechanisms, see Figure 7.2.2c-f, clearly demonstrate the absence of these mechanisms in the negative direction, as the calculated ϵ_{Op} is far from the theoretical value. However, at high positive fields, the slope of the linear fit for

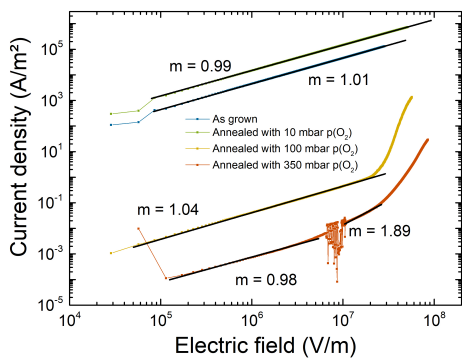
the Poole-Frenkel mechanism results in an optical permittivity of 5.02, which falls within the expected range. Therefore, it can be assumed that this mechanism plays a role in the conductivity at large positive fields, possibly due to states in the band gap resulting from oxygen vacancies.[136]

Similarly, the film annealed with 350 mbar of oxygen pressure shows a transition from Ohmic behaviour to another mechanism at larger electric fields. In both polarities, SCLC behaviour is initially visible at intermediate fields, as indicated in the double-logarithmic plots by a slope close to 2, followed by another transition marked by a further increase in slope. For the negative polarity, neither Schottky nor Poole-Frenkel fitting yields a good fit. However, the shape resembles a transition from a trap-filled limit to Child's law.[136] To validate this hypothesis, data points at larger fields would be necessary to reveal the slope of 2 in the double logarithmic plot. For the case of positive polarity, on the other hand, the slope of the Schottky fitting shows an optical permittivity in the expected range after the transition from SCLC at approximately $270 \text{ kV} \cdot \text{cm}^{-1}$. Due to the difference of the electrode material, the Schottky injection is only present in one direction, indicating a lower barrier height for the application of a negative bias to the sample. With the utilised configuration, this corresponds to an electron injection from the top contact or hole injection from the bottom electrode into the sample.

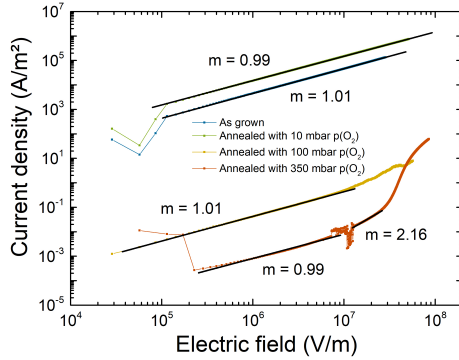
Thus, heat treatment under high oxygen pressure is effective at reducing the number of internal defects in the films. This transforms the conduction mechanism from bulk-controlled to electrode-controlled, which goes along with a significant reduction of the magnitude of the leakage current. With the low leakage achieved for the film annealed under 350 mbar of oxygen pressure, further electrical characterisation can be achieved. Structural characterisation of the samples before and after heat treatment showed no change in crystal structure or strain state, see Figure S6 and Figure S7.

7.3 Polarisation versus Electric Field Behaviour

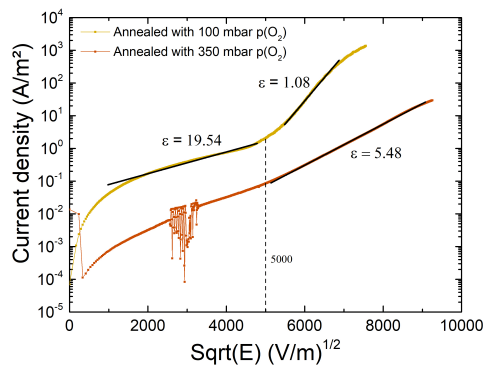
Following the reduction in leakage current due to heat treatment, further electrical characterisation of the samples is enabled. Since the polarisation vector for the bulk ground state is perpendicular to the a_{PC} lattice parameter and corresponds to the $[011]_{PC}$ direction,[13] measuring the out-of-plane contribution with the parallel plate capacitor setup allows access to a portion of the polarisation for epitaxial growth on the selected substrates. To supplement the information about the phase balance obtained from XRD, the polarisation versus electric field behaviour is measured and shown in Figure 7.3.1. For each substrate, the curves represent films with the lowest leakage current. While the trends for all films on a given substrate resemble the shown graphs, the contribution of



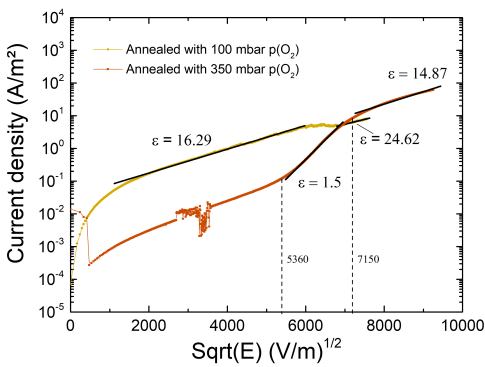
(a) Ohm fitting, positive



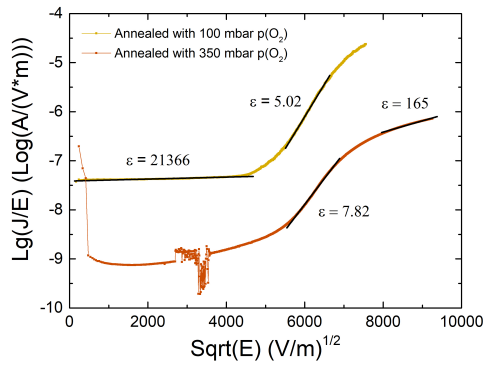
(b) Ohm fitting, negative



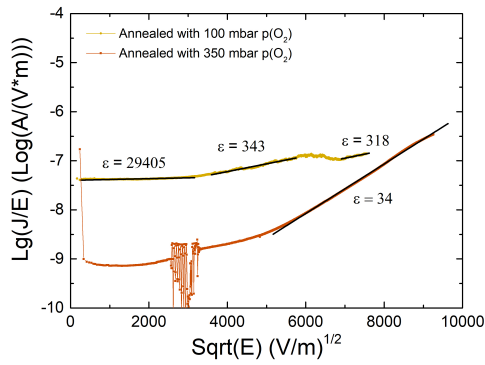
(c) Schottky fitting, positive



(d) Schottky fitting, negative



(e) Poole-Frenkel fitting, positive



(f) Poole-Frenkel fitting, negative

Figure 7.2.2: Fitting of the leakage current from the as grown sample as well as the annealed samples. For all graphs, segments are fitted by a linear fit. For the double-logarithmic plots, the slope of the respective fit is given, while for the other graphs the optical permittivity calculated from the slope is given. Reprinted with permission.[160]

leakage current leads to curves which are more difficult to analyse.

The NaNbO_3 thin films exhibit different electrical behaviour depending on the type of epitaxial strain. When grown on LSAT under compressive strain, as seen in Figure 7.3.1a, the film displays a strong out-of-plane polarisation component, with a saturation polarisation of up to $55 \mu\text{C} \cdot \text{cm}^{-2}$. While the shape of the P-E hysteresis resembles a FE hysteresis, it is different from the ideal shape of such a hysteresis. This difference results from multiple peaks in the plot of the current density versus electric field, which would feature one peak for each field direction for a FE material and two for a AFE material. These multiple peaks render the dielectric behaviour unclear. It should be noted, that repeated measurements lead to slight differences in the shape of the obtained hysteresis curve. From the structural characterisation, the films are found to exhibit complex domain ordering, which can contribute to the observed behaviour. Further, the identified presence of defects can lead to pinning centres, locally affecting switching fields and, thus, leading to multiple current peaks.

For growth on SrTiO_3 , no polarisation contribution is visible up to the thickest film, as shown in Figure 7.3.1b. The latter exhibits bulk-like properties with a saturation polarisation of $26.5 \mu\text{C} \cdot \text{cm}^{-2}$. This represents one of the highest values ever reported for NaNbO_3 grown on $\text{SrTiO}_3(100)$ substrates.[104, 29] However, it is important to consider that these literature reports are derived from thick films with thicknesses of several μm . Thus, similar to bulk ceramics of NaNbO_3 , these thin films undergo an irreversible transition to the FE phase due to a small energy difference between the two phases.

Meanwhile for the thinner films, the transition from the antipolar phase to a FE phase is not achieved for fields up to $600 \text{ kV} \cdot \text{cm}^{-1}$. This is indicative of the applied electric field being insufficient to lead to the transition. Due to the changed symmetry of the thin films because of the epitaxy, it can be possible that no suitable FE phase exists, leading to the observed behaviour. However, as the thicker film grown on SrTiO_3 shows FE behaviour, this theory can be dismissed. Thus, this reveals that the epitaxy enhances the switching field for thin NaNbO_3 films on $\text{SrTiO}_3(100)$. However, as the strain affects not only the phase balance, a stabilisation of the AFE phase by the epitaxy cannot be concluded. As the transition from the AFE to the FE phase is accompanied by a strain increase in the material,[24] it is possible, that the epitaxy renders only the phase transition unfavourable. Once the material would achieve this transition, however, the FE phase can remain metastable as for bulk ceramics of NaNbO_3 . To clearly evaluate an increased stability of the AFE phase, a reversible double-hysteresis loops needs to be visible. Notably, when comparing the two different thicknesses shown in Figure 7.3.1b for NaNbO_3 , the thicker film exhibits contributions from two different orientations, while the thinner film only possesses one orientation, with the b/c lattice parameter in the out-of-plane direction. However, looking at the direction of the polarisation vector for both orientations, only one of them should

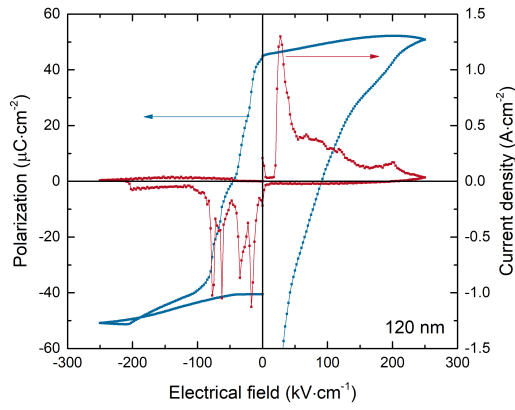
be able to contribute to an out-of-plane polarisation component: For the bulk AFE phase, the polarisation vector is perpendicular to the a_{PC} lattice parameter. Hence, when this parameter grows in the out-of-plane direction, the ion displacements and the polarisation vector should lie fully in-plane. Assuming this is the case, for the thicker film, simply the increased volume fraction of the b/c -orientation might be sufficient to overcome the epitaxial boundary and switch to the FE phase, while the a -orientation does not contribute to the polarisation at all.

For the case of NaNbO_3 grown on DyScO_3 and GdScO_3 under tensile strain, only a linear behaviour is observed in the P-E measurement until the leakage current contributes at higher applied voltages, see Figure 7.3.1c and d. Since the structural analysis reveals no antipolar displacements for this case, the stabilisation of such a phase can be excluded for these films. Therefore, the most likely explanation is the formation of a different structure for the growth on these substrates or that the polarisation direction is rotated fully in-plane due to the tensile strain. The latter results in a linear behaviour, as the parallel-plate electrode setup only measures the out-of-plane contribution. To clearly differentiate these two cases, in-plane measurements are necessary.

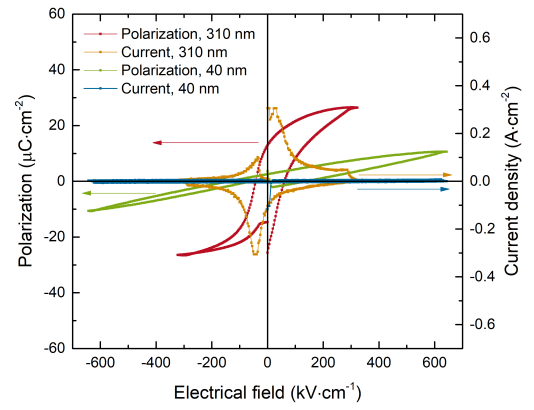
7.4 Conclusion

This chapter concludes the electrical measurements of the NaNbO_3 thin films. The as-grown films suffer from severe leakage currents, rendering the characterisation of the P-E behaviour impossible. The origin of this current is found to be free charge carriers in the films due to oxygen vacancies. By annealing at a high oxygen pressure of 350 mbar, these vacancies are successfully minimised, leading to a change from Ohmic conduction to SCLC for large negative bias and Schottky injection for large positive bias. At lower fields, the annealed film still exhibits Ohmic conduction, however, with a significantly reduced magnitude due to the reduction of free charge carriers.

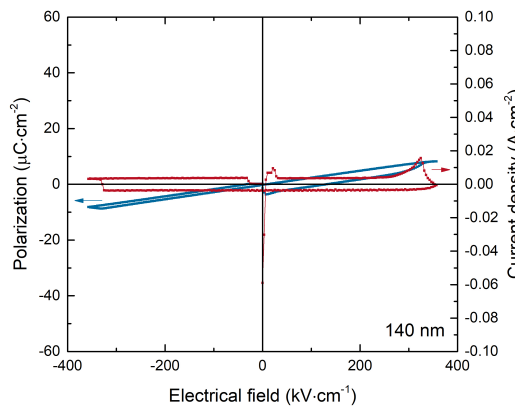
From the electrical characterisation of the NaNbO_3 thin films, no stabilisation of the AFE phase with strain can be recognised. For the thin films which have previously been characterised to possess an AFE ground state, FE behaviour is observed in the P-E curves. An exception are films thinner than 310 nm grown on SrTiO_3 . These show a linear behaviour and no switching to the FE phase up to an applied field of $600 \text{ kV} \cdot \text{cm}^{-1}$. This indicates a stabilisation of the AFE state for these films or an inhibition of the transition due to the epitaxy. Considering the constraint from the epitaxy, that two lattice parameters as well as their angle needs to remain constant through the phase transition, it might be impossible to transform the AFE phase to the FE phase while keeping this condition intact. Thus, the switching to the FE phase might necessitate a relaxation from the strained state,



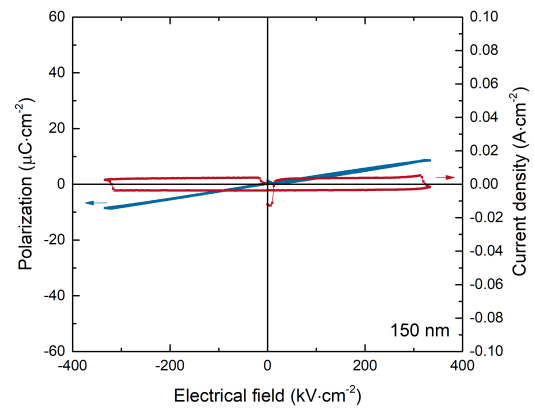
(a) $\text{NaNbO}_3/\text{LaNiO}_3/\text{LSAT}$



(b) $\text{NaNbO}_3/\text{LaNiO}_3/\text{SrTiO}_3$



(c) $\text{NaNbO}_3/\text{LaNiO}_3/\text{DyScO}_3$



(d) $\text{NaNbO}_3/\text{LaNiO}_3/\text{GdScO}_3$

Figure 7.3.1: Polarisation (left axis) and current density (right axis) versus electric field curves for NaNbO_3 thin films on different substrates. The samples shown feature the lowest leakage current and represent the general behaviour on the respective substrate. Reprinted with permission.[160]

which can be facilitated by the energy of the electric field. With this assumption, the difference between thin and thicker films of NaNbO₃ on SrTiO₃ can be well explained: with increasing thickness, the total strain energy is already increased, while the energy supplied by the electric field similarly increases due to the increased volume of the NaNbO₃ film. Thus, this energy is sufficient to lead to a local relaxation and switch the material to the bulk FE phase. In order to test this hypothesis, however, local measurements of the epitaxial relation before and after the application of the electric field would be necessary. The magnitude of the polarisation response of the FE phase in NaNbO₃ thin films is also affected by the introduced strain. The measured saturation polarisation for the films on LSAT is more than twice as large as the saturation polarisation observed for growth on SrTiO₃, confirming the effect of compressive strain on the polarisation.[106, 24] The measured saturation polarisation is also larger than the highest values measured for NaNbO₃ bulk materials of $\sim 40 \mu\text{C} \cdot \text{cm}^{-2}$. [15] It should be noted that the thickness of the films impacts their dielectric properties, affecting the comparison between films on different substrates. However, due to the dead layer effect, thicker films tend to have higher permittivity and polarisation values, and so the increase in the magnitude of the saturation polarisation is not negatively affected by this effect.[179]

To summarise the findings of this chapter, the initial questions for this study are answered:

1. What are the leakage current properties of NaNbO₃ thin films? How can they be improved to facilitate measurement of the P-E behaviour?

As-grown thin films are found to exhibit large leakage currents, mediated by free charge carriers in the films. The resulting Ohmic conduction exceeds currents created by the polarisation response of the films and renders the P-E measurement impossible. The number of mobile charges in the films can be affected by annealing in oxygen atmosphere. While a low oxygen pressure is shown to increase the magnitude of the current further, annealing under higher oxygen pressure reduces the current density by several magnitudes. Thus, the origin of the leakage stems partially from oxygen vacancies supplying the mobile charges in the films.

2. What is the impact of the strain on the P-E behaviour? Can the AFE phase be stabilised by strain?

The electrical characterisation does not clearly reveal a stabilisation of the AFE phase with epitaxial strain. Only thin films below 310 nm on SrTiO₃(100) show no transition from the antipolar state to a FE phase. To clarify whether the phase balance or only the transition is affected by the strain, however, a sufficiently high field such that a reversible transition becomes visible needs to be applied. For the present films, however, at higher fields, the leakage current contribution becomes too large. The other films which have been found to retain the bulk-like AFE ground

state in the structural characterisation show a FE like hysteresis in the electrical characterisation. This indicates a small energy difference and, hence, no additional stabilisation of the AFE phase compared to bulk ceramics of NaNbO_3 .

3. How can strain engineering be utilised to improve the properties of AFE materials?

While the strain engineering does not show an improved stabilisation of the AFE phase in the investigated strain range, films grown under compressive strain on LSAT reveal an increased saturation polarisation. This polarisation is more than two times as large as for the case of small strain for growth on SrTiO_3 . Concerning the energy density of AFE materials, the magnitude of the saturation polarisation plays a significant role. As compressively strained films retain the AFE ground state, the phase balance appears similar to bulk ceramics. Thus, the impact of doping materials is expected to be similar, which is already heavily investigated for NaNbO_3 bulk ceramics. Combination of doping to stabilise the double-hysteresis loop with the introduction of compressive strain is promising to lead to increased energy densities for AFE materials.

8 Final Conclusion & Outlook

This work concludes with the critical influences on thin film growth of the AFE perovskites NaNbO_3 and AgNbO_3 . Both show a tendency towards non-stoichiometric material transfer in the PLD process, which has to be overcome to achieve phase-pure thin films. Further, the impact of strain engineering to improve AFE properties has been investigated via epitaxially strained films with different strain states. A relation between the formed crystal structure of both materials in dependence on the strain level is uncovered via structural characterisation. Further, in combination with the electrical characterisation, a trend towards higher energy densities for AFE capacitors is formulated.

Summary of the Results

Thin film growth: In the first step, the film growth of both materials has been investigated in depth to achieve phase pure, stoichiometric thin films with high crystalline quality. For the growth of both NaNbO_3 and AgNbO_3 films via PLD, an off-stoichiometric material transfer is observed which has to be overcome to achieve the desired phase.

For NaNbO_3 thin film growth, the difficulty is the incorporation of Na during the film growth, resulting in a deficiency of this A-cation in the thin film. The Na loss, which is also observed for the synthesis of bulk ceramics,[109] can be related to the high volatility of Na at elevated temperatures. An increase of the background pressure can suppress the desorption of this species from the substrate during film growth, and stoichiometric NaNbO_3 thin films are achieved at an oxygen background pressure of 0.53 mbar. After modification of the relevant PLD parameters, thin films with high crystalline quality are achieved, which are shown to grow epitaxially strained on LSAT, SrTiO_3 , DyScO_3 as well as GdScO_3 .

For AgNbO_3 thin film growth, similarly the problems in the stoichiometric transfer can be traced to a deficiency of the A-cation, in this case silver. However, unlike for the growth of NaNbO_3 , the source of the silver loss in the process is not clearly identified and compensation via growth parameter optimisation has proven difficult. Hence, an

external method for the compensation is developed, based on the high mobility of silver ions at elevated temperatures. For this method, a thin layer of silver is sputtered on the substrate before the deposition, which serves as a silver reservoir during growth and fills the vacancies created by the off-stoichiometric material transfer. This method results in stoichiometric, phase-pure AgNbO_3 thin films of high crystalline quality. Further, this method is examined in regards to growth on different substrates and different AgNbO_3 film thicknesses. The transfer to other substrates necessitates a calibration of the thickness of the Ag compensation layer, upon which epitaxially strained films are obtained up to a thickness of 150 nm on the substrates SrTiO_3 , DyScO_3 and GdScO_3 .

Structural characterisation: In literature, no clear consensus can be found concerning the dielectric nature of NaNbO_3 and AgNbO_3 thin films, lacking an investigation of the properties in dependence on the epitaxial strain. Thus, both materials are characterised regarding the formed crystal structure via XRD and HRTEM. For the determination of the ground state, the crystal structure of the thin films is related to the phases of the respective bulk materials. The characteristic difference between the AFE and FE phases of both materials can be found in the size of the unit cell, which is twice as large for the AFE phase due to the antipolar displacement of the cations.[14]

For NaNbO_3 the presence of the resulting superlattice reflections is detected for films grown under compressive strain on LSAT as well as under small tensile strain on SrTiO_3 . The crystal structure of these thin films shows a close correlation to the structure of the bulk AFE phase, as the direction of these superlattice reflections coincides with the expected direction based on the lattice parameters of bulk NaNbO_3 . For growth on SrTiO_3 , the direction of the cell quadrupling changes from in-plane to out-of-plane with increasing thickness. This results in a compensation of the strain in the films, as the lattice parameter combination between NaNbO_3 and SrTiO_3 allows the material to change from tensile to compressively strained growth by this orientation change. This in turn minimises the total strain energy in the films and the strained state is preserved up to larger thicknesses. For growth under compressive strain, on DyScO_3 and GdScO_3 , on the other hand, no indication of an AFE phase can be detected. This is observed even for relaxed films on these substrates, indicating a destabilisation by the epitaxial growth even beyond the relaxation to the bulk structure.

The AgNbO_3 thin films show the same trend of the ground state, i.e. the presence of an AFE structure under compressive epitaxial strain and no indication of the formation of this phase for tensile strain. However, the behaviour for small tensile strain is different. The AgNbO_3 thin films grown on DyScO_3 under small tensile strain show no indication of an AFE structure, hinting at a destabilisation of this phase already at low strain levels. In comparison with NaNbO_3 , AgNbO_3 features a more stable AFE phase in bulk materials,

due to a larger energy difference between the AFE and the FE phases. Thus, similar to NaNbO_3 , a retention of the AFE phase would be expected, however, the epitaxial strain appears to affect AgNbO_3 differently in this regard.

Electrical characterisation: As the structural investigation is limited to the identification of the ground state, it only serves to analyse whether a bulk-like antipolar structure is formed or destabilised by the epitaxial growth. To characterise, if the epitaxial strain has the potential to stabilise the AFE phase, either structural characterisation parallel to application of an electric field, or measurement of the P-E behaviour is necessary. In the latter case, a stabilisation can be inferred if the switching fields to and from the FE phase are shifted to higher electric fields.

To access the P-E behaviour, the films must be insulating. The as-grown films, however, show a significant leakage current, which renders the P-E characterisation impossible. This leakage current is investigated in-depth for the NaNbO_3 thin films, and the presence of mobile charge carriers leading to Ohmic conduction is detected. These leakage currents in perovskite thin films are often observed due to free charge carriers supplied from oxygen vacancies.[79, 151, 161] Heat treatment in dependence on the applied oxygen pressure reveals a clear correlation confirming this hypothesis and allows to reduce the leakage current by several orders of magnitude through annealing under 350 mbar of oxygen pressure. This leads to a change from Ohmic conduction to an electrode controlled conduction mechanism, revealing the minimisation of intrinsic charge carriers in the NaNbO_3 thin films.

The consecutive analysis of the P-E behaviour reveals no proof of a stabilisation of the AFE phase by the induced epitaxial strain. The NaNbO_3 thin films, which exhibit an antipolar structure show a FE hysteresis behaviour. This resembles the behaviour of bulk NaNbO_3 in which the energy difference between the two phases is sufficiently low such that the FE phase remains meta-stable once the material has switched to this phase. On SrTiO_3 , only the film with 310 nm of NaNbO_3 shows a polarisation contribution, indicating that the switching from the AFE to the FE phase is inhibited by the epitaxy for thinner films. In combination with the fact, that the thicker film with the same structure shows FE behaviour, likely the switching between the two phases is affected and not their energy levels. Possibly a local break of the epitaxial strain state is necessary to induce the switching from the AFE to the FE phase, which can explain the FE behaviour of the thicker film, where the increased interaction volume of the NaNbO_3 with the electric field provides sufficient energy to overcome this constraint. However, further analysis is necessary to draw a conclusion about the interaction between epitaxy and this phase change.

The effect of an increasing compressive strain is manifested in an increase of the saturation polarisation of the FE hysteresis loop. While the NaNbO_3 thin film on SrTiO_3 exhibits a

saturation polarisation of $26.5 \mu\text{C} \cdot \text{cm}^{-2}$, the NaNbO_3 thin film on LSAT displays a value of $55 \mu\text{C} \cdot \text{cm}^{-2}$, which corresponds to an increase of more than 100%. As the saturation polarisation of the FE phase is an important factor for the energy density of AFE capacitors, and these films have been shown to retain the AFE ground state, this presents a promising route to increase the energy density of AFE materials. By suitable doping of the NaNbO_3 thin films, which is deeply explored for bulk ceramics, a further stabilisation of the AFE phase should lead to double-hysteresis loops.

The NaNbO_3 films grown with tensile strain do not reveal any polarisation response to the electric field independent of their thickness and the applied electric field. Since they do not exhibit the AFE ground state, this cannot be explained by a prevention of the phase transition to the FE phase. For this case, it is likely that a rotation of the polarisation vector of the unit cell is responsible for the observed phenomena. Due to the tensile strain, the ions in the perovskite cell have more space to displace in the in-plane direction, resulting in no out-of-plane polarisation.[180, 181, 31] As only the out-of-plane component is probed with the present measurements, no polarisation can be detected. Further in-plane characterisation is necessary to confirm this theory. This rotation and the associated strength of the polarisation vector in dependence on the strain is visualised in Figure 8.0.1.

Outlook

While the investigation of the thin films reveals a clear trend for the formation of the AFE ground state depending on the induced epitaxial strain, much of the atomistic mechanism remains unclear. Especially for the case of NaNbO_3 , computational predictions conclude the contrary behaviour, i.e. a potential stabilisation of the AFE structure with tensile strain.[106, 31] Further, while the trend of the ground state for both NaNbO_3 and AgNbO_3 is similar, the resulting phase for small tensile strain is AFE for NaNbO_3 and FE for AgNbO_3 . As a bulk material, NaNbO_3 features only a small energy difference between the two phases while AgNbO_3 shows a more stable AFE phase. This is reversed for thin films, despite their similarity in regards to the crystal structure.

Whether the AFE phase can be stabilised with the epitaxial strain, however, is not fully answered yet. Since compressively strained films are promising due to the retention of an AFE ground state, the electrical results show no indication of the double-hysteresis loops characteristic for a stable AFE material. This investigation is complicated due to low defect formation energies for both materials,[163] leading to leakage currents and rendering high field investigations impossible. Thus, for further investigations, the thin films need to be further improved and the amount of defects minimised. This can be achieved e.g. by

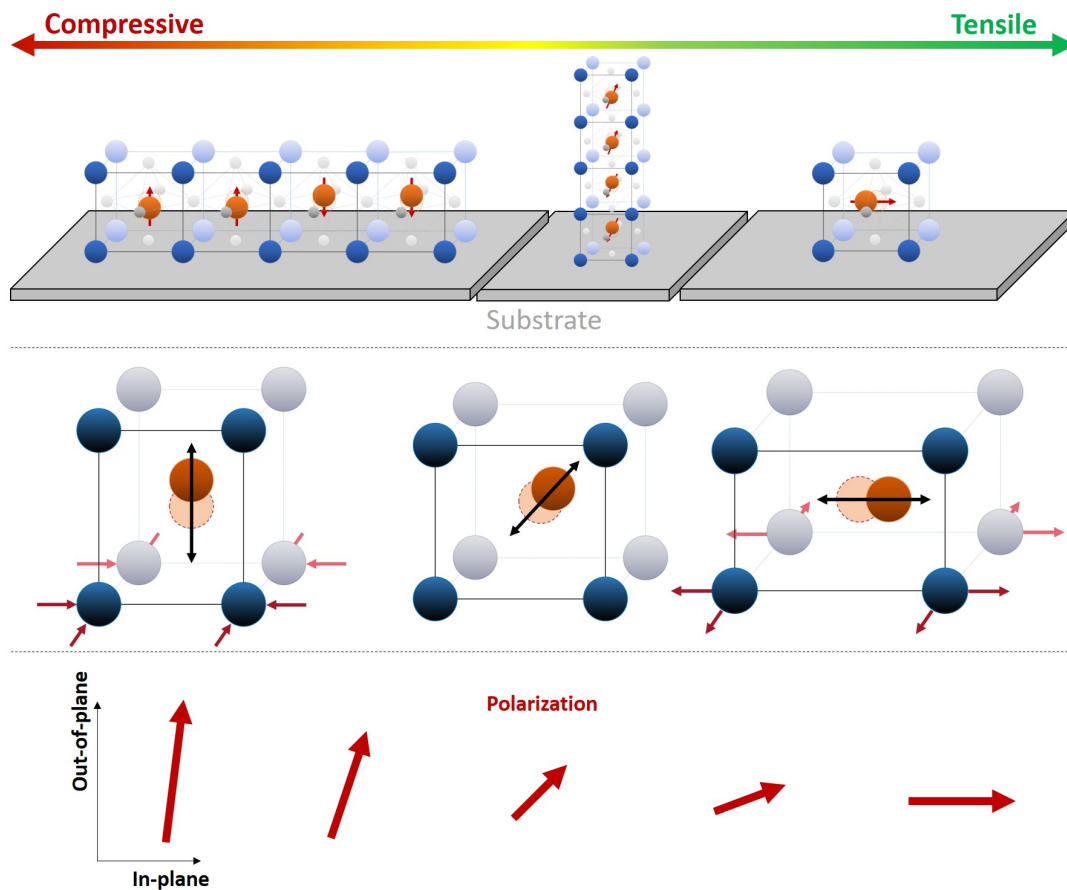


Figure 8.0.1: Simplified model of the results from the structural and electrical results of the NaNbO_3 thin films. *Top*: Growth direction of the fourfold lattice direction based on the XRD results. *Middle*: Direction of the polarisation axis in relation to the perovskite cell. *Bottom*: polarisation direction and magnitude based on the electrical results. Reprinted with permission.[160]

growth via molecular beam epitaxy (MBE). The particle energies of this method are much lower than for PLD, leading to a reduction of defects during film growth. Further, as the cations are supplied via separate sources, a precise control of the film stoichiometry is possible, which has been shown to be critical for the phase formation as well as for the leakage current.

Since the films which feature an AFE ground state show a FE P-E behaviour, the impact of the epitaxy on the AFE stability is difficult to evaluate. Commonly the AFE stability is characterised by the switching fields to and from the FE phase. This analysis also allows to differentiate an increased AFE stability from an inhibition of the phase switching, as for the latter, the mean of both switching fields do not change. Thus, this analysis can only be conducted for materials with a stable AFE phase. Therefore, it is suggested to work with doped NaNbO_3 thin films instead to directly visualise the impact of strain on the phase balance.

Bibliography

- [1] Karin M Rabe, Charles H Ahn, and Jean-Marc Triscone. *Physics of ferroelectrics: a modern perspective*. Vol. 105. Springer Science & Business Media, 2007.
- [2] Clive A Randall et al. “Antiferroelectrics: History, Fundamentals, Crystal Chemistry, Crystal Structures, Size Effects, and Applications”. In: *J. Am. Ceram. Soc.* 104 (2021), pp. 3775–3810. DOI: 10.1111/jace.17834.
- [3] Xihong Hao. “A review on the dielectric materials for high energy-storage application”. In: *Journal of Advanced Dielectrics* 03 (2013). DOI: 10.1142/s2010135x13300016.
- [4] G. Wang et al. “Electroceramics for High-Energy Density Capacitors: Current Status and Future Perspectives”. In: *Chem Rev* 121 (2021), pp. 6124–6172. DOI: 10.1021/acs.chemrev.0c01264.
- [5] Zhen Liu et al. “Antiferroelectrics for Energy Storage Applications: a Review”. In: *Adv. Mater. Technol.* 3 (2018), p. 1800111. DOI: 10.1002/admt.201800111.
- [6] A. Chauhan et al. “Anti-Ferroelectric Ceramics for High Energy Density Capacitors”. In: *Materials (Basel)* 8 (2015), pp. 8009–8031. DOI: 10.3390/ma8125439.
- [7] C. Kittel. “Theory of Antiferroelectric Crystals”. In: *Physical Review* 82 (1951), pp. 729–732. DOI: 10.1103/PhysRev.82.729.
- [8] Xihong Hao et al. “A comprehensive review on the progress of lead zirconate-based antiferroelectric materials”. In: *Progress in Materials Science* 63 (2014), pp. 1–57. DOI: 10.1016/j.pmatsci.2014.01.002.
- [9] Karin M Rabe. “Antiferroelectricity in oxides: A reexamination”. In: *Functional metal oxides: new science and novel applications* (2013), pp. 221–244.
- [10] Malcolm E Lines and Alastair M Glass. *Principles and applications of ferroelectrics and related materials*. Oxford university press, 2001.
- [11] *Ceralink antiferroelectric capacitor by TDK*. <https://www.tdk-electronics.tdk.com/download/1195592/1753c455d19f9c7e635942c9cfba0318/ceralink-presentation.pdf>. Accessed: 2023-11-07.

-
- [12] Kailun Zou et al. “Recent advances in lead-free dielectric materials for energy storage”. In: *Materials Research Bulletin* 113 (2019), pp. 190–201. DOI: 10.1016/j.materresbull.2019.02.002.
- [13] L. E. Cross and B. J. Nicholson. “The optical and electrical properties of single crystals of sodium niobate”. In: *Lond. Edinb. Dublin philos. mag. j. sci.* 46 (1955), pp. 453–466. DOI: 10.1080/14786440508520582.
- [14] Jurij Koruza et al. “Grain-size-induced ferroelectricity in NaNbO_3 ”. In: *Acta Mater.* 126 (2017), pp. 77–85. DOI: 10.1016/j.actamat.2016.12.049.
- [15] Dong Yang et al. “Lead-free antiferroelectric niobates AgNbO_3 and NaNbO_3 for energy storage applications”. In: *J. Mater. Chem. A* 8 (2020), pp. 23724–23737. DOI: 10.1039/d0ta08345c.
- [16] Desheng Fu et al. “ AgNbO_3 : A lead-free material with large polarization and electromechanical response”. In: *Applied Physics Letters* 90 (2007). DOI: 10.1063/1.2751136.
- [17] Lei Zhao et al. “Lead-free AgNbO_3 anti-ferroelectric ceramics with an enhanced energy storage performance using MnO_2 modification”. In: *Journal of Materials Chemistry C* 4 (2016), pp. 8380–8384. DOI: 10.1039/c6tc03289c.
- [18] L. Zhao et al. “Lead-Free Antiferroelectric Silver Niobate Tantalate with High Energy Storage Performance”. In: *Adv Mater* 29 (2017). DOI: 10.1002/adma.201701824.
- [19] Mao-Hua Zhang et al. “Design of Lead-Free Antiferroelectric $(1-x)\text{NaNbO}_3-x\text{SrSnO}_3$ Compositions Guided by First-Principles Calculations”. In: *Chem. Mater.* 33 (2021), pp. 266–274. DOI: 10.1021/acs.chemmater.0c03685.
- [20] Darrell G Schlom et al. “Strain Tuning of Ferroelectric Thin Films”. In: *Annu. Rev. Mater. Res.* 37 (2007), pp. 589–626. DOI: 10.1146/annurev.matsci.37.061206.113016.
- [21] K. J. Choi et al. “Enhancement of Ferroelectricity in Strained BaTiO_3 Thin Films”. In: *Sci.* 306 (2004), pp. 1005–1009. DOI: 10.1126/science.1103218.
- [22] Darrell G Schlom et al. “A Thin Film Approach to Engineering Functionality into Oxides”. In: *J. Am. Ceram. Soc.* 91 (2008), pp. 2429–2454. DOI: 10.1111/j.1551-2916.2008.02556.x.
- [23] J Schwarzkopf et al. “Ferroelectric domain structure of anisotropically strained NaNbO_3 epitaxial thin films”. In: *J. Appl. Phys.* 115 (2014), p. 204105. DOI: 10.1063/1.4876906.

-
- [24] X Tan et al. “Electric-field-induced antiferroelectric to ferroelectric phase transition in mechanically confined $\text{Pb}_{0.99}\text{Nb}_{0.02}[(\text{Zr}_{0.57}\text{Sn}_{0.43})_{0.94}\text{Ti}_{0.06}]_{0.98}\text{O}_3$ ”. In: *Phys. Rev. B* 81 (2010), p. 014103. DOI: 10.1103/PhysRevB.81.014103.
- [25] Claudia Neusel and Gerold A. Schneider. “Size-dependence of the dielectric breakdown strength from nano- to millimeter scale”. In: *J Mech Phys Solids* 63 (2014), pp. 201–213. DOI: 10.1016/j.jmps.2013.09.009.
- [26] Xiaoli Tan et al. “The Antiferroelectric \leftrightarrow Ferroelectric Phase Transition in Lead-Containing and Lead-Free Perovskite Ceramics”. In: *Journal of the American Ceramic Society* 94 (2011), pp. 4091–4107. DOI: 10.1111/j.1551-2916.2011.04917.x.
- [27] Mao-Hua Zhang et al. “Electric-field-induced antiferroelectric to ferroelectric phase transition in polycrystalline NaNbO_3 ”. In: *Acta Mater.* 200 (2020), pp. 127–135. DOI: 10.1016/j.actamat.2020.09.002.
- [28] Yanle Zhang et al. “ AgNbO_3 antiferroelectric film with high energy storage performance”. In: *Journal of Materiomics* 7 (2021), pp. 1294–1300. DOI: 10.1016/j.jmat.2021.02.018.
- [29] Takehisa Saito et al. “Pulsed-Laser Deposition of Ferroelectric NaNbO_3 Thin Films”. In: *Jap. J. Appl. Phys.* 44 (2005), pp. 6969–6972. DOI: 10.1143/jjap.44.6969.
- [30] Yoonho Ahn et al. “Ferroelectric domain of epitaxial AgNbO_3 thin film”. In: *Journal of Crystal Growth* 437 (2016), pp. 10–13. DOI: 10.1016/j.jcrysgr.2015.12.014.
- [31] Oswaldo Diéguez, Karin M Rabe, and David Vanderbilt. “First-principles study of epitaxial strain in perovskites”. In: *Phys. Rev. B* 72 (2005), p. 144101. DOI: 10.1103/PhysRevB.72.144101.
- [32] R. Xu et al. “Size-Induced Ferroelectricity in Antiferroelectric Oxide Membranes”. In: *Adv Mater* 35 (2023), e2210562. DOI: 10.1002/adma.202210562.
- [33] Spartak Gevorgian. *Ferroelectrics in microwave devices, circuits and systems: physics, modeling, fabrication and measurements*. Springer Science & Business Media, 2009.
- [34] F. Jona and G. Shirane. *Ferroelectric Crystals*. Macmillan, 1962.
- [35] Shigeyuki Somiya. *Handbook of advanced ceramics: materials, applications, processing, and properties*. Academic press, 2013.
- [36] Joseph Valasek. “Piezo-electric and allied phenomena in Rochelle salt”. In: *Physical review* 17 (1921), p. 475. DOI: 10.1103/PhysRev.17.475.

-
- [37] Gen Shirane, Etsuro Sawaguchi, and Yutaka Takagi. “Dielectric properties of lead zirconate”. In: *Physical Review* 84 (1951), p. 476.
- [38] E. Sawaguchi, H. Maniwa, and S. Hoshino. “Antiferroelectric Structure of Lead Zirconate”. In: *Physical Review* 83 (1951), pp. 1078–1078. DOI: 10.1103/PhysRev.83.1078.
- [39] Etsuro Sawaguchi and Tomoyoshi Kittaka. “Antiferroelectricity and Ferroelectricity in Lead Zirconate”. In: *Journal of the Physical Society of Japan* 7 (1952), pp. 336–337. DOI: 10.1143/JPSJ.7.336.
- [40] Jiake Xia et al. “Evaluation of various methods for energy storage calculation in nonlinear capacitors”. In: *AIP Advances* 10 (2020), p. 095132. DOI: 10.1063/5.0012089.
- [41] A.S. Bhalla, Ruyan Guo, and Rustum Roy. “The Perovskite Structure - A review of its role in ceramic science and technology”. In: *Mat Res Innovat* 4 (2000), pp. 3–26. DOI: 10.1007/s100190000062.
- [42] VM Goldschmidt. “Die Gesetze der Krystallochemie”. In: *Naturwissenschaften* 14 (1926), pp. 477–485. DOI: 10.1007/BF01507527.
- [43] M. C. Morris et al. “Standard X-ray diffraction powder patterns, NBS monograph 25, Section 18, data for 58 substances”. In: *Gaithersburg: National Bureau of Standards* (1981), pp. 64–65.
- [44] Koichi Momma and Fujio Izumi. “VESTA: a three-dimensional visualization system for electronic and structural analysis”. In: *Journal of Applied crystallography* 41 (2008), pp. 653–658.
- [45] B. T. Matthias. “New Ferroelectric Crystals”. In: *Phys. Rev.* 75 (1949), pp. 1771–1771. DOI: 10.1103/PhysRev.75.1771.
- [46] P. Vousden. “A study of the unit-cell dimensions and symmetry of certain ferroelectric compounds of niobium and tantalum at room temperature”. In: *Acta Crystallographica* 4 (1951), pp. 373–376. DOI: 10.1107/S0365110X5100115X.
- [47] E. A. Wood. “Polymorphism in potassium niobate, sodium niobate, and other ABO_3 compounds”. In: *Acta Crystallographica* 4 (1951), pp. 353–362. DOI: 10.1107/S0365110X51001112.
- [48] Karen E. Johnston et al. “ ^{93}Nb NMR and DFT investigation of the polymorphs of NaNbO_3 ”. In: *Phys. Chem. Chem. Phys.* 13 (2011), pp. 7565–7576. DOI: 10.1039/C1CP20258H.

-
- [49] A. M. Glazer and Koichi Ishida. “Cation displacements and octahedral tilts in NaNbO_3 Part I—Determination from X-ray difference reflections”. In: *Ferroelectrics* 6 (1973), pp. 219–224. DOI: 10.1080/00150197408243971.
- [50] Helen D Megaw. “The seven phases of sodium niobate”. In: *Ferroelectrics* 7 (1974), pp. 87–89. DOI: 10.1080/00150197408237956.
- [51] J. Koruza et al. “Phase transitions of sodium niobate powder and ceramics, prepared by solid state synthesis”. In: *Journal of Applied Physics* 108 (2010), p. 113509. DOI: 10.1063/1.3512980.
- [52] Arnold Reisman, Frederic Holtzberg, and Ephraim Banks. “Reactions of the Group VB Pentoxides with Alkali Oxides and Carbonates. VII. Heterogeneous Equilibria in the System Na_2O or $\text{Na}_2\text{CO}_3\text{--Nb}_2\text{O}_5$ ”. In: *Journal of the American Chemical Society* 80 (1958), pp. 37–42. DOI: 10.1021/ja01534a011.
- [53] Hanzheng Guo et al. “Strategy for stabilization of the antiferroelectric phase (Pbma) over the metastable ferroelectric phase (P21ma) to establish double loop hysteresis in lead-free $(1-x)\text{NaNbO}_3\text{--}x\text{SrZrO}_3$ solid solution”. In: *Journal of Applied Physics* 117 (2015). DOI: 10.1063/1.4921876.
- [54] Zhiyong Liu et al. “Energy storage properties of $\text{NaNbO}_3\text{--CaZrO}_3$ ceramics with co-existence of ferroelectric and antiferroelectric phases”. In: *Journal of the European Ceramic Society* 38 (2018), pp. 4939–4945. DOI: 10.1016/j.jeurceramsoc.2018.07.029.
- [55] H Shimizu et al. “Lead-free antiferroelectric: $x\text{CaZrO}_3\text{--}(1-x)\text{NaNbO}_3$ system ($0 \leq x \leq 0.10$)”. In: *Dalton Trans.* 44 (2015), pp. 10763–10772. DOI: 10.1039/c4dt03919j.
- [56] Lisheng Gao et al. “A perovskite lead-free antiferroelectric $x\text{CaHfO}_3\text{--}(1-x)\text{NaNbO}_3$ with induced double hysteresis loops at room temperature”. In: *Journal of Applied Physics* 120 (2016). DOI: 10.1063/1.4968790.
- [57] Lei Zhao et al. “Silver Niobate Lead-Free Antiferroelectric Ceramics: Enhancing Energy Storage Density by B-Site Doping”. In: *ACS Appl. Mater. Interfaces* 10 (2018), pp. 819–826. DOI: 10.1021/acsmi.7b17382.
- [58] He Qi and Ruzhong Zuo. “Linear-like lead-free relaxor antiferroelectric $(\text{Bi}_{0.5}\text{Na}_{0.5})\text{TiO}_3\text{--NaNbO}_3$ with giant energy-storage density/efficiency and super stability against temperature and frequency”. In: *J. Mater. Chem. A* 7 (2019), pp. 3971–3978. DOI: 10.1039/C8TA12232F.

-
- [59] He Qi et al. “Ultrahigh Energy-Storage Density in NaNbO_3 -Based Lead-Free Relaxor Antiferroelectric Ceramics with Nanoscale Domains”. In: *Advanced Functional Materials* (2019). DOI: 10.1002/adfm.201903877.
- [60] Masatomo Yashima et al. “Structure of Ferroelectric Silver Niobate AgNbO_3 ”. In: *Chemistry of Materials* 23 (2011), pp. 1643–1645. DOI: 10.1021/cm103389q.
- [61] Jan Fábry et al. “Silver niobium trioxide, AgNbO_3 ”. In: *Acta Crystallographica Section C* 56 (2000), pp. 916–918. DOI: 10.1107/S0108270100006806.
- [62] Ph Sciau et al. “Structural investigation of AgNbO_3 phases using x-ray and neutron diffraction”. In: *Journal of Physics: Condensed Matter* 16 (2004), pp. 2795–2810. DOI: 10.1088/0953-8984/16/16/004.
- [63] Igor Levin et al. “Structural changes underlying the diffuse dielectric response in AgNbO_3 ”. In: *Phys. Rev. B* 79 (2009), p. 104113. DOI: 10.1103/PhysRevB.79.104113.
- [64] Manish K. Niranjana and Saket Asthana. “First principles study of lead free piezoelectric AgNbO_3 and $(\text{Ag}_{1-x}\text{K}_x)\text{NbO}_3$ solid solutions”. In: *Solid State Communications* 152 (2012), pp. 1707–1710. DOI: 10.1016/j.ssc.2012.05.002.
- [65] Ye Tian et al. “Silver niobate perovskites: structure, properties and multifunctional applications”. In: *Journal of Materials Chemistry A* 10 (2022), pp. 14747–14787. DOI: 10.1039/d2ta00905f.
- [66] Ye Tian et al. “High energy density in silver niobate ceramics”. In: *Journal of Materials Chemistry A* 4 (2016), pp. 17279–17287. DOI: 10.1039/c6ta06353e.
- [67] N. Luo et al. “Constructing phase boundary in AgNbO_3 antiferroelectrics: pathway simultaneously achieving high energy density and efficiency”. In: *Nat Commun* 11 (2020), p. 4824. DOI: 10.1038/s41467-020-18665-5.
- [68] Ye Tian et al. “Phase transitions in bismuth-modified silver niobate ceramics for high power energy storage”. In: *J. Mater. Chem. A* 5 (2017), pp. 17525–17531. DOI: 10.1039/C7TA03821F.
- [69] Jing Gao et al. “Enhanced antiferroelectric phase stability in La-doped AgNbO_3 : perspectives from the microstructure to energy storage properties”. In: *J. Mater. Chem. A* 7 (2019), pp. 2225–2232. DOI: 10.1039/C8TA09353A.
- [70] Nengneng Luo et al. “Design for high energy storage density and temperature-insensitive lead-free antiferroelectric ceramics”. In: *Journal of Materials Chemistry C* 7 (2019), pp. 4999–5008. DOI: 10.1039/c8tc06549g.

-
- [71] Jing Gao et al. “Local Structure Heterogeneity in Sm-Doped AgNbO₃ for Improved Energy-Storage Performance”. In: *ACS Appl. Mater. Interfaces* 12 (2020), pp. 6097–6104. DOI: 10.1021/acsami.9b20803.
- [72] Nengneng Luo et al. “Aliovalent A-site engineered AgNbO₃ lead-free antiferroelectric ceramics toward superior energy storage density”. In: *Journal of Materials Chemistry A* 7 (2019), pp. 14118–14128. DOI: 10.1039/c9ta02053e.
- [73] Wenna Chao et al. “Excellent energy storage performance in La and Ta co-doped AgNbO₃ antiferroelectric ceramics”. In: *Journal of the European Ceramic Society* 41 (2021), pp. 7670–7677. DOI: 10.1016/j.jeurceramsoc.2021.07.062.
- [74] Haoming Wei et al. “LaNiO₃ films with tunable out-of-plane lattice parameter and their strain-related electrical properties”. In: *physica status solidi (a)* 212 (2015), pp. 1925–1930. DOI: 10.1002/pssa.201431695.
- [75] Masatoshi Imada, Atsushi Fujimori, and Yoshinori Tokura. “Metal-insulator transitions”. In: *Rev. Mod. Phys.* 70 (1998), pp. 1039–1263. DOI: 10.1103/RevModPhys.70.1039.
- [76] J.-S. Zhou et al. “Probing the metal-insulator transition in Ni(III)-oxide perovskites”. In: *Phys. Rev. B* 61 (2000), pp. 4401–4404. DOI: 10.1103/PhysRevB.61.4401.
- [77] Tzu-Feng Tseng et al. “Ferroelectric properties of (Pb_{0.97}La_{0.03})(Zr_{0.66}Ti_{0.34})_{0.9875}O₃ films deposited on Si₃N₄-coated Si substrates by pulsed laser deposition process”. In: *Applied Physics Letters* 70 (1997), pp. 46–48. DOI: 10.1063/1.119300.
- [78] Ming-Sen Chen, Tai-Bor Wu, and Jenn-Ming Wu. “Effect of textured LaNiO₃ electrode on the fatigue improvement of Pb(Zr_{0.53}Ti_{0.47})O₃ thin films”. In: *Applied Physics Letters* 68 (1996), pp. 1430–1432. DOI: 10.1063/1.116103.
- [79] Mingwei Zhu et al. “Effect of composition and strain on the electrical properties of LaNiO₃ thin films”. In: *Appl. Phys. Lett.* 103 (2013), p. 141902. DOI: 10.1063/1.4823697.
- [80] Quan-Liang Zhao et al. “Energy storage and thermodynamics of PNZST thick films with coexisting antiferroelectric and ferroelectric phases”. In: *International Journal of Applied Ceramic Technology* 18 (2020), pp. 154–161. DOI: 10.1111/ijac.13642.
- [81] Xiaolin Wang et al. “Enhanced Energy-Storage Performance of an All-Inorganic, Antiferroelectric, Thin-Film via Orientation Adjustments”. In: *IEEE Access* 8 (2020), pp. 217246–217254. DOI: 10.1109/access.2020.3039349.

-
- [82] Henghui Cai et al. “Significantly improved energy storage properties and cycling stability in La-doped PbZrO_3 antiferroelectric thin films by chemical pressure tailoring”. In: *Journal of the European Ceramic Society* 39 (2019), pp. 4761–4769. DOI: 10.1016/j.jeurceramsoc.2019.07.024.
- [83] C. W. Ahn et al. “Antiferroelectric Thin-Film Capacitors with High Energy-Storage Densities, Low Energy Losses, and Fast Discharge Times”. In: *ACS Appl Mater Interfaces* 7 (2015), pp. 26381–6. DOI: 10.1021/acsami.5b08786.
- [84] Zhongqiang Hu et al. “Temperature-dependent energy storage properties of antiferroelectric $\text{Pb}_{0.96}\text{La}_{0.04}\text{Zr}_{0.98}\text{Ti}_{0.02}\text{O}_3$ thin films”. In: *Applied Physics Letters* 104 (2014), p. 263902. DOI: 10.1063/1.4887066.
- [85] C. H. Ahn, K. M. Rabe, and Jean-Marc Triscone. “Ferroelectricity at the Nanoscale: Local Polarization in Oxide Thin Films and Heterostructures”. In: *Science* 303 (2004). DOI: 10.1126/science.1092508.
- [86] D. D. Fong et al. “Ferroelectricity in Ultrathin Perovskite Films”. In: *Science* 304 (2004). DOI: 10.1126/science.1098252.
- [87] E.V. Charnaya, O.S. Pogorelova, and C. Tien. “Phenomenological model for the antiferroelectric phase transition in thin films and small particles”. In: *Physica B* 305 (2001), pp. 97–104. DOI: 10.1016/S0921-4526(01)00613-5.
- [88] E. A. Eliseev, M. D. Glinchuk, and A. N. Morozovska. “Antiferroelectric thin films phase diagrams”. In: *Phase Transitions* 80 (2007), pp. 47–54. DOI: 10.1080/01411590601092654.
- [89] Angus Rockett. “Thin film growth processes”. In: *The materials science of semiconductors*. Springer Science & Business Media, 2007. Chap. 10.
- [90] Milton Ohring. “Substrate surfaces and thin-film nucleation”. In: *Materials Science of Thin Films: Deposition & Structure*. San Diego, CA, USA: Academic Press, 2002. Chap. 7, pp. 357–415.
- [91] Ran Xu et al. “Effects of compressive stress on electric-field-induced phase transition of antiferroelectric ceramics”. In: *Journal of Applied Physics* 125 (2019). DOI: 10.1063/1.5089163.
- [92] Zhen Liu et al. “Lead-free $(\text{Ag,K})\text{NbO}_3$ materials for high-performance explosive energy conversion”. In: *Science Advance* 6 (2020). DOI: 10.1126/sciadv.aba0367.

-
- [93] Hassel Ledbetter, Ming Lei, and Sudook Kim. “Elastic constants, Debye temperatures, and electron-phonon parameters of superconducting cuprates and related oxides”. In: *Ph. Transit.* 23 (1990), pp. 61–70. DOI: 10.1080/01411599008241819.
- [94] Ayan Roy Chaudhuri et al. “Epitaxial strain stabilization of a ferroelectric phase in PbZrO_3 thin films”. In: *Physical Review B* 84 (2011). DOI: 10.1103/PhysRevB.84.054112.
- [95] Jun Ge et al. “Enhancement of energy storage in epitaxial PbZrO_3 antiferroelectric films using strain engineering”. In: *Applied Physics Letters* 105 (2014). DOI: 10.1063/1.4896156.
- [96] V. Lingwal, B.S. Semwal, and N.S. Panwar. “Dielectric Properties Of $\text{Na}_{1-x}\text{K}_x\text{NbO}_3$ in orthorhombic phase”. In: *Bull. Mater. Sci.* 26 (2003), pp. 619–625. DOI: 10.1007/BF02704326.
- [97] W. J. Maeng, I. Jung, and J. Y. Son. “Enhanced ferroelectric polarization in tetragonally strained NaNbO_3 thin film on single crystal Rh substrate”. In: *Journal of Crystal Growth* 349 (2012), pp. 24–26. DOI: 10.1016/j.jcrysgro.2012.04.009.
- [98] Jan Sellmann et al. “Strained ferroelectric NaNbO_3 thin films: Impact of pulsed laser deposition growth conditions on structural properties”. In: *Thin Solid Films* 570 (2014), pp. 107–113. DOI: 10.1016/j.tsf.2014.09.016.
- [99] Yasuyoshi Saito et al. “Lead-free piezoceramics”. In: *Nature* 432 (2004), pp. 84–87. DOI: 10.1038/nature03028.
- [100] Jutta Schwarzkopf et al. “Strain-induced phase transitions in epitaxial NaNbO_3 thin films grown by metal–organic chemical vapour deposition”. In: *J. Appl. Crystallogr.* 45 (2012), pp. 1015–1023. DOI: 10.1107/s0021889812035911.
- [101] B Cai et al. “Anisotropic ferroelectric properties of anisotropically strained epitaxial NaNbO_3 films”. In: *J. Appl. Phys.* 115 (2014), p. 224103. DOI: 10.1063/1.4882296.
- [102] Seiji Yamazoe et al. “The effect of SrTiO_3 substrate orientation on the surface morphology and ferroelectric properties of pulsed laser deposited NaNbO_3 films”. In: *Appl. Phys. Lett.* 95 (2009), p. 062906. DOI: 10.1063/1.3205103.
- [103] Huijuan Dong et al. “Electrical study of antiferroelectric NaNbO_3 thin films integrated directly on 4H–SiC”. In: *Journal of Physics and Chemistry of Solids* 143 (2020). DOI: 10.1016/j.jpcs.2020.109477.

-
- [104] Seiji Yamazoe et al. “Observation of domain structure in 001 orientated NaNbO₃ films deposited on (001)SrTiO₃ substrates by laser beam scanning microscopy”. In: *Appl. Phys. Lett.* 96 (2010), p. 092901. DOI: 10.1063/1.3330963.
- [105] Yu I. Yuzyuk et al. “Ferroelectric Q-phase in a NaNbO₃ epitaxial thin film”. In: *Applied Physics Letters* 96 (2010). DOI: 10.1063/1.3437090.
- [106] Kinnary Patel et al. “Properties of (001) NaNbO₃ films under epitaxial strain: A first-principles study”. In: *Phys. Rev. B* 103 (2021), p. 094103. DOI: 10.1103/PhysRevB.103.094103.
- [107] Jianglei Ma et al. “Enhanced energy storage properties of silver niobate ceramics under hydrostatic pressure”. In: *Materials Letters* 247 (2019), pp. 40–43. DOI: 10.1016/j.matlet.2019.03.035.
- [108] Linguang Zhu, Xiangjian Wang, and Xiaojie Lou. “Effects of Epitaxial Strain on Antiferrodistortion of AgNbO₃ from First-Principle Calculations”. In: *physica status solidi (RRL) - Rapid Research Letters* 12 (2018). DOI: 10.1002/pssr.201800007.
- [109] Mao-Hua Zhang et al. “Revealing the mechanism of electric-field-induced phase transition in antiferroelectric NaNbO₃ by in situ high-energy x-ray diffraction”. In: *Appl. Phys. Lett.* 118 (2021), p. 132903. DOI: 10.1063/5.0043050.
- [110] Hiroyuki Sakurai, Seiji Yamazoe, and Takahiro Wada. “Ferroelectric and antiferroelectric properties of AgNbO₃ films fabricated on (001), (110), and (111)SrTiO₃ substrates by pulsed laser deposition”. In: *Applied Physics Letters* 97 (2010). DOI: 10.1063/1.3467137.
- [111] M. B. Telli et al. “(001) epitaxial AgTaO₃ and AgNbO₃ thin films on (001)SrRuO₃/(001)LaAlO₃ substrates by chemical solution deposition”. In: *Applied Physics Letters* 89 (2006). DOI: 10.1063/1.2403918.
- [112] M. Valant et al. “Strain influence on crystallography of AgNbO₃-based thin films”. In: *Journal of Optoelectronics and Advanced Materials* 9 (2007), pp. 1377–1381.
- [113] Liang Shu et al. “Phase-pure antiferroelectric AgNbO₃ films on Si substrates: chemical solution deposition and phase transitions”. In: *Journal of Materials Chemistry A* 10 (2022), pp. 12632–12642. DOI: 10.1039/d2ta01577c.
- [114] Lambert Alff et al. “Vapor-Phase Deposition of Oxides”. In: *Ceramics Science and Technology*. John Wiley & Sons, Ltd, 2011. Chap. 11, pp. 267–290. DOI: 10.1002/9783527631957.ch11.
- [115] Robert Eason. *Pulsed Laser Deposition of Thin Films: Applications-Led Growth of Functional Materials*. Wiley, 2007.

-
-
- [116] P. Willmott and J.R. Huber. “Pulsed Laser vaporization and deposition”. In: *Reviews of Modern Physics* 72 (2000), p. 315. DOI: 10.1103/RevModPhys.72.315.
- [117] Dave H. A. Blank, Matthijn Dekkers, and Guus Rijnders. “Pulsed laser deposition in Twente: from research tool towards industrial deposition”. In: *Journal of Physics D: Applied Physics* 47 (2014). DOI: 10.1088/0022-3727/47/3/034006.
- [118] P. Willmott. “Deposition of complex multielemental thin films”. In: *Progress in Surface Science* 76 (2004), pp. 163–217. DOI: 10.1016/j.progsurf.2004.06.001.
- [119] S.K. Hau et al. “Intrinsic resputtering in pulsed-laser deposition of lead-zirconate-titanate thin films”. In: *Applied physics letters* 66 (1995), pp. 245–247. DOI: 10.1063/1.113560.
- [120] S Wicklein et al. “Pulsed laser ablation of complex oxides: The role of congruent ablation and preferential scattering for the film stoichiometry”. In: *Applied physics letters* 101 (2012). DOI: 10.1063/1.4754112.
- [121] R. Dittmann. “9 - Stoichiometry in epitaxial oxide thin films”. In: *Epitaxial Growth of Complex Metal Oxides*. Ed. by G. Koster, M. Huijben, and G. Rijnders. Woodhead Publishing Series in Electronic and Optical Materials. Woodhead Publishing, 2015, pp. 231–261. ISBN: 978-1-78242-245-7. DOI: 10.1016/B978-1-78242-245-7.00009-9.
- [122] M. N. Ashfold et al. “Pulsed laser ablation and deposition of thin films”. In: *Chem Soc Rev* 33 (2004), pp. 23–31. DOI: 10.1039/b207644f.
- [123] T.E. Itina, W. Marine, and M. Autric. “Monte Carlo simulation of pulsed laser ablation from two-component target into diluted ambient gas”. In: *Journal of applied physics* 82 (1997), pp. 3536–3542. DOI: 10.1063/1.365672.
- [124] H. M. Christen and G. Eres. “Recent advances in pulsed-laser deposition of complex oxides”. In: *J Phys Condens Matter* 20 (2008), p. 264005. DOI: 10.1088/0953-8984/20/26/264005.
- [125] Agham-Bayan Posadas et al. “Growth and novel applications of epitaxial oxide thin films”. In: *Physics of Ferroelectrics: A Modern Perspective* (2007), pp. 219–304.
- [126] William Henry Bragg and William Lawrence Bragg. “The reflection of X-rays by crystals”. In: *Proceedings of the Royal Society of London. Series A, Containing Papers of a Mathematical and Physical Character* 88 (1913), pp. 428–438. DOI: 10.1098/rspa.1913.0040.

-
-
- [127] Yoshio Waseda et al. “Fundamental Properties of X-rays”. In: *X-Ray Diffraction Crystallography: Introduction, Examples and Solved Problems* (2011), pp. 1–20. DOI: 10.1007/978-3-642-16635-8_1.
- [128] Katsuhiko Inaba. “X-ray thin-film measurement techniques”. In: *The Rigaku Journal* 24 (2008), pp. 10–15.
- [129] Toru Mitsunaga. “X-ray thin-film measurement techniques”. In: *Rigaku J* 25 (2009), pp. 7–12.
- [130] Jo Bo Nelson and DP Riley. “An experimental investigation of extrapolation methods in the derivation of accurate unit-cell dimensions of crystals”. In: *Proceedings of the Physical Society* 57 (1945), p. 160. DOI: 10.1088/0959-5309/57/3/302.
- [131] M Maul et al. “Epitaxial CeO₂ buffer layers for YBa₂Cu₃O_(7-x) films on sapphire”. In: *Journal of applied physics* 74 (1993), pp. 2942–2944. DOI: 10.1063/1.354650.
- [132] Miho Yasaka et al. “X-ray thin-film measurement techniques”. In: *The Rigaku Journal* 26 (2010), pp. 1–9.
- [133] JF Moulder et al. *Handbook of X-ray Photoelectron Spectroscopy*. 1992.
- [134] Alexander G Shard. “Practical guides for x-ray photoelectron spectroscopy: Quantitative XPS”. In: *Journal of Vacuum Science & Technology A* 38 (2020). DOI: 10.1002/sia.740030506.
- [135] C. D. Wagner et al. “Empirical atomic sensitivity factors for quantitative analysis by electron spectroscopy for chemical analysis”. In: *Surface and Interface Analysis* 3 (1981), pp. 211–225. DOI: 10.1002/sia.740030506.
- [136] Fu-Chien Chiu. “A Review on Conduction Mechanisms in Dielectric Films”. In: *Adv. Mater. Sci. Eng.* 2014 (2014), pp. 1–18. DOI: 10.1155/2014/578168.
- [137] M. Dawber, K. M. Rabe, and J. F. Scott. “Physics of thin-film ferroelectric oxides”. In: *Rev. Mod. Phys.* 77 (2005), pp. 1083–1130. DOI: 10.1103/RevModPhys.77.1083.
- [138] E. L. Murphy and R. H. Good. “Thermionic Emission, Field Emission, and the Transition Region”. In: *Phys. Rev.* 102 (1956), pp. 1464–1473. DOI: 10.1103/PhysRev.102.1464.
- [139] Klaus Prume, Thorsten Schmitz, and Stephan Tiedke. “Electrical Characterization of Ferroelectrics”. In: *Polar Oxides*. 2004. Chap. 3, pp. 53–75. DOI: 10.1002/3527604650.ch3.
- [140] T. Schenk et al. “About the deformation of ferroelectric hystereses”. In: *Applied Physics Reviews* 1 (2014). DOI: 10.1063/1.4902396.

-
- [141] Charles Baldwin Sawyer and CH Tower. “Rochelle salt as a dielectric”. In: *Physical review* 35 (1930), p. 269. DOI: 10.1103/PhysRev.35.269.
- [142] J F Scott. “Ferroelectrics go bananas”. In: *J. Condens. Matter Phys.* 20 (2008), p. 021001. DOI: 10.1088/0953-8984/20/02/021001.
- [143] Li Jin et al. “Decoding the Fingerprint of Ferroelectric Loops: Comprehension of the Material Properties and Structures”. In: *Journal of the American Ceramic Society* 97 (2014), pp. 1–27. DOI: 10.1111/jace.12773.
- [144] Dave A Shirley. “High-resolution X-ray photoemission spectrum of the valence bands of gold”. In: *Physical Review B* 5 (1972), p. 4709. DOI: 10.1103/PhysRevB.5.4709.
- [145] I. Aulika et al. “Structural and optical Studies of NaNbO₃ thin films grown by PLD on SrRuO₃ bottom electrode”. In: *Reviews on advanced Material Science* 15 (2007), pp. 158–166.
- [146] S. Oda et al. “Preparation of ferroelectric NaNbO₃ thin films on MgO substrate by pulsed laser deposition”. In: *IEEE Trans Ultrason Ferroelectr Freq Control* 55 (2008), pp. 1017–22. DOI: 10.1109/TUFFC.2008.748.
- [147] Seiji Yamazoe et al. “Laser beam scanning microscope and piezoresponse force microscope studies on domain structured in 001-, 110-, and 111-oriented NaNbO₃ films”. In: *Journal of Applied Physics* 112 (2012). DOI: 10.1063/1.4746079.
- [148] Sandra Hildebrandt et al. “Epitaxial growth and control of the sodium content in Na_xCoO₂ thin films”. In: *Thin Solid Films* 545 (2013), pp. 291–295. DOI: 10.1016/j.tsf.2013.08.072.
- [149] A. Popovič et al. “Vapour pressure and mixing thermodynamic properties of the KNbO₃–NaNbO₃ system”. In: *RSC Adv.* 5 (2015), pp. 76249–76256. DOI: 10.1039/C5RA11874C.
- [150] Thorsten Schneider et al. “Evidence for antipolar displacements in NaNbO₃ thin films”. In: *Appl. Phys. Lett.* 121 (2022), p. 122906. DOI: 10.1063/5.0101739.
- [151] Juliette Cardoletti et al. “{ 001}-Textured Pb(Zr,Ti)O₃ Thin Films on Stainless Steel by Pulsed Laser Deposition”. In: *J. Appl. Phys.* 128 (2020), p. 104103. DOI: 10.1063/5.0019967.
- [152] Mingwei Zhu et al. “Joint effect of composition and strain on the anomalous transport properties of LaNiO₃ films”. In: *Journal of Applied Physics* 117 (2015), p. 155306. DOI: 10.1063/1.4918661.

-
- [153] Yongbo Fan, Weijia Wang, and Jinyan Zhao. “Fabrication, structural and dielectric property of lead-free perovskite silver niobate ceramics”. In: *Ceramics International* 46 (2020), pp. 12269–12274. DOI: 10.1016/j.ceramint.2020.01.276.
- [154] Jung-Hyuk Koh, S. I. Khartsev, and Alex Grishin. “Ferroelectric silver niobate-tantalate thin films”. In: *Applied Physics Letters* 77 (2000), pp. 4416–4418. DOI: 10.1063/1.1334655.
- [155] Thorsten Schneider et al. “Strain impact on crystal structure in stoichiometric AgNbO₃ epitaxial thin films with compensated silver deficiency”. unpublished.
- [156] S. Yilmaz, T. Venkatesan, and R. Gerhard-Multhaupt. “Pulsed laser deposition of stoichiometric potassium-tantalate-niobate films from segmented evaporation targets”. In: *Applied Physics Letters* 58 (1991), pp. 2479–2481. DOI: 10.1063/1.104849.
- [157] P W M Jacobs, J Corish, and C R A Catlow. “Ionic mobility in silver chloride”. In: *Journal of Physics C: Solid State Physics* 13 (1980), p. 1977. DOI: 10.1088/0022-3719/13/10/017.
- [158] F. Jona, G. Shirane, and R. Pepinsky. “Optical Study of PbZrO₃ and NaNbO₃ Single Crystals”. In: *Phys. Rev.* 97 (1955), pp. 1584–1590. DOI: 10.1103/PhysRev.97.1584.
- [159] Qingzhu Ma et al. “Dielectric and Antiferroelectric Properties of AgNbO₃ Films Deposited on Different Electrodes”. In: *Coatings* 12 (2022). DOI: 10.3390/coatings12121826.
- [160] Thorsten Schneider et al. “Impact of Strain Engineering on Antiferroelectricity in NaNbO₃ Thin Films”. In: *ACS Omega* 8 (2023), pp. 23587–23595. DOI: 10.1021/acsomega.3c01327.
- [161] A. P. Chen et al. “Strong oxygen pressure dependence of ferroelectricity in BaTiO₃/SrRuO₃/SrTiO₃ epitaxial heterostructures”. In: *J. Appl. Phys.* 114 (2013), p. 124101. DOI: 10.1063/1.4821643.
- [162] Y. Z. Yoo et al. “Contribution of oxygen partial pressures investigated over a wide range to SrRuO₃ thin-film properties in laser deposition processing”. In: *J. Appl. Phys.* 97 (2005), p. 103525. DOI: 10.1063/1.1909284.
- [163] Lorenzo Villa, Elaheh Ghorbani, and Karsten Albe. “Role of intrinsic defects in cubic NaNbO₃: A computational study based on hybrid density-functional theory”. In: *J. Appl. Phys.* 131 (2022), p. 124106. DOI: 10.1063/5.0079881.
- [164] Dorin Rusu et al. “Ferroelectric incommensurate spin crystals”. In: *Nature* 602 (2022), pp. 240–244. DOI: 10.1038/s41586-021-04260-1.

-
- [165] Sujit Das et al. “Perspective: Emergent topologies in oxide superlattices”. In: *APL Mater.* 6 (2018), p. 100901. DOI: 10.1063/1.5046100.
- [166] G. L. Yuan and A. Uedono. “Behavior of oxygen vacancies in BiFeO₃/SrRuO₃/SrTiO₃(100) and DyScO₃(100) heterostructures”. In: *Appl. Phys. Lett.* 94 (2009), p. 132905. DOI: 10.1063/1.3114993.
- [167] V. Shabadi et al. “Origin of superstructures in (double) perovskite thin films”. In: *Journal of Applied Physics* 116 (2014), p. 114901. DOI: 10.1063/1.4895636.
- [168] David I. Woodward and Ian M. Reaney. “Electron diffraction of tilted perovskites”. In: *Acta Crystallographica Section B* 61 (2005), pp. 387–399. DOI: 10.1107/S0108768105015521.
- [169] Sami Vasala and Maarit Karppinen. “A₂B'B”O₆ perovskites: A review”. In: *Progress in Solid State Chemistry* 43 (2015), pp. 1–36. DOI: 10.1016/j.progsolidstchem.2014.08.001.
- [170] P. M. Woodward. “Octahedral Tilting in Perovskites. I. Geometrical Considerations”. In: *Acta Crystallographica Section B* 53 (1997), pp. 32–43. DOI: 10.1107/S0108768196010713.
- [171] Min Chen et al. “Phase identification and structural evolution in BMT modified NN anti-ferroelectric ceramics”. In: *Journal of the European Ceramic Society* 42 (2022), pp. 6504–6511. DOI: 10.1016/j.jeurceramsoc.2022.07.029.
- [172] Lothar Spieß et al. “Untersuchungen an dünnen Schichten”. In: *Moderne Röntgenbeugung: Röntgendiffraktometrie für Materialwissenschaftler, Physiker und Chemiker*. Springer Fachmedien Wiesbaden, 2019, pp. 481–516. DOI: 10.1007/978-3-8348-8232-5_13.
- [173] Hui Ding et al. “Domain morphology of newly designed lead-free antiferroelectric NaNbO₃-SrSnO₃ ceramics”. In: *J. Am. Ceram. Soc.* 104 (2021), p. 1. DOI: 10.1111/jace.17738.
- [174] Felix V. E. Hensling et al. “Unraveling the enhanced Oxygen Vacancy Formation in Complex Oxides during Annealing and Growth”. In: *Scientific Reports* 7 (2017), p. 39953. DOI: 10.1038/srep39953.
- [175] Katharina N. S. Schuldt et al. “Influence of Defects on the Schottky Barrier Height at BaTiO₃/RuO₂ Interfaces”. In: *physica status solidi (a)* 218 (2021), p. 2100143. DOI: 10.1002/pssa.202100143.
- [176] Nicole Bein et al. “Fermi energy, electrical conductivity, and the energy gap of NaNbO₃”. In: *Phys. Rev. Mater.* 6 (2022), p. 084404. DOI: 10.1103/PhysRevMaterials.6.084404.

-
- [177] Jitendra Kumar Singh, Sujit Kumar Mandal, and Gautam Banerjee. “Refractive index of different perovskite materials”. In: *J. Mater. Res.* 36 (2021), pp. 1773–1793. DOI: 10.1557/s43578-021-00257-8.
- [178] Lukas Zeinar et al. “Matching conflicting oxidation conditions and strain accommodation in perovskite epitaxial thin-film ferroelectric varactors”. In: *J. Appl. Phys.* 128 (2020), p. 214104. DOI: 10.1063/5.0021097.
- [179] Yaser Bastani et al. “Critical thickness for extrinsic contributions to the dielectric and piezoelectric response in lead zirconate titanate ultrathin films”. In: *J. Appl. Phys.* 109 (2011), p. 014115. DOI: 10.1063/1.3527970.
- [180] H. W. Jang et al. “Strain-Induced Polarization Rotation in Epitaxial (001) BiFeO₃ Thin Films”. In: *Phys. Rev. Lett.* 101 (2008), p. 107602. DOI: 10.1103/PhysRevLett.101.107602.
- [181] Lu You et al. “Effect of lanthanum doping on tetragonal-like BiFeO₃ with mixed-phase domain structures”. In: *Phys. Rev. B* 90 (2014), p. 134110. DOI: 10.1103/PhysRevB.90.134110.

Acknowledgements

I extend my sincere appreciation to all those who played a significant role in the process of this dissertation, whether through direct or indirect contributions.

First and foremost, I would like to thank Prof. Dr. Lambert Alff, whose guidance has been invaluable since my involvement in his research group. His encouragement, open-door policy for discussions, and the opportunities to enhance my skills on personal and scientific fronts throughout the years have allowed me to conduct this thesis.

Special recognition is owed to Prof. Dr. Leopoldo Molina-Luna, whose supervision of HRTEM experiments and support during paper writing were crucial. I am also grateful for his role as the second referee.

I extend my gratitude to Prof. Dr. Wolfgang Donner and Prof. Dr. Jurij Koruza for their constructive critiques and expert guidance within the FLAME project, which significantly enriched the quality of this work. Further, I would like to express my gratefulness for their roles in my committee.

Within the ATFT group, Dr. Philipp Komissinskiy and Dr. Juliette Cardoletti deserve my sincere thanks for their constant feedback, insightful discussion, and guidance throughout my whole PhD time. Especially their meticulous paper corrections significantly improved the quality of my research.

Of course this thesis could not have been written without the endless support from my colleagues within the ATFT group. Further thanks goes to the colleagues which have been going to great efforts to keep our devices running: Dipl.-Ing. Gabi Haindl who constructed the DAISY-BAT PLD, without which this thesis could have never been conducted, Jürgen Schreck, who was always available for reparations, service and open for questions related to technical problems, and my colleagues who maintained the other machines, each with its unique challenges. Moreover, I appreciated the great atmosphere within the group and all the help I got from the various members which are not named explicitly.

Besides my research group, I received manifold support within the FLAME project from the hessian state, which also financed the research conducted in this thesis. Cooperation with other members of the FLAME project, mainly Mao-Hua Zhang and Hui Ding, enriched this work. Further, I would like to thank all FLAME members for the countless discussion within PhD meetings, project meetings and great time in Summer schools!

Acknowledgement is due to the Mechanical and Electronic Workshop of the Materials Science department, with special mention to Michael Weber, for their support in overcoming challenging tasks.

Appreciation is extended to Marion Bracke, Angela Dreher, and Dr. Márton Major for their open doors and reliable assistance with project issues.

I thank all professors and scientific staff of the Department for their advisory contributions. Lastly, heartfelt thanks to my wife, and my family and my friends for their unwavering support, love, and for making this world a wonderful place to be.

Appendix

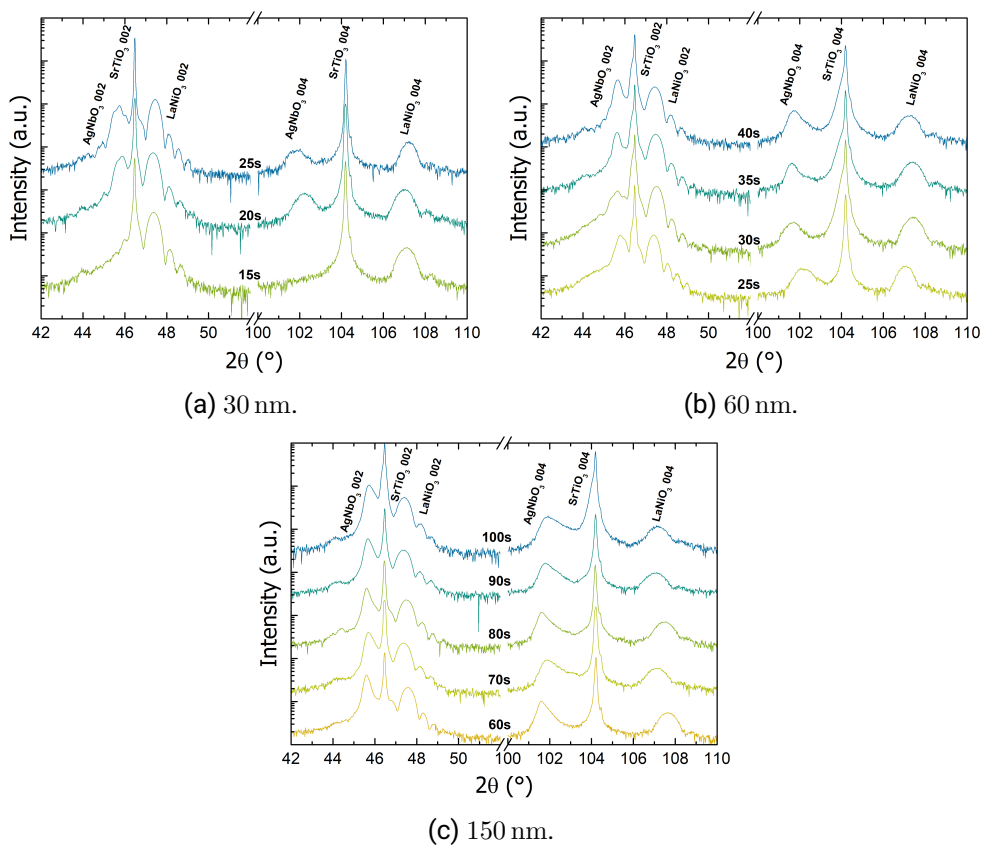


Figure S1: θ - 2θ scans of thin films grown from a stoichiometric AgNbO_3 target with the indicated thickness. For each thickness of the thin film, the thickness of the Ag compensation layer is changed, as denoted by the sputtering time in the respective graph. 1 s conforms to ~ 1 nm.

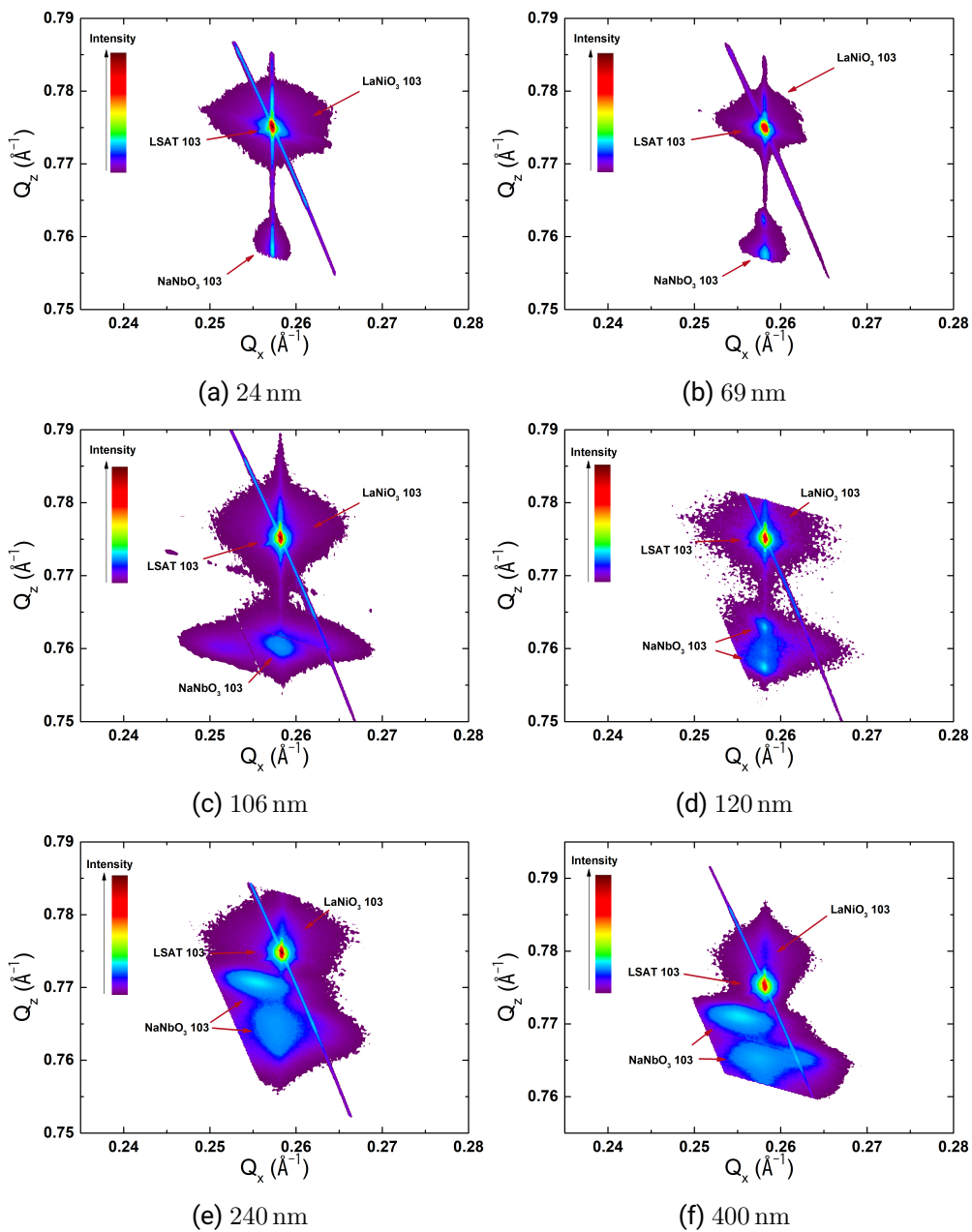


Figure S2: All RSMs around the 103 substrate reflection for NaNbO_3 grown on $\text{LaNiO}_3/\text{LSAT}$ with varying thickness. Reprinted with permission.[160]

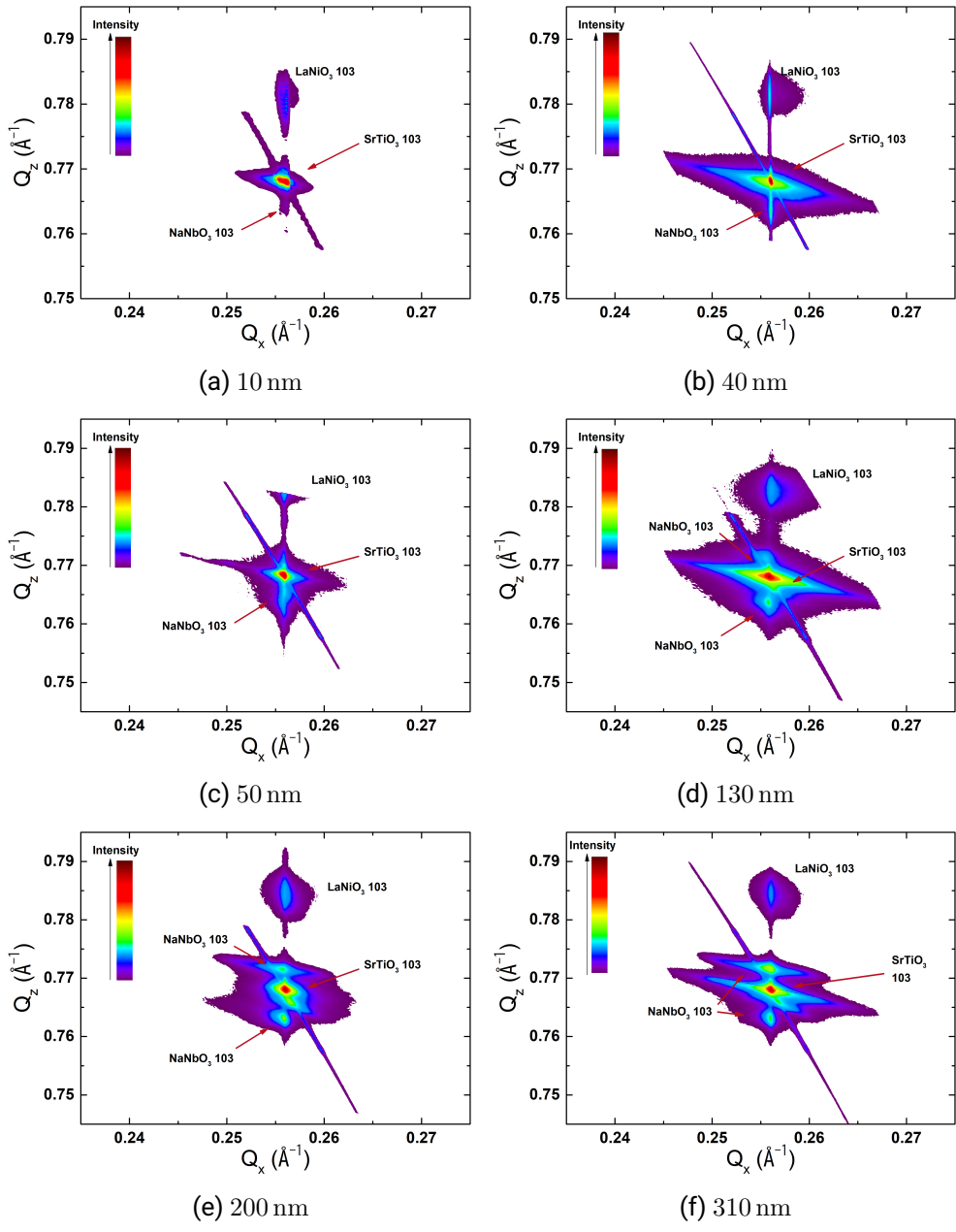


Figure S3: All RSMs around the 103 substrate reflection for NaNbO_3 grown on $\text{LaNiO}_3/\text{SrTiO}_3$ with varying thickness. Reprinted with permission.[160]

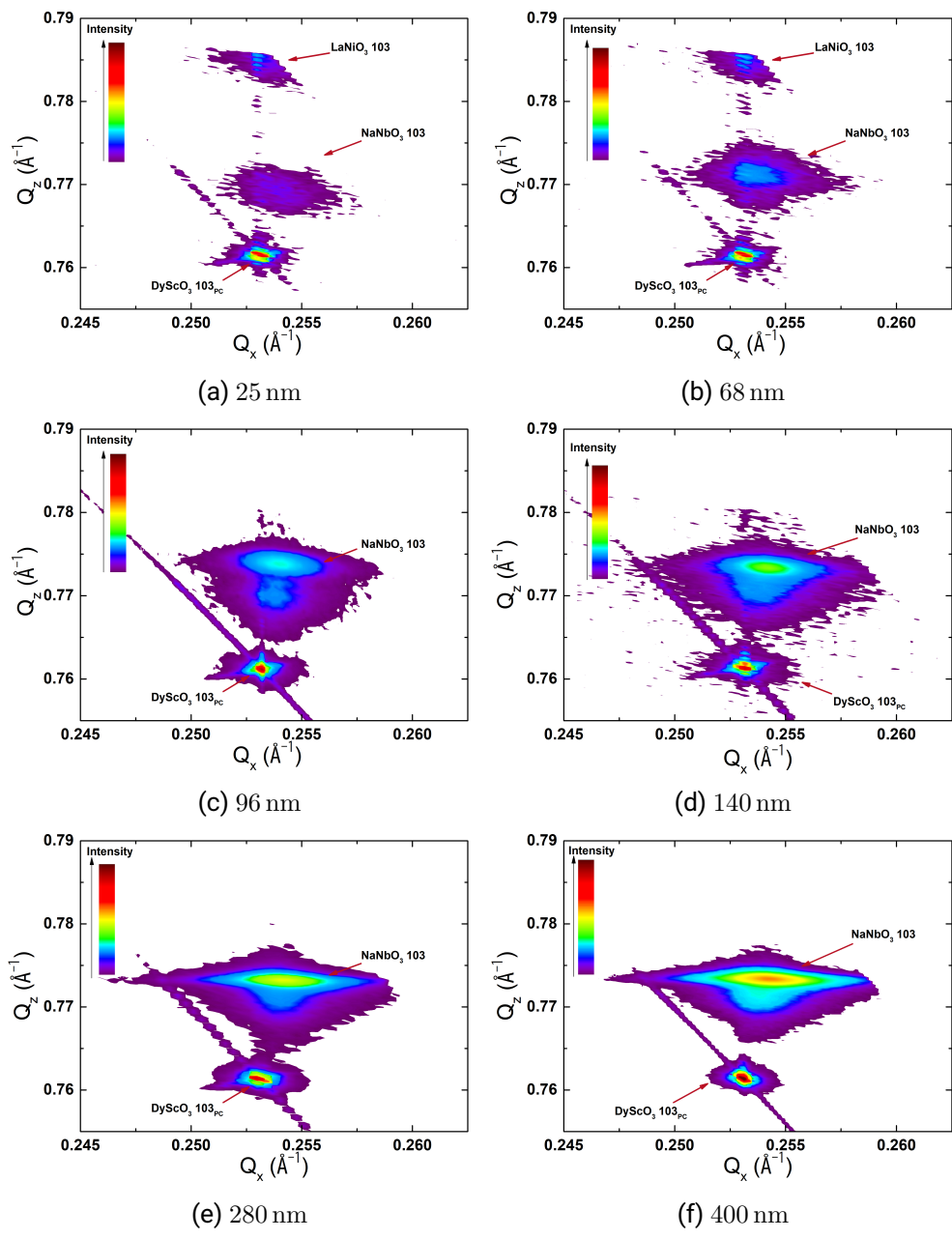


Figure S4: All RSMs around the 103 substrate reflection for NaNbO_3 grown on $\text{LaNiO}_3/\text{DyScO}_3$ with varying thickness. Reprinted with permission.[160]

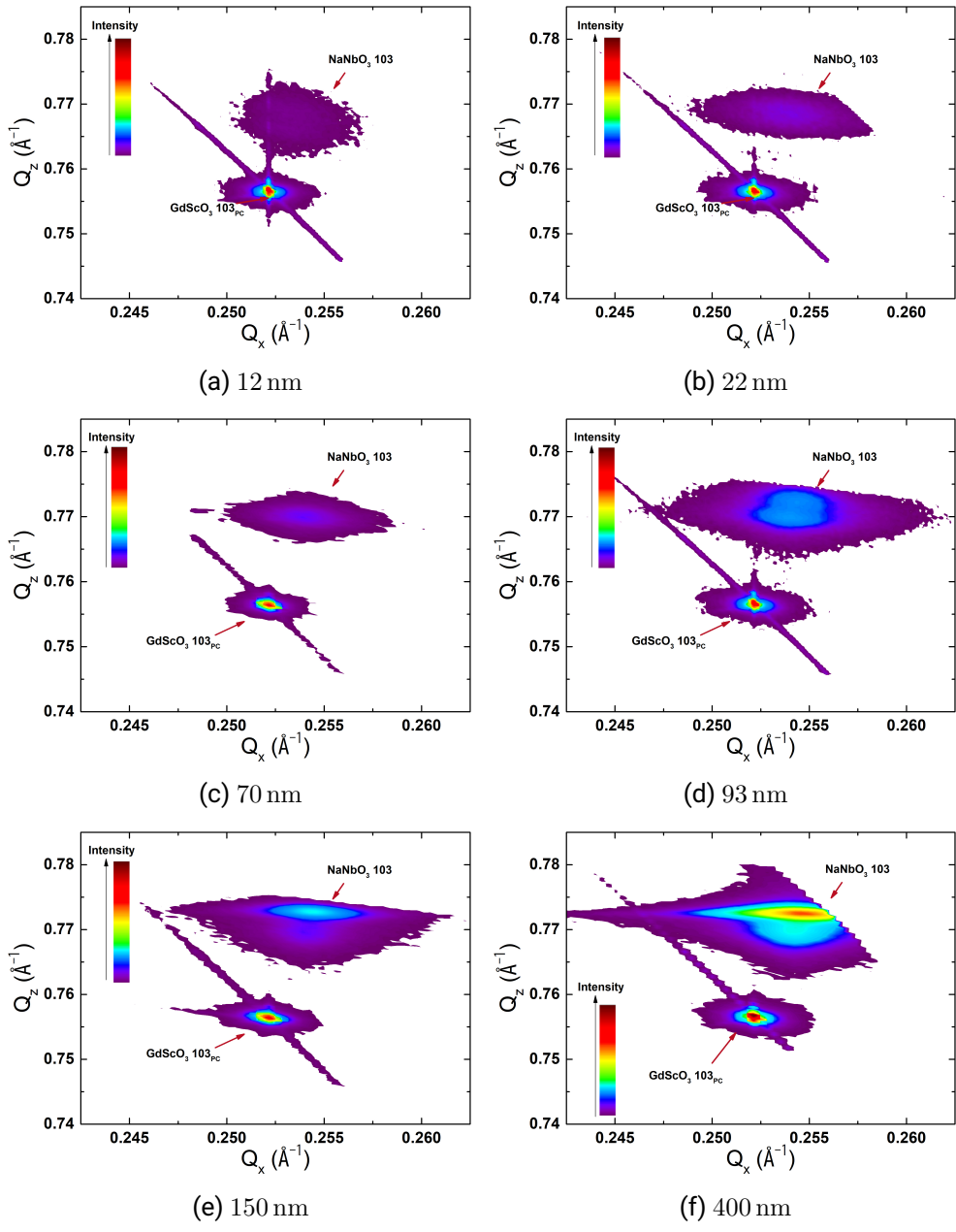
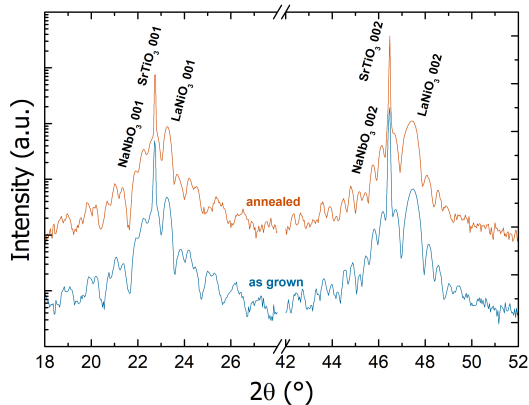
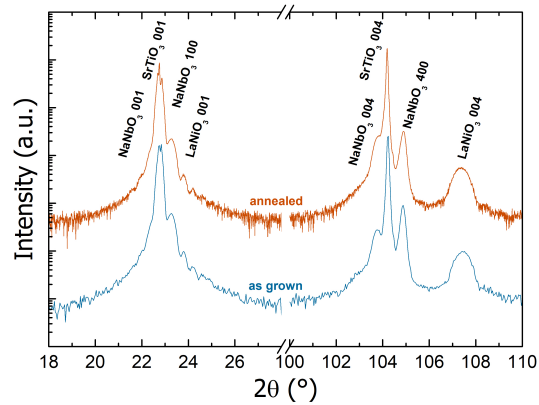


Figure S5: All RSMs around the 103 substrate reflection for NaNbO_3 grown on $\text{LaNiO}_3/\text{GdScO}_3$ with varying thickness. Reprinted with permission.[160]

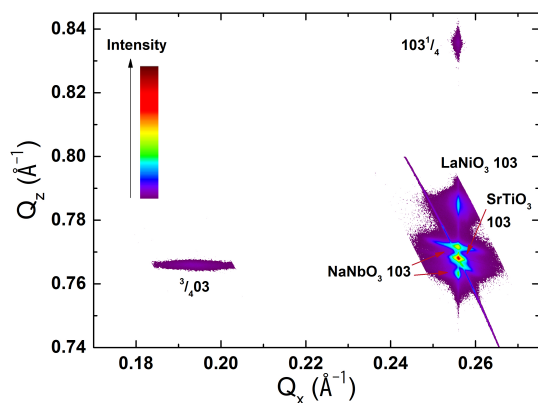


(a) 10 nm thick NaNbO₃ film on SrTiO₃.

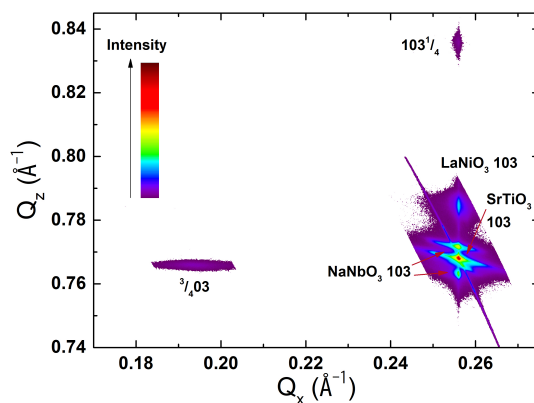


(b) 310 nm thick NaNbO₃ film on SrTiO₃.

Figure S6: Comparison between the $\theta - 2\theta$ scans of NaNbO₃ grown on LaNiO₃/SrTiO₃ before and after the heat treatment. Reprinted with permission.[160]



(a) RSM before the heat treatment.



(b) RSM after the heat treatment.

Figure S7: Comparison between the RSMs of the 310 nm thick NaNbO₃ film on LaNiO₃/SrTiO₃ before and after the heat treatment. Reprinted with permission.[160]

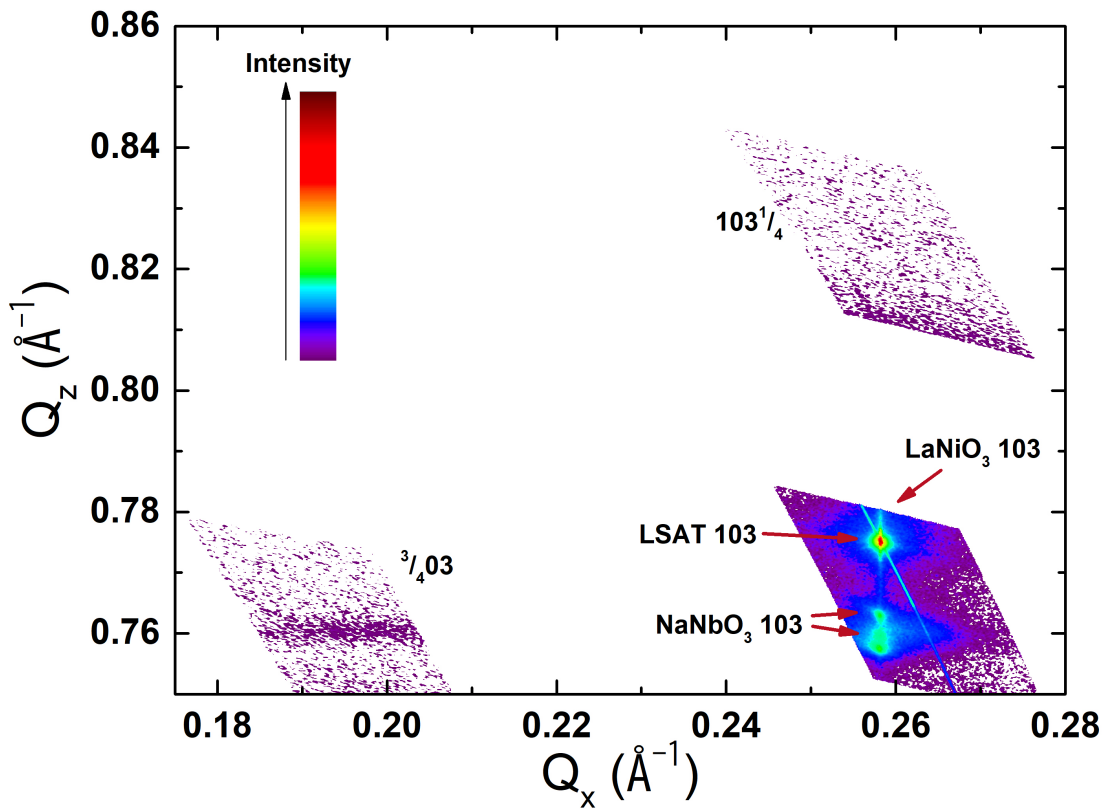


Figure S8: RSM of $NaNbO_3$ grown on $LaNiO_3/LSAT$ around the 103 substrate reflection. Additionally, the areas for the expected superlattice reflection are shown.

List of Publications and Conference Contributions

Peer-reviewed Publications

Thorsten Schneider, Juliette Cardoletti, Hui Ding, Mao-Hua Zhang, Tianshu Jiang, Márton Major, Philipp Komissinskiy, Leopoldo Molina-Luna, and Lambert Alff. “Evidence for antipolar displacements in NaNbO₃ thin films”. In: *Applied Physics Letters* 121 (2022), DOI: <https://doi.org/10.1063/5.0101739>

Thorsten Schneider, Juliette Cardoletti, Philipp Komissinskiy and Lambert Alff. “Impact of Strain Engineering on Antiferroelectricity in NaNbO₃ Thin Films”. In: *ACS Omega* 8 (2023), DOI: <https://doi.org/10.1021/acsomega.3c01327>

Nicole Bein, Brigita Kmet, Tadej Rojac, Andreja Benčn Golob, Barbara Malič, Julian Moxter, **Thorsten Schneider**, Lovro Fulanovic, Maryam Azadeh, Till Frömling, Sonja Egert, Hongguang Wang, Peter van Aken, Jutta Schwarzkopf, and Andreas Klein. “Fermi energy, electrical conductivity, and the energy gap of NaNbO₃”. In: *Physical Review Materials* 6 (2022), DOI: <https://doi.org/10.1103/PhysRevMaterials.6.084404>

Jasnamol P. Palakkal, **Thorsten Schneider** and Lambert Alff. “Oxygen defect engineered magnetism of La₂NiMnO₆ thin films”. In: *AIP Advances* 12 (2022), DOI: <https://doi.org/10.1063/9.0000360>

Jasnamol P. Palakkal, Lukas Zeinar, Márton Major, Philipp Komissinskiy, **Thorsten Schneider**, and Lambert Alff. “Thickness-Dependent Magnetism in Epitaxial SrFeO_{3-x} Thin Films”. In: *IEEE Transactions on Magnetics* 57 (2021), DOI: <https://doi.org/10.1109/TMAG.2020.3023372>

Conference Contributions

ISAF2022 (Tours, France): “Antipolar ground state in NaNbO_3 Thin Films grown by Pulsed Laser Deposition”; **Thorsten Schneider**, Juliette Cardoletti, Hui Ding, Mao-Hua Zhang, Tianshu Jiang, Márton Major, Philipp Komissinskiy, Leopoldo Molina-Luna, and Lambert Alff. Oral Presentation.

MSE2022 (Darmstadt, Germany): “Antipolar ground state in NaNbO_3 Thin Films grown by Pulsed Laser Deposition”; **Thorsten Schneider**, Juliette Cardoletti, Hui Ding, Mao-Hua Zhang, Tianshu Jiang, Márton Major, Philipp Komissinskiy, Leopoldo Molina-Luna, and Lambert Alff. Oral Presentation.

GPMS 2022 (Sendai, Japan): “Strain engineering of Antiferroelectricity”; **Thorsten Schneider**, Juliette Cardoletti, Hui Ding, Philipp Komissinskiy, Leopoldo Molina-Luna, and Lambert Alff. Invited oral Presentation.

ISAF2023 (Cleveland, USA): “Strain Engineering of Antiferroelectricity in NaNbO_3 thin films”; **Thorsten Schneider**, Juliette Cardoletti, Hui Ding, Mao-Hua Zhang, Philipp Komissinskiy, Leopoldo Molina-Luna, and Lambert Alff. Oral Presentation.

Curriculum Vitae

Education

- | | |
|-------------------|--------------------------------------------------------------------------------------------------------------------------------------------------------------------------------------------------------------------------------------------------------------------------------------------------------------------------------------|
| 03/2019 – 03/2023 | Technische Universität Darmstadt, Germany
Research assistant and PhD candidate with the focus on the thin film growth of the antiferroelectric materials NaNbO_3 and AgNbO_3 by pulsed laser deposition; conducted at the advanced thin film division (Dünne Schichten), Department of Materials Science |
| 10/2016 – 03/2019 | Technische Universität Darmstadt, Germany
Master of Science in Materials Science; Titel der Thesis: “ <i>Magnetic properties of double-perovskite Sr_2CrWO_6 thin films produced by pulsed laser deposition</i> ”; Final grade: 1.22 |
| 10/2013 – 09/2016 | Technische Universität Darmstadt, Germany
Bachelor of Science in Materials Science; Bachelor thesis title: “ <i>Der Korngrenzendiffusionsprozess in NdFeB Permanentmagneten unter Verwendung von $\text{NdCu}'6z'$</i> ”; Final grade: 1.41 |

Research Experiences

- | | |
|-------------------|----------------------------------------------------------------------------------------------------------------------------------------------------------------------------------------------------------|
| 09/2017 – 03/2018 | Tohoku Universität, Sendai, Japan
Research project; Title: “ <i>Electrical and magnetic transport properties of $\text{CoFeB}/(\text{Ta},\text{Ru})$ layers</i> ”; Final grade: 1.7 |
| 10/2014 – 05/2017 | Technische Universität Darmstadt, Germany
Scientific assistant in the group “ <i>Functional Materials</i> ” by Professor Oliver Gutfleisch |
| 08/2014 – 09/2014 | Umicore AG, Hanau, Germany
Internship in the research division for solders |